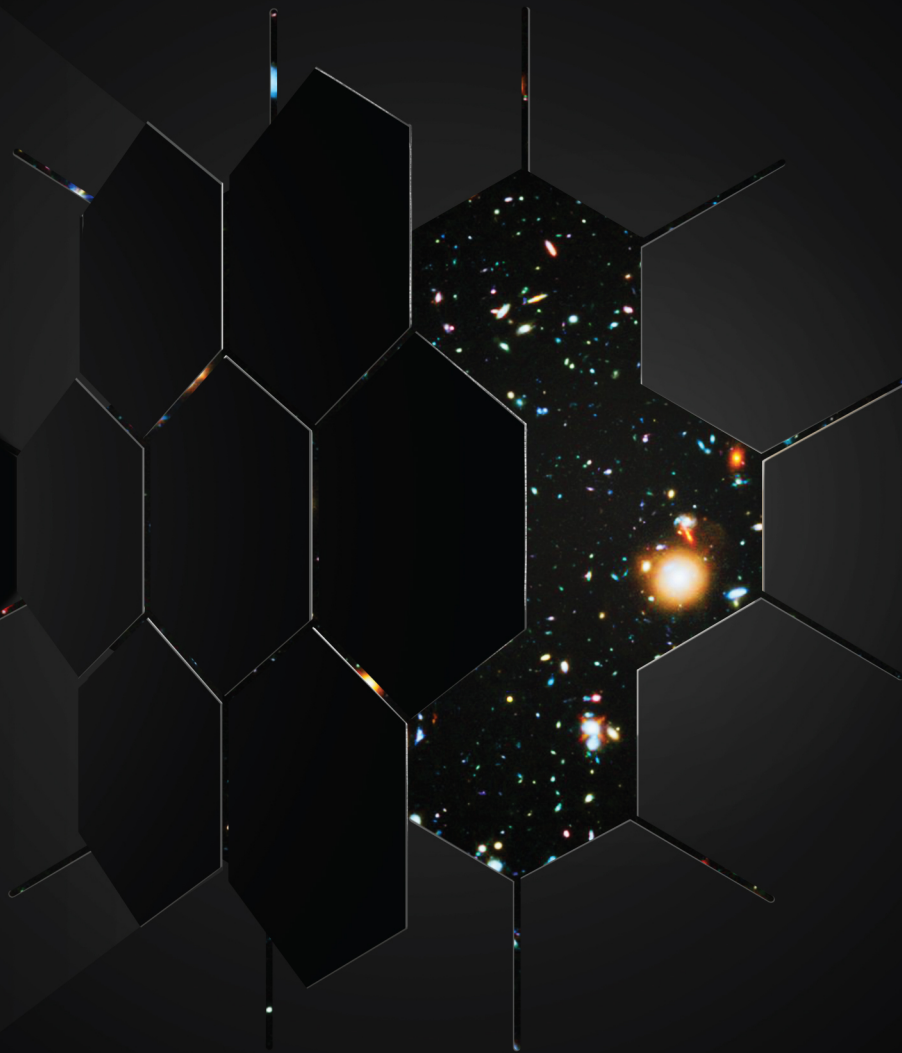


# Galaxy Evolution Probe



*Polycyclic aromatic hydrocarbons (PAH) are key probes for investigating the evolution of galaxies.*



**Principal Investigator:**  
Jason Glenn  
University of Colorado Boulder

**Prepared For:**  
National Aeronautics and Space Administration  
Science Mission Directorate

### List of Participants

Participant	Contribution	Institution
Jason Glenn	Principal Investigator	University of Colorado Boulder
Katherine Alatalo	Lensed high-redshift galaxy science	Space Telescope Science Institute
Rashied Amini	JPL Lead and systems engineering	JPL
Lee Armus	Infrared extragalactic astronomy	Infrared Processing and Analysis Center
Andrew Benson	Galaxy evolution theory	Carnegie Institute
C. Matt Bradford	Mid- and far-infrared spectroscopy of galaxies	JPL
Jeremy Darling	Supermassive black hole accretion and star formation in galaxies	University of Colorado Boulder
Peter Day	Kinetic inductance detectors	JPL
Jeanette Domber	Systems engineering	Ball Aerospace
Duncan Farrah	Star formation in galaxies as a function of environment	University of Hawaii
Adalyn Fyhrie	Mid- and far-infrared background radiation	University of Colorado Boulder
Mark Shannon	Systems engineering	Ball Aerospace
Brandon Hensley	Polycyclic aromatic hydrocarbons	Princeton University
Sarah Lipsy	Systems engineering	Ball Aerospace
Bradley Moore	Cryogenic and thermal design	JPL
Sebastian Oliver	High-redshift galaxies	University of Sussex
Benjamin Oppenheimer	Galaxy formation theory	University of Colorado Boulder
David Redding	Mirror design	JPL
Michael Rodgers	Optical design	JPL
Erik Rosolowsky	Star formation and interstellar medium in nearby galaxies	University of Alberta
Raphael Shirley	Extragalactic source confusion mitigation	University of Sussex
John Steeves	Mirror design	JPL
Alexander Tielens	Polycyclic aromatic hydrocarbons and interstellar medium in galaxies	NASA Ames
Carole Tucker	Optical (infrared) filters	Cardiff University
Gordon Wu	Systems engineering	Ball Aerospace
Jonas Zmuidzinas	Kinetic inductance detectors and readout electronics	Caltech/JPL

### Acknowledgements

This work was supported, in part, by a NASA Astrophysics Probe Concept Study grant. This research was funded in part by the Jet Propulsion Laboratory, California Institute of Technology, under a contract with the National Aeronautics and Space Administration. The PI would like to thank Ball Aerospace for their support of the Study effort. The GEP team would like to thank many contributors whose important work helped lead to the successful completion of this study but whose roles traditionally do not qualify for inclusion in authorship lists of scientific publications: engineering aides, documentarians, administrators, administrative aides, and reviewers.

### Disclaimer

The costs presented in this report are ROM estimates; they are not point estimates or cost commitments. It is possible that each estimate could range from as much as 20% percent higher to 10% lower. The costs presented are based on Pre-Phase A design information, which is subject to change.

The cost information contained in this document is of a budgetary and planning nature and is intended for informational purposes only. It does not constitute a commitment on the part of JPL and/or Caltech.

**Table of Contents**

Factsheet ..... 1

1 Executive Summary ..... 3

2 Galaxy Evolution Probe Science ..... 5

3 Instrument Payload ..... 27

4 Design Reference Mission ..... 32

5 Cost, Risk, And Heritage Assessment ..... 36

6 Technology Maturation Plan ..... 40

7 Management Plan ..... 44

8 Conclusions ..... 44

Appendix A - Acronyms ..... A-1

Appendix B - References ..... B-1

Cost Table ..... 46

# GEP Galaxy Evolution Probe

GEP is an exciting new mid and far-infrared NASA Astrophysics Probe (<\$1B) Concept. GEP will: **(01)** Map the history of galaxy growth by star formation and accretion by super-massive black holes and characterize the relation between those processes.

**(02)** Measure the evolution of the interstellar medium and the buildup of life-enabling heavy elements, such as carbon, nitrogen, and oxygen, in the hearts of galaxies over cosmic time.

## GEP MISSION PARAMETERS

Target Launch Date  
**January 1, 2029**

Orbit  
**Sub-Earth L2**

Observing Mode  
**Dedicated Surveys**

Duration  
**4 Years**

## GEP IMAGER: GEP-I

Wavebands  
**23 Bands covering 10-400  $\mu\text{m}$**

R ( $\lambda/\Delta\lambda$ )  
**8 (10-95  $\mu\text{m}$ ), 3.5 (95-400  $\mu\text{m}$ )**

Surveys and Target Depths  
(towards elliptic poles, except for all-sky survey)  
**All Sky,  $\sim 1$  mJy**  
**300 square degrees,  $\sim 50$   $\mu\text{Jy}$**   
**30 square degrees,  $\sim 20$   $\mu\text{Jy}$**   
**3 square degrees,  $\sim 5$   $\mu\text{Jy}$**

## GEP PAYLOAD

Telescope  
**2.0 m, 4 K, unobscured, SiC**

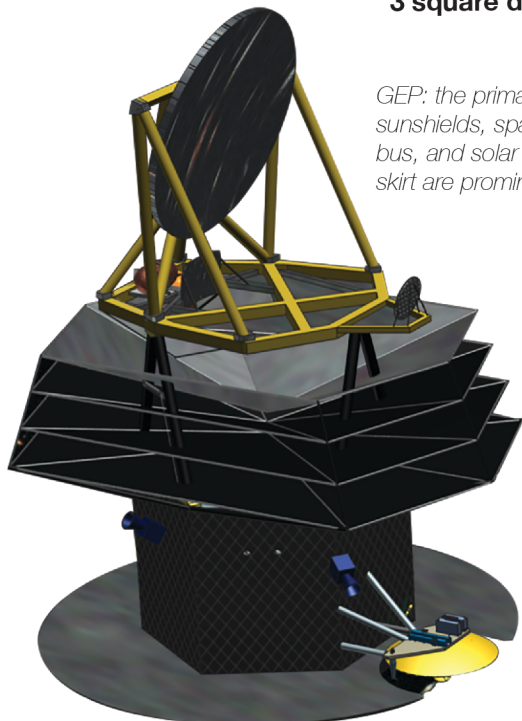
Detectors  
**Kinetic Inductance Detectors**

## GEP SPECTROMETER: GEP-S

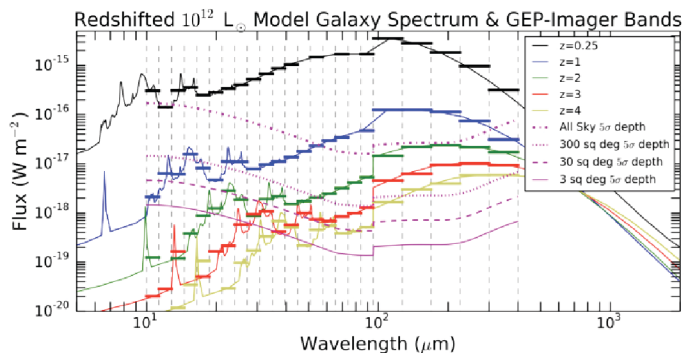
Bands ( $\mu\text{m}$ )  
**24-42, 40-70, 66-116, 110-193**

R ( $\lambda/\Delta\lambda$ )  
**200**

Surveys  
**Selected galaxies, 1.5 and 100 square degrees**



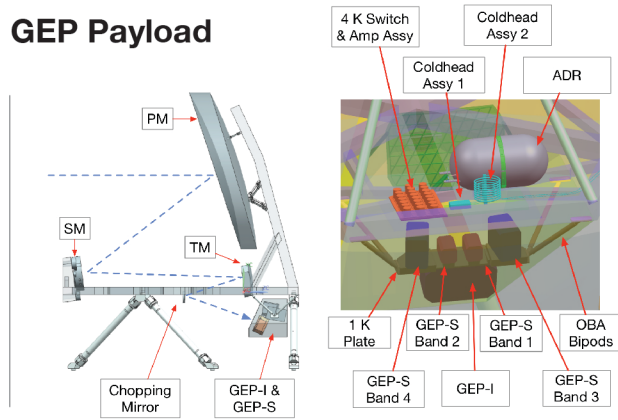
*GEP: the primary mirror, sunshields, spacecraft bus, and solar panel skirt are prominent.*



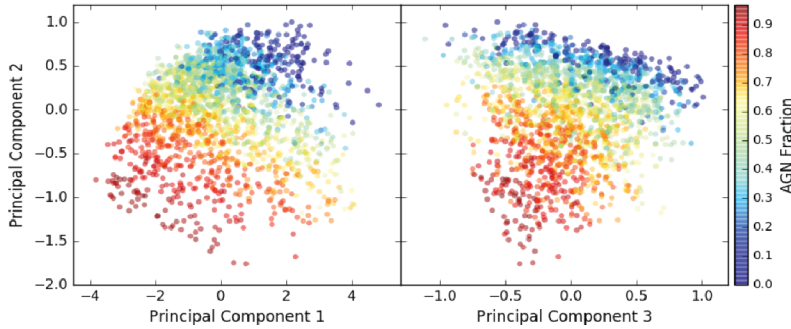
*Redshifted model spectrum of a star-forming galaxy and GEP survey depths. GEP will measure the redshifts of a million galaxies to  $\sigma_z = 0.1$  using the prominent PAH emission lines and distinguish their star-formation rates and black hole accretion luminosities.*

# GEP Technical Data

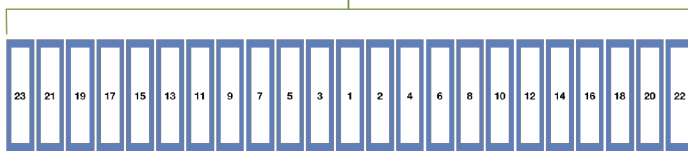
## GEP Payload



Parameter	GEP Design
Mission Class	B, dual string (hot/cold redundancy)
Anticipated Bus Heritage	Ball BCP2000
Dry Mass (CBE+Contingency)	1320 kg
Max Power (CBE+Contingency)	1990 W
Stabilization	Three axis (0.5 as/3 min) non-spinning
Primary Mirror Temperature	4 K design, 6 K allowable
Focal Plane Temperature	100 mK
Field of Regard	$\pm 20.6^\circ$
Total Mission Science Data	> 350 TB

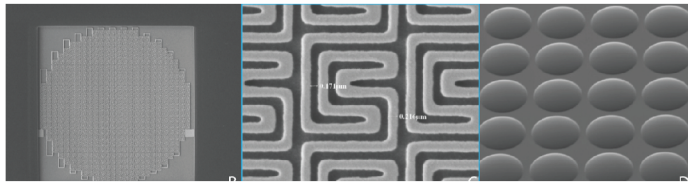


GEP-I KID Array & Bandpass Filters



**Bands 1-18:**  
Band: 10-95  $\mu\text{m}$  (13% Bandwidth)  
KID Arrays: 12 x 120 pixels

**Bands 19-23:**  
Band: 95-400  $\mu\text{m}$  (29% Bandwidth)  
KID Arrays: Varies, less than 12 x 120 pixels

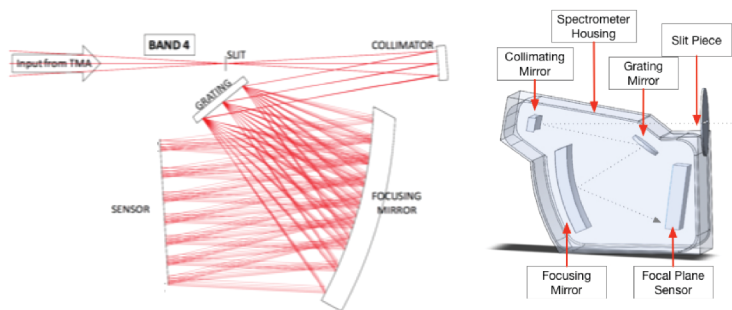


## GEP Imager: GEP-I

GEP will detect millions of star-forming galaxies, measure their redshifts, and separate their star-formation and super-massive black hole accretion (AGN) luminosities. A simulation using principle component analysis using GEP-I's 23 bands is shown here.

GEP-I will be comprised of 23 spectral bands, totaling 25,735 kinetic inductance detectors (KIDs).

Left to Right: 10 $\mu\text{m}$  (Band 1) KID absorber, absorber detail, and micro lens array.



## GEP Spectrometer: GEP-S

GEP-S covers 24 - 193  $\mu\text{m}$  with four modules and 24,640 KIDs.

## 1 EXECUTIVE SUMMARY

Understanding the physical processes that drove the evolution of galaxies is a key topic in modern astrophysics and a principal goal of NASA's space science program. Building upon decades of observational and theoretical work, we are within reach of creating a self-consistent model for galaxy evolution. That model must and will start from cosmology, incorporate stellar dynamics and evolution, and include interstellar processes, star-formation, and supermassive black hole growth. But critical questions remain: What was the role of feedback from black holes and stars themselves in regulating star-formation? How do a galaxy's external environment and internal contents influence its evolutionary trajectory? Where and when were the Universe's heavy elements forged in galaxies? Answering these questions requires measurements in the mid and far infrared because galaxies were permeated with dust through their most active evolutionary stages. The Galaxy Evolution Probe (GEP) is a NASA Astrophysics Probe concept that capitalizes on new detector capability to address these questions with a powerful mid- and far-infrared toolset.

Thanks to ground-breaking prior infrared (IR) observatories such as *IRAS*, *Spitzer*, *ISO*, and *Herschel*, and dedicated ground-based (e.g., SCUBA and SPT) and space-based (e.g., *Hubble*) ultraviolet and optical observing campaigns, astronomers have deduced that the total star-formation rate was more than an order of magnitude higher at the Universe's halfway point ( $z \sim 1$ ) than it is in the present-day. Why has star formation declined so precipitously since that time? Feedback is often invoked, and most galaxy evolution models require feedback from active galactic nuclei (AGN) and stars to explain the local stellar mass functions of galaxies. Observationally we know that supermassive black-hole masses are well correlated with their host galaxy bulges, suggesting a close connection in their respective growth histories. Understanding the interplay between AGN and stellar feedback and the formation of new stars is central to understanding galaxy evolution.

Addressing these questions will require panchromatic studies, and we are approaching a special time in astronomy when this can come to fruition. ALMA and JWST will simultaneously enable high-resolution observations of galaxies, and

large near-IR and optical surveys by, e.g., WFIRST, Euclid, and LSST, will measure the stellar masses of large samples of galaxies, eROSITA will identify AGN and measure X-ray luminosities, and SKA will measure neutral atomic gas masses and probe star-formation and AGN with continuum measurements. An essential outstanding component, however, will be measurements of star-formation rates and black hole growth rates in galaxies unbiased by dust extinction over a broad range of redshifts, luminosities, and (halo) environments.

To make these measurements, large-scale mid- and far-IR surveys that identify star-forming galaxies and correlate their star-formation rates (SFRs) with other physical properties are needed. Sensitivity is required that will be sufficient to detect Milky Way-type galaxies at  $z = 2$  ( $L^*$ ,  $\sim 10^{12} L_{\odot}$ ), at the peak of cosmic star-formation, prior to when most cosmic stellar mass has been assembled. SFRs and supermassive black hole (SMBH) accretion rates must be assessed over a full range of cosmic environments, from isolated field galaxies, to galaxies in groups and in massive clusters, including those that are still forming. Determining the relative importance of star-formation and AGN in powering the dust emission and heating the gas in large samples of galaxies will be required to understand how stellar and SMBH growth are linked over cosmic time. Spectral mapping capability is required for unbiased 'blind' spatial-spectral surveys and line mapping of nearby galaxies to measure gas column densities, ionization parameters, and metallicities with tracers unaffected by dust obscuration. Crucially, the galaxies must have measured redshifts so that their epochs and distances are known and so that their X-ray, optical, near-IR, and radio counterparts can be identified in large numbers for panchromatic studies. These IR observations must be made from space because the Earth's atmosphere is opaque to mid- and far-IR radiation.

GEP is a concept for a mid-IR/far-IR space observatory purpose-designed to answer important questions about the evolution of star-formation and massive black holes in galaxies (Table 1). GEP will measure star-formation rates and detect AGN even under conditions of heavy extinction. It will measure SMBH accretion rates to address the connection between the masses of stellar populations and supermassive black holes. The same observations enable GEP to measure metallicities with extinction-

**Table 1.** GEP payload parameters.

GEP Mission Parameters	
Target Launch Date	January 2029
Orbit	Sun-Earth L2
Observing Mode	Dedicated Surveys
Duration	4 Years
GEP Payload	
Telescope	2.0 m, 4 K, unobscured, SiC
Detectors	Kinetic Inductance Detectors
GEP Imager (GEP-I)	
Wavebands	23 bands covering 10-400 $\mu\text{m}$
R ( $N/\Delta\lambda$ )	8 (10-95 $\mu\text{m}$ ), 3.5 (95-400 $\mu\text{m}$ )
Surveys and Target Depths	All sky, $\sim 1$ mJy
	300 square degrees, $\sim 50$ $\mu\text{Jy}$
	30 square degrees, $\sim 20$ $\mu\text{Jy}$
	3 square degrees, $\sim 5$ $\mu\text{Jy}$
GEP Spectrometer (GEP-S)	
Bands	24-42, 40-70, 66-116, 110-193 $\mu\text{m}$
R ( $N/\Delta\lambda$ )	200
Surveys	Selected galaxies, 1.5 and 100 square degrees

free tracers to observe growth of metals over the last 2/3 of the Universe’s age. In nearby galaxies, GEP will observe feedback between star-formation, AGN, and the interstellar medium (ISM) to understand the processes that regulate star-formation. By mapping nearby galaxies and the Galactic ISM, GEP will reveal the energy balance of the ISM by measuring the total interstellar material mass, ionization state, and the local radiation field using fine-structure transitions of ions and polycyclic aromatic hydrocarbon (PAH) molecules.

GEP will have a 2.0 m, 4 K telescope that will enable sensitivity limited by astrophysical sources: zodiacal dust emission and Galactic dust emission. GEP will have one scientific instrument with two modules: an imager, GEP-I, and a dispersive spectrometer, GEP-S. GEP-I will have 23 photometric bands distributed on the focal plane: 18 resolution  $R = 8$  bands from 10–95  $\mu\text{m}$  designed to measure photometric redshifts with PAHs and five resolution  $R = 3.5$  bands from 95 to 400  $\mu\text{m}$  to measure dust spectral energy distributions (SEDs) encompassing the SED peak to beyond  $z = 2$ . GEP-S will be comprised of four long-slit grating spectrometers with spectral resolution  $R = 200$  from 24 to 193  $\mu\text{m}$ . Both modules will utilize arrays of kinetic inductance detectors (KIDs) cooled to 100 mK by a multistage adiabatic demagnetization refrigerator (ADR) backed by a hybrid Joule-Thomson and Stirling cryocooler, which will also cool the telescope and coupling optics.

GEP will achieve its goals with large, multi-tiered surveys for galaxies detected by their mid/far-IR emission from dust, PAHs, and atomic fine-structure lines. GEP will conduct two types of surveys: photometric with GEP-I and spectroscopic with GEP-S. The photometric survey areas will be 3, 30, and 300 sq deg, and an all-sky survey. The photometric redshift precision of galaxies will typically be  $\sigma_z \leq 0.1$ . The spectral surveys will cover a range of low- and high-ionization atomic fine-structure lines. Spectral surveys will consist of ‘blind’ surveys utilizing a long-slit configuration and follow-up, deep pointed observations of galaxies identified in the photometric surveys, and the regions of the Milky Way and nearby galaxies.

From mid/far-IR dust emission, PAHs, and atomic fine-structure lines, SFRs and SMBH accretion rates will be calculated, and the abundances of metals in the atomic, molecular, and solid (dust) phases of the interstellar medium will be measured. Infrared luminosity functions of galaxies will be assembled as a function of redshift probing well below  $L^*$  over large enough volumes to be immune to the effects of cosmic sample variance (hereafter *sample variance*) that often plague small-area cosmological surveys. By correlating physical properties as a function of redshift and environment, *GEP will address the compelling science questions with unique data that cannot be obtained by any other means.* GEPs observations will be highly complementary to current and future observatories that target UV and optical emission from stars and gas: it will probe properties of star-formation and the star-forming ISM rather than stellar masses and warm or hot ISM. More than 100 million galaxies will be detected, with mid-IR/far-IR SEDs measured, and redshifts obtained for more than 1 million galaxies. *GEPs capability will be a major step forward in studies of star-forming galaxies over a significant fraction of cosmic time through a unique combination of medium-band photometry and spectroscopy that has never been used before in an IR space observatory.*

GEP shares common elements with two other cryogenic far-IR space missions under study: SPICA, an ESA-JAXA collaboration recently selected as a candidate for the M5 mission in Europe, and Origins Space Telescope, a NASA-led Flagship-class study being prepared for the Astro2020 Decadal Survey. SPICA features a 2.5 m,

6–8 K telescope and a spectrometer using sensitive bolometer arrays. It will be powerful for one-by-one galaxy follow-up, but with its smaller array sizes (e.g., 3600 pixels total for the far-IR spectrometer), it cannot match the mapping speed of GEP in either imaging or spectroscopy. *Furthermore, it does not have the 23-band, moderate spectral resolution imaging that is central to GEP’s architecture, so it cannot measure redshifts photometrically as GEP will.* Origins Space Telescope, with its 5.6 meter, 4.5 K telescope, will be very powerful. Its multi-billion-dollar scope, however, puts its earliest possible realization well into the 2030 decade. With its simple, optimized implementation, GEP provides excellent science value in this still relatively unexplored spectral regime.

GEP launch is planned for January 1, 2029, using a Falcon 9 rocket. It will have a mission duration of four years. GEP will perform its observations from the dark, quiet environment of Earth-Sun L2. An available field of regard of  $\pm 21$  degrees will provide constant access to the north and south ecliptic poles, which have the minimum average zodiacal emission in the sky. GEP has total dry mass of 1,320 kg (CBE with contingency) with a maximum power requirement of 1,990 W (CBE with contingency).

The GEP mission utilizes a low-risk approach to achieving large multi-tiered galaxy surveys within the Probe-class cost cap through use of a single instrument, a simple survey-based operations plan, and high-heritage flight hardware. The GEP study evaluated the cost of the mission to be \$910–951M FY18, including 30% Phase A–D reserves, based on NASA JPL Team X and GEP team assessments.

Like *Kepler* and several other NASA missions, GEP uses the Ball BCP2000 bus, capable of meeting GEPs pointing, propulsion, and data requirements. The GEP mission was designed to include substantial pointing, thermal, and data margin with redundancy of critical components, assuring a low-risk mission by design.

No new technologies are required to fabricate GEPs cryocoolers and optical assembly. GEPs technology development plan provides a clear pathway to KID detector and readout electronics readiness, taking advantage of ongoing developments funded by NASA and rapid progress in industry, respectively. The detector TRL will be raised by both laboratory demonstrations and a

pathfinder long-duration balloon (GEP-B), which will perform precursor GEP science while also demonstrating optics technology.

Buoyed by major discoveries about star-formation and massive black holes in galaxies in the previous decades, astronomers are ready to take the next step in galaxy evolution by characterizing the processes that drove star-formation and supermassive black hole growth. The GEP is a NASA Astrophysics Probe concept study designed to provide key data on these astrophysical processes with large surveys orthogonal and complementary to observational data expected over the next two decades. GEP will have a major impact on astronomers’ understanding of the star-formation in galaxies within the \$1B Probe cost cap, providing NASA an opportunity for an affordable mission with a lasting legacy.

## 2 GALAXY EVOLUTION PROBE SCIENCE

### 2.1 Science Goals and Objectives

GEP addresses questions on the key physical processes, which control the formation and assembly of galaxies and their components across cosmic history, identified in the *NASA Astrophysics Roadmap 2013: Enduring Quests, Daring Visions*.

Goal #1: Map the history of galaxy growth by star formation and accretion by supermassive black holes and characterize the relation between those processes.

Star formation began sometime in the first billion years of the Universe, then rose to a peak or broad plateau in the range  $1 < z < 3$ , and declined sharply in the last half of the Universe’s history (Figure 1, *top*). Substantial uncertainties in the cosmic star-formation history persist, including: SFRs derived from IR galaxy surveys of limited size that do not probe low luminosities and are limited by sample variance, uncertain redshifts of large samples of far-IR continuum-detected galaxies, and uncertain extinction in rest-frame UV observations. Thus, GEP will address these concerns with large, deep IR surveys for star-forming galaxies, with redshifts, and meet its first objective: to **measure the coevolution of and discriminate between star formation and SMBH growth in galaxies (Objective 1a)**. GEP-I dust continuum, spectral slope, and PAH/continuum measurements will yield star-formation and SMBH accretion rates and infrared luminosity functions for millions of galaxies from  $0 < z < 3$ , attaining a depth of  $L_* = 10^{12}$

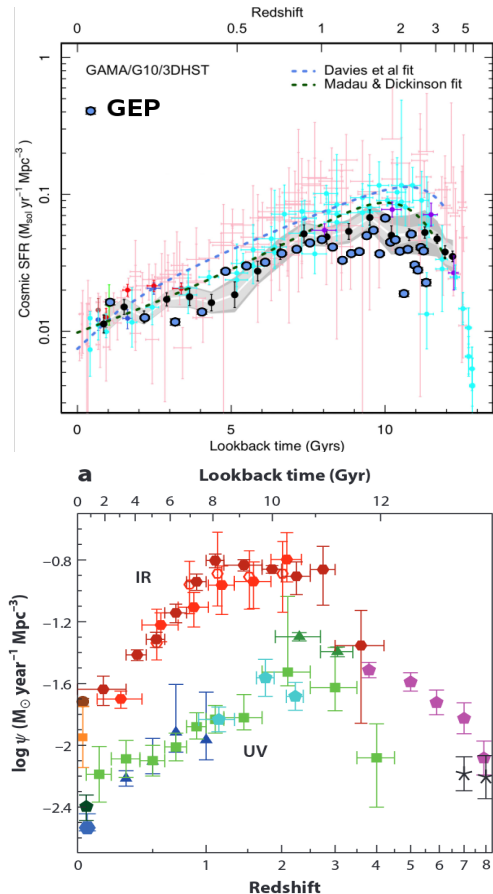


**Figure 1.** GEP provides a significant leap in our understanding of the evolution of the cosmic history of star-formation by measuring the star formation rate density accurately across a wide range of redshifts. *Top:* A recent study by [Driver et al. 2017] compiling multiband deep data shows the substantial uncertainties that persist with the existing datasets. The principal source of uncertainty is the limitation of the far-IR data, a limitation that GEP will remove. Blue circles from simulation (for  $0 < z < 3$  only) show expectations from a combination of GEP full sky, 300, 30, and 3 square degree surveys, showing that GEP will measure the star formation history with unprecedented precision (in most cases error bars are smaller than the symbols). *Bottom:* IR observations are an essential probe of star formation in galaxies. The compilation from [Madau and Dickinson 2014], highlights the predominance of the thermal IR in the history of star-formation (extinction corrections have not been applied to UV observations).

$L_{\odot}$  at  $z = 2$ , in a comprehensive range of environments. Concurrently, the 23-band GEP-I photometry of the mid-IR PAH features will yield redshifts for the galaxies. PAHs have been detected spectroscopically with *Spitzer* at high redshifts,  $z = 1.09$  and  $2.96$  [Teplitz et al. 2007] and  $z = 4.055$  [Riechers et al. 2014] in galaxies with and without prominent AGN. GEP-S spectroscopy of high-ionization atomic fine-structure lines, such as [Ne V], will yield SMBH accretion rates.

GEP will access the earliest epochs of galaxy growth ( $z > 3$ ) by utilizing the brightening from gravitational lensing. In their recent star-formation history review [Madau and Dickinson 2014], conclude that our knowledge of dust-obscured star-formation from  $z \approx 2$  to 8 leaves considerable uncertainty about how much SFR density may be missed in the UV census of that early phase of galaxy evolution (Figure 1, *bottom*). Wide-area GEP-I surveys taking advantage of the brightening provided by gravitational lensing will address this problem head-on with  $10^4$  lensed high- $z$  galaxies. These galaxies can then be followed-up with GEP-S.

Understanding the role of accreting SMBHs in galaxy formation and evolution requires IR observations since dusty disks or tori obscure black hole growth. A principal objective of GEP is therefore to identify obscured AGN in galaxies and relate their accretion luminosities to their star-formation rates. GEP will identify and quantify luminosities of dust-obscured AGN via mid-IR spectral signatures, including the continuum shape with GEP-I and high-ionization fine-structure atomic transitions with GEP-S. GEP complements X-ray detection of AGN because X-ray observations can miss Compton thick AGN or underestimate accretion rates.

GEP will test a key hypothesis of some evolutionary models using a census of obscured AGN activity. Specifically, by identifying galactic outflows from high-velocity spectral line wings such as [Peeters et al.] to assess energy injection into the ISM, **GEP will determine whether feedback from buried accreting black holes could have caused the decline of luminosity density from star-formation in the last half of the Universe's history (Objective 1b)**. The masses of supermassive black holes in the centers of modern-day galaxies are well correlated with galaxies' bulge masses [Magorrian et al. 1998; Marconi and Hunt 2003]. This has led to

the hypothesis that some feedback loop exists in which AGN activity governs the rate of star-formation in galaxies, or at least in galactic bulges [Silk and Rees 1998]. Theoretical models—for example, [Bower et al. 2006; Croton et al. 2006; Sijacki et al. 2007; Di Matteo et al. 2008]—invoke AGN feedback as a primary mechanism to explain the observed distribution of galaxy masses today. Without AGN and feedback, models are unable to explain the low ratio of galactic stellar mass to halo mass at both high and low masses [Benson et al. 2003] (see Figure 2). Yet the efficiency of AGN feedback for regulating star formation remains controversial [Wagner et al. 2016; Silk 2013].

GEP will assess the role of feedback in distant galaxies both via correlation analyses of the AGN/star-formation partitioned samples and by measuring aggregate line wings in high-ionization gas via stacked spectra. In nearby galaxies, **GEP will obtain a spatially resolved view of feedback and its effects with a detailed spectroscopic study of galactic outflows and fountains in local**

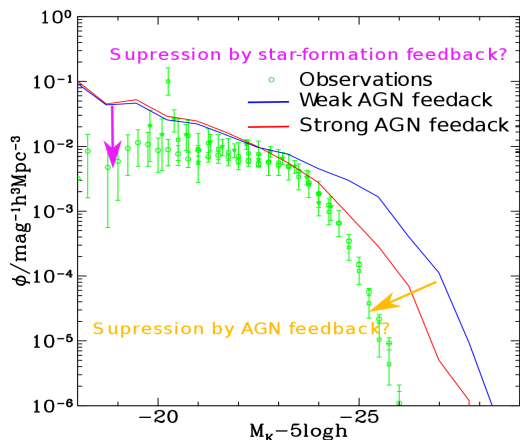


**Figure 2.** GEP offers multiple paths to understanding the degree to which strong feedback suppresses star-formation in massive galaxies. Galaxy evolution models require strong AGN feedback to explain galaxy masses. The K-band luminosity function of galaxies from [Benson et al. 2003] is shown. Green points show observations. The models shown by the blue and red lines illustrate the effects of increasingly strong feedback from AGN in a model of galaxy formation, described by the fraction of the supermassive black hole’s Eddington luminosity that is coupled into an outflowing wind. At faint magnitudes feedback from star formation is expected to suppress galaxy formation.

**galaxies** in various atomic fine-structure emission lines (**Objective 1c**). Species with bright lines include [C II], [N II], and [O III].

With the star-formation history cataloged, **GEP will determine whether interstellar gas conditions at star-formation sites in galaxies changed as star formation declined (Objective 1d)**. Measurement of fine-structure lines including [C II], [N II], and [O III] will be used to infer the masses of interstellar gas components (neutral/ionized), the hardness of the UV radiation fields and its implications for the stellar initial mass function, and the density of HII regions from which the pressure in the ISM can be inferred. These measurements will address physical properties of the star-forming regions in galaxies and thus inform theories and models of star-formation. Aggregate spectra created by stacking on near-IR priors insure high signal-to-noise ratio (SNR) studies of hundreds of thousands of galaxies. Furthermore, GEP will measure emission from PAHs in galaxies out to at least  $z = 4$ . By modeling PAH properties, these combined observations constrain the physical conditions of the ISM and the consequences for star-formation and dust grain physics. The resulting relations between metallicity, star-formation rate, and other galaxy properties will inform models of galactic winds by placing constraints on the presence of gas-phase metals at their source.

**Goal #2:** Measure the growth of metals and changing of star-formation environments over cosmic time.

Metallicity represents the effects of star-formation, inflow, and outflow of matter from galaxies and can be used as a probe of how galaxies are assembled. Measurements of metallicity as a function of galaxy luminosity will constrain these physical processes. Metallicities of galaxies have not been measured beyond the local universe with unbiased, extinction-free probes using far-IR atomic fine-structure lines. GEP will **measure metal (heavy element) content and observe the buildup of metals in galaxies over the peak epoch of star-formation** with spectroscopic surveys of metals in atomic gas, PAHs, and dust (**Objective 2**). GEP will measure the absolute metallicity in galaxies in the last  $\frac{2}{3}$  of Universe’s history, reaching down to typical ( $L^* = 10^{12} L_{\odot}$ ) galaxies at  $z = 2$ , using the nitrogen to oxygen ratio. Relative metallicities will be measured using the neon to sulfur ratio.

## 2.2 Science Traceability Matrix

GEP's contribution to the science goals outlined above will have a lasting impact on the science community by addressing key aspects of the evolution of our cosmos. These goals are listed in the leftmost column of the science traceability matrix (Science Traceability Matrix (STM), Figure 3). Read from left to right, the flow from column to column of the STM details how these goals will be achieved via measurements of physical parameters, survey requirements and observables, and ultimately payload requirements, mission functional requirements, and mission design. The payload projected performance and mission projected performance columns demonstrate that the observatory requirements are met.

Science Goals	Science Objectives	Scientific Measurement Requirements: Physical Parameters	Survey Requirements	Scientific Measurement Requirements: Observables	Payload Functional Requirements	Payload Projected Performance	Mission Functional Requirements	Mission Specifications & Projected Performance		
<p><b>Goal #1:</b> Map the history of galaxy growth by star formation and accretion by supermassive black holes and characterize the relation between those processes. "Use telescopes as time machines to map the full history of galaxy formation and assembly," and "characterize... the relation between [this history and that of] black holes." (Enduring Quests and Daring Visions, pp. 8 and 54.)</p>	<p><b>Objective #1a:</b> Measure the coevolution of and discriminate between star formation and supermassive black hole growth in galaxies.</p>	<p><b>Measure:</b> a) redshifts, b) luminosity from star formation, and c) luminosity from AGN accretion for representative galaxy populations using coarse mid-IR spectrophotometric surveys.</p> <p><b>Epochs under study:</b> <math>0 &lt; z &lt; 2</math> for <math>L \leq L^*</math> galaxies, higher <math>z</math> for <math>L &gt; L^*</math> and lensed galaxies.</p> <p><b>Reach to <math>L^*</math>:</b> <math>10^{10} L_{\odot}</math> at <math>z = 0.1</math> and <math>10^{12} L_{\odot}</math> at <math>z = 2</math>.</p> <p><b>Photometric redshift precision:</b> <math>\sigma_z = 0.1</math>, validated spectroscopically in sub-samples.</p> <p><b>Spectroscopic redshifts:</b> precision <math>\sigma_z = 1\%</math> for <math>&gt;1000</math> galaxies to verify photometric redshifts.</p> <p><b>AGN power confirmed</b> with spectroscopic measurement of [OIV] (26 <math>\mu\text{m}</math>) transition in sub-sample.</p>	<p><b>Areas:</b> Wide and deep surveys should each comprise <math>\sim 10^5</math> galaxies for sufficient luminosity function resolution and not be limited by cosmic variance: <math>&gt;100</math> and <math>&gt;10</math> sq deg.</p> <p><b>Approach: Broadband spectra</b> for SFRs &amp; LFs: 10 <math>\mu\text{m}</math> (12 and 13.5 <math>\mu\text{m}</math> PAH + continuum baseline at <math>z=0</math>) to 400 <math>\mu\text{m}</math> (dust SED peak <math>0 &lt; z &lt; 2</math> for <math>T_{\text{dust}} &lt; 30</math> K galaxies). <math>R = 8</math> for <math>\sigma_z = 0.1</math>.</p> <p><b>Spectroscopic redshifts:</b> sample from surveys below.</p>	<p><b>PAH emission lines for photometric redshifts:</b> 3.3, 6.2, 7.7, 8.6, 12, 13.5, 17 <math>\mu\text{m}</math> rest frame.</p> <p><b>Depths: <math>1\sigma</math> depths of 10 <math>\mu\text{Jy}</math> in 3 sq deg survey, 30 <math>\mu\text{Jy}</math> in 30 sq deg survey, 100 <math>\mu\text{Jy}</math> in 300 sq deg survey, and 1 mJy in all-sky survey.</b></p> <p><b>Spectra of atomic fine-structure lines for photometric redshifts:</b> [Ne II] 12.8, [Ne III] 15.6, [Si II] 34.8, [O I] 63.2, [O III] 88.4, [N II] 122, and [C II] 158 <math>\mu\text{m}</math>.</p>	<p><b>GEP-I (narrow-band imager)</b></p> <p><b>Spectral coverage:</b> 10 - 400 <math>\mu\text{m}</math></p> <p><b>Spectral resolution:</b> <math>R=8</math> for 10-95 <math>\mu\text{m}</math> and <math>R=3</math> for 95-400 <math>\mu\text{m}</math></p> <p><b>FWHM beam size:</b> 2.6" for <math>\leq 24</math> <math>\mu\text{m}</math>, 7.6" at 70 <math>\mu\text{m}</math>, and 30" at 263 <math>\mu\text{m}</math></p> <p><b>Mapping speed:</b> 10 sq deg/mJy<sup>2</sup>/hr</p>	<p><b>GEP-I</b></p> <p><b>Spectral coverage:</b> 10 - 400 <math>\mu\text{m}</math></p> <p><b>Spectral resolution:</b> <math>R=8</math></p> <p><b>FWHM beam size:</b> 2.6" for <math>\leq 24</math> <math>\mu\text{m}</math>, 7.6" at 70 <math>\mu\text{m}</math>, and 30" at 263 <math>\mu\text{m}</math></p> <p><b>Mapping speed:</b> 10 sq deg/mJy<sup>2</sup>/hr</p>	<p><b>Attitude Control:</b> Pointing Knowledge: 0.5 arcsec <math>1\sigma</math> Pointing Control: 1 arcmin/s <b>Survey Duration:</b> 12,000 hrs <b>Data Volume:</b> 126 TB (0.6 TB/week) <b>Field of Regard:</b> Constant availability of ecliptic poles Constant access <math>\pm 15^\circ</math> about boresight normal to the Sun-Probe line.</p> <p><b>Mapping modes using steering mirror and telescope slew to raster.</b></p>	<p><b>Optics:</b> Type: SiC, unactuated Aperture: 2.0 m Thermal: <math>T_{\text{optics}} &lt; 4-5</math> K <math>T_{\text{FPA}}: 100</math> mK <b>ACS:</b> Type: 3x Star Tracker (+1 spare) and IMU, telemetry fed directly to payload electronics Pointing Knowledge: 0.5 arcsec <math>1\sigma</math> Pointing Control: <math>&gt;&gt;1</math> arcmin/s <b>Survey Duration:</b> 4 year science mission Continuous observation (35,000 hrs) <b>Data Volume:</b> 354 TB Downlink Performance: 1.8 TB/week (2.9X margin over requirement) Downlink Capability: 2.0 TB/week (3.4X margin over requirement) <b>Field of Regard:</b> Constant availability of ecliptic poles Constant access <math>\pm 21^\circ</math> about boresight normal to the Sun-Probe line. (12° margin over requirement)</p>		
	<p><b>Objective #1b:</b> Determine whether feedback from buried accreting black holes could have caused the decline of luminosity density from star formation in the last half of the Universe's history.</p>	<p><b>1. Measure outflowing gas from AGN.</b> Measure aggregate fluxes in line wings (<math>\pm 500</math> km/s, after deconvolution).</p> <p><b>2. Measure average fluxes of H<sub>2</sub> lines</b> indicating shocked gas associated with feedback processes.</p>	<p><b>Stacked spectra from GEP-DSS. Shift by redshift and stack spectrally in bins to reveal</b> average fluxes in H<sub>2</sub> and in high-velocity wings of key lines such as [Ne V]. Require 5 redshift bins below <math>z=1.5</math>.</p>	<p><b>Spectral Resolving Power:</b> 200. <b>Sensitivity:</b> stacked spectrum should reach <math>1\sigma</math> flux uncertainty of <math>5 \times 10^{-22}</math> W/m<sup>2</sup>.</p>	<p><b>Spectral-line mapping speed:</b> same as above. <b>Spectral resolving power:</b> at least 200.</p>				<p><b>GEP-S (spectrometer)</b></p> <p><b>Spectral coverage:</b> 25 - 78 <math>\mu\text{m}</math></p> <p><b>Spectral resolution:</b> <math>R = 150</math></p> <p><b>Spectral-line mapping speed at 78 <math>\mu\text{m}</math>:</b> <math>1.5 \times 10^{-7}</math> sq degrees / hour / (<math>10^{-19}</math> W/m<sup>2</sup>)<sup>2</sup> (<math>5\sigma</math>)</p>	<p><b>GEP-S</b></p> <p><b>Spectral coverage:</b> 25-193 <math>\mu\text{m}</math></p> <p><b>Spectral resolution:</b> <math>R = 200</math></p> <p><b>Spectral-line mapping speed: At 78 <math>\mu\text{m}</math></b> <math>3.2 \times 10^{-7}</math> sq deg / hour / (<math>10^{-19}</math> W/m<sup>2</sup>)<sup>2</sup> (<math>5\sigma</math>)</p>
	<p><b>Objective #1c:</b> Obtain a spatially resolved view of feedback and its effects in local galaxies with spectroscopic study of galactic outflows and fountains.</p>	<p><b>Outflows and fountains in local galaxies:</b> Maps of [C II], [O I], [O III], [N II], other lines reaching below star-formation threshold.</p>	<p><b>Map 400 nearby resolved galaxies</b> in key far-IR fine-structure transitions. Map areas of 8' by 8' to include outskirts with outflowing gas.</p>	<p><b>Line maps with surface brightness sensitivity reaching</b> below the star-formation column density threshold (see text). 1.5 hours per galaxy.</p>	<p><b>Beam:</b> 20" FWHM at [C II] 158 <math>\mu\text{m}</math></p> <p><b>Sensitivity:</b> Surface brightness sensitivity, per channel, per pix: <math>1 \times 10^{-10}</math> W/m<sup>2</sup>/sr (<math>1\sigma</math>, 15 sec) at [N II] 122 <math>\mu\text{m}</math>.</p> <p><b>Slit length:</b> <math>\geq 24</math> beams</p>				<p><b>GEP-S Beam:</b> 20" at [C II]</p> <p><b>Sensitivity:</b> <math>5 \times 10^{-11}</math> W/m<sup>2</sup>/sr per pixel at 66 <math>\mu\text{m}</math> and longer. <b>Slit:</b> 40 - 70 beams</p>	<p><b>Spectral Resolving Power:</b> 200.</p>
	<p><b>Objective #1d:</b> Determine whether the interstellar gas conditions at star-formation sites in galaxies changed as star formation declined.</p>	<p><b>Evolving ISM conditions in star forming galaxies in the last 1/2 of the Universe's history.</b> Three basic characteristics: mass of star-forming gas, density of gas around young stars, stellar effective temperature.</p>	<p><b>GEP wide spectral survey (GEP-WSS). Overlapping with deep Euclid and/or WFIRST near-IR spectroscopic datasets.</b> Form 100 high-SNR stacks for <math>0 &lt; z &lt; 1</math> with <math>\geq 50</math> galaxies in each stack.</p>	<p><b>Map area:</b> <math>\geq 100</math> sq deg to overcome cosmic variance and Poisson errors. Stack on 1/100 of the 400k available galaxies should have <math>1\sigma = 6 \times 10^{-21}</math> W/m<sup>2</sup> at 78 <math>\mu\text{m}</math> fiducial.</p>	<p><b>100 sq deg survey w/ <math>1\sigma</math> depth of 1.8 x <math>10^{-19}</math> W/m<sup>2</sup> in Band 2.</b> Requires mapping speed of <math>1.6 \times 10^{-7}</math> deg<sup>2</sup>/s / (<math>10^{-19}</math> W/m<sup>2</sup>)<sup>2</sup>. <b>Coverage to 189 <math>\mu\text{m}</math> for [O I] 63 <math>\mu\text{m}</math> at <math>z=2</math>.</b></p>				<p><b>GEP-S mapping speed in Band 2 = <math>3.2 \times 10^{-7}</math> deg<sup>2</sup>/s / (<math>10^{-19}</math> W/m<sup>2</sup>)<sup>2</sup>.</b> <b>Coverage to 193 <math>\mu\text{m}</math>.</b></p>	
<p><b>Goal #2:</b> Measure the growth of metals and changing star-formation environments over cosmic time, addressing NASA Astrophysics questions: "How does our universe work?" and "How did we get here?" (Enduring Quests Daring Visions, p. 33).</p>	<p><b>Objective #2:</b> Measure the metal (heavy element) content and observe the buildup of metals in galaxies over the peak epoch of star formation.</p>	<p><b>Metallicity:</b> Relative metallicity evolution in galaxies from <math>z = 3</math> to <math>z = 1.5</math> using neon to sulfur ratio indicator.</p> <p><b>Metallicity:</b> Metallicities in galaxies in last 8 billion years, using oxygen to nitrogen ratio diagnostic. Reach to 1/2 dex below <math>L^*</math> (<math>L^* = 10^{12} L_{\odot}</math> at <math>z=1.2</math>).</p>	<p><b>Pointed spectra:</b> 300 galaxies (20 each in 15 redshift bins), <math>z = 1.2 - 3</math>. <b>Depth:</b> <math>2 \times 10^{12} L_{\odot}</math> galaxy at <math>z=3</math></p> <p><b>Blindly detect &gt; 500 galaxies in each of 5 redshift x 2 luminosity bins for <math>0 &lt; z \leq 1.2</math> in [N III] 57, [O III] 52 and 88 <math>\mu\text{m}</math>.</b> Most challenging requirement is [N III] detection in faintest bin (<math>3 \times 10^{11} L_{\odot}</math>) at highest <math>z: 1.2</math>.</p>	<p><b>Line Flux:</b> <math>2.8 \times 10^{-4} \times L_{\text{galaxy}}</math>. <math>2 \times 10^{12} L_{\odot}</math> galaxy at <math>z=3</math> produces flux of <math>2.7 \times 10^{-20}</math> W/m<sup>2</sup> in the sulfur lines. <b>Coverage:</b> 25-75 <math>\mu\text{m}</math>.</p> <p><b>Depth:</b> [N III] 57 <math>\mu\text{m}</math> flux from <math>3 \times 10^{11} L_{\odot}</math> galaxy at <math>z=1.2</math> is <math>5.5 \times 10^{-20}</math> W/m<sup>2</sup>. Require <math>5\sigma</math> map depth of this in GEP-S deep survey. <b>Spectral Resolution:</b> <math>R=150</math></p>	<p><b>GEP-S Spectral resolution:</b> <math>R = 150</math></p> <p><b>Sensitivity:</b> <math>5\sigma</math>, 4 hour line flux of <math>2.7 \times 10^{-20}</math> W/m<sup>2</sup>.</p> <p><b>Use 1.5 sq deg GEP-DSS above.</b> <b>Mapping speed <math>\geq 8.6 \times 10^{-7}</math> sq deg / sec / (<math>10^{-19}</math> W/m<sup>2</sup>)<sup>2</sup> in band 4.</b> <b>Spectra Coverage:</b> 50 to 193 <math>\mu\text{m}</math> <b>Spectral Resolving Power:</b> <math>R=100</math></p>	<p><b>GEP-S Spectral resolution:</b> <math>R = 200</math></p> <p><b>Sensitivity:</b> <math>5\sigma</math>, 4 hours line flux of <math>2.1 \times 10^{-20}</math> W/m<sup>2</sup>.</p> <p><b>GEP-S Band 4 mapping speed:</b> <math>1.45 \times 10^{-6}</math> sq deg / sec / (<math>10^{-19}</math> W/m<sup>2</sup>)<sup>2</sup> <b>Spectral Coverage:</b> 24 to 193 <math>\mu\text{m}</math> <b>Spectral Resolving Power:</b> 200</p>	<p>Same as top row, <b>plus Pointed mode with chopping on the spectrometer slit.</b></p> <p>Same as top row</p>			

Figure 3. STM. Light green cells are crosscutting across the Science Objectives.

## 2.3 Perceived Scientific Impact of the GEP

### 2.3.1 Measuring Redshifts and Star-Formation Rates of Millions of Galaxies

GEP Science Objective 1a requires rest-frame mid-IR and far-IR continuum observations and redshifts of galaxies with GEP-I to measure luminosities and star formation rates. The far-IR is the dominant repository of star-formation energy, and uncertainties in the star-formation history are dominated by uncertainties in galaxies’ far-IR properties. Recent star-formation history compilations (Figure 1) show that factors of  $\sim 3$  discrepancy still exist among the various measures of star-formation history at its peak (‘cosmic noon’). As [Driver et al. 2017] conclude, ‘‘Obvious improvements ... include improved measurements of far-IR fluxes.’’ A closely related problem is that far-IR datasets are not always well linked to redshift information; in particular, the vast majority of galaxies discovered with *Herschel* do not have redshift counterparts. GEP will overcome both of these limitations with a novel and powerful technique well suited to the 2 m aperture permitted by the Probe budget.

Using coarse spectroscopy (23-band photometry) targeting the powerful and ubiquitous mid-IR dust features (PAH emission and silicate absorption), GEP will simultaneously measure redshifts and star-formation rates of millions of galaxies in blind multiband imaging surveys. The technique is summarized in Figure 4.

The mid-IR dust spectrum, measured with GEPs purpose-built array of  $R = 8$  photometric bands, provide a coarse spectrum with PAH fluxes and a redshift estimate ( $\sigma_z = 0.1$  accuracy). The PAH fluxes themselves provide a good proxy for star-formation rate, but the redshift also unlocks the existing far-IR to millimeter-wave legacy datasets, (e.g., those of *Herschel* SPIRE, but also SCUBA/JCMT and soon TolTEC/LMT). With redshifts in hand, these measured fluxes can be converted into high-quality SEDs, fixing unambiguously the star-formation rates in the Kennicutt  $L_{\text{IR-to-SFR}}$  formalism.

The surveys will be conducted in wedding-cake fashion (§2.4.1), and the result will be the first wide-field, dust-immune, redshift-informed survey of star-formation in last 2/3 of the Universe’s history. Depths will reach below  $L^*$  across this period, and will enable us to redraw this portion of the ‘Madau

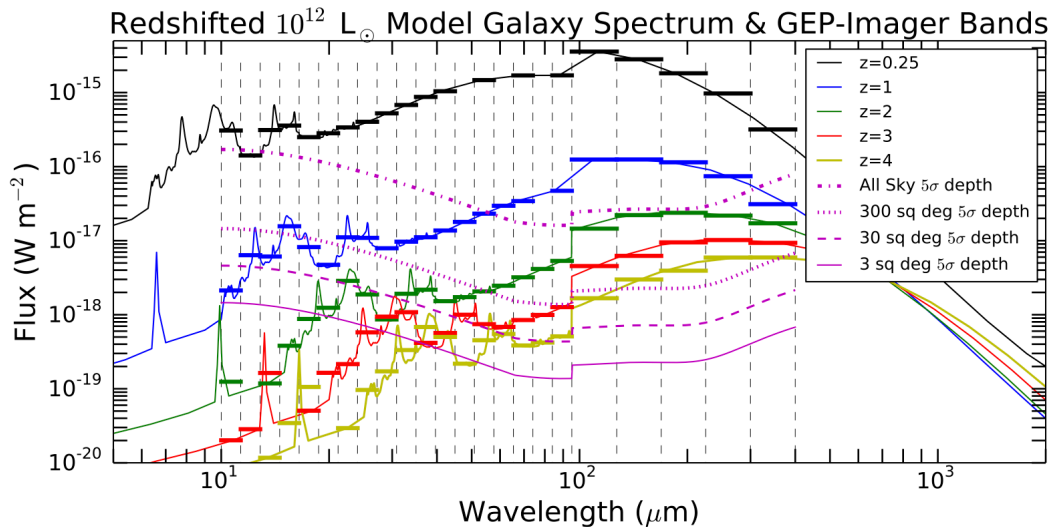


**Figure 4.** GEP will detect  $10^{12} L_{\odot}$  galaxies (corresponding to  $L^*$ ) at  $z = 2$  and higher luminosities at higher redshifts, and will measure photometric redshifts to at least  $z = 4$  (for bright or lensed galaxies). The spectra (from models by [Dale et al. 2014]) display PAH emission lines, silicate absorption at  $10 \mu\text{m}$ , a rising mid-IR continuum from warm dust, and an SED peak just longward of  $100 \mu\text{m}$  from cold dust. The spectra are binned into GEP-I’s wavebands, which are demarcated by dashed vertical lines. The bandwidths change abruptly at  $95 \mu\text{m}$  from  $R = 8$  to  $R = 3.5$  because broad emission lines are not expected to be present for redshift determination. Bright atomic fine-structure emission lines are not shown. Pink lines demark  $5\sigma$  survey depths.

Plot, with better than 0.1 dex uncertainty in enough redshift bins to capture the detailed shape of the star formation history.

### 2.3.2 Early Universe Star-Forming Galaxies Revealed by Gravitational Lensing

**GEP Science Objective 1a** requires GEP-I infrared observations of high-redshift ( $z > 3$ ) galaxies. Understanding the evolution of massive galaxies in the Universe is intrinsically tied to being able to study them at their inception. Dusty star-forming galaxies are the progenitors of massive galaxies and a substantial source of radiation in the universe [Casey et al. 2014]. High-redshift, high star-formation-rate galaxies serve as lenses into the most extreme star-formation environments, and possibly hold the keys to understanding the relationship between supermassive black hole mass and bulge mass [Magorrian et al. 1998; McConnell and Ma 2013]. Despite their luminosities, the origin of these galaxies is unclear: they seem to be the product of both mergers [Chapman et al. 2003] and the manifestation of the extreme star-forming tail from cold accretion [Dekel and Birnboim 2006]. Though these objects exhibit extreme ( $L^* \sim 10^{13} L_{\odot}$ ) luminosities, the majority of that radiation is obscured. In order to detect and understand such objects, IR observations are essential.

Gravitational lensing (in which the gravitational potential of a foreground galaxy bends the light of a background galaxy, thereby magnifying it) will enable GEP-I to vastly increase the number of known dusty high-redshift galaxies (Figure 5). While the redshifts of the majority of lensed galaxies that GEP will detect may be similar those detected by the *Herschel* ( $\langle z \rangle \sim 2.5$ , e.g., [Negrello et al. 2017]), the GEP will also detect an interesting number of much higher redshift galaxies. Based on the number of galaxies detected by the South Pole Telescope (189 sources in 771 square degrees, all believed to be gravitationally lensed—[Mocanu et al. 2013]), GEP is expected to detect 10,000 gravitationally lensed galaxies with mean redshift of  $z = 2$  and tail extending to  $z = 7$ . In the early 2030's, these galaxies will be prime targets for follow-up with 30 m class telescopes in the near-IR and with ALMA.

### 2.3.3 Charting the History of Supermassive Black Hole Accretion

The relation of supermassive black hole mass to stellar bulge mass in galaxies in the local Universe, and the correspondence between the star-formation rate and black hole accretion rate densities to  $z \sim 3$  [Madau and Dickinson 2014], strongly suggest that most galaxies at  $z > 1$  will be composite sources—galaxies with both stellar and accretion energy

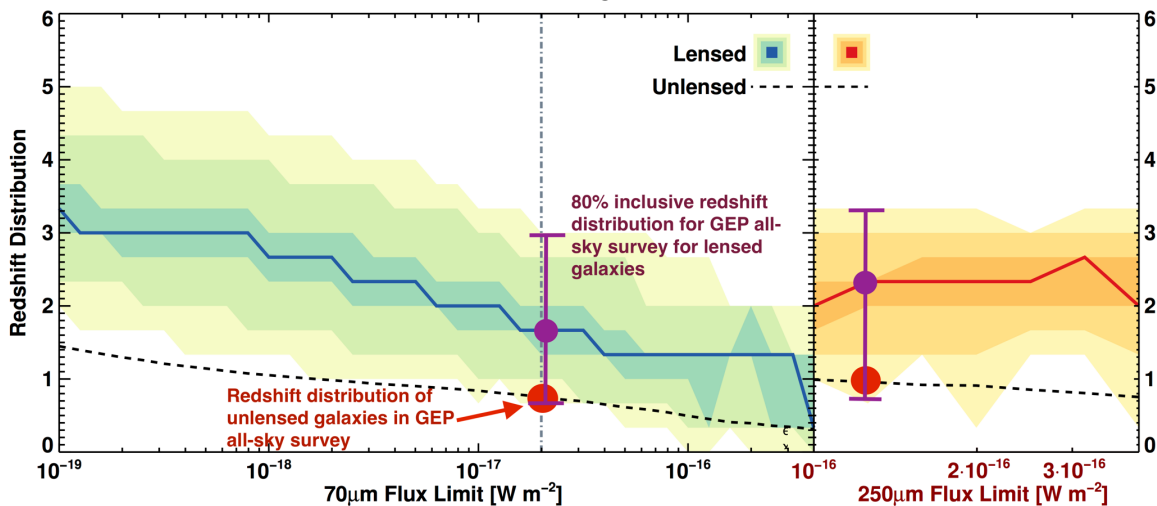


**Figure 5.** GEP will detect 10,000 gravitationally lensed galaxies with mean redshift of  $z = 2$  and tail extending to  $z = 7$ , with photometric redshifts, extending beyond the unlensed galaxy population. Gravitational lensing extends GEP's redshift detection range by a median redshift boost of  $\langle \Delta z \rangle = 1$ . The colors in these plots for GEP-I's 70 and 250  $\mu\text{m}$  bands show the simulated 10, 20, 40, median, 60, 80 and 90 redshift distribution percentiles of lensed galaxies expected to be detected by GEP from models by [Hezaveh and Holder 2011]. The dashed vertical line in the 70  $\mu\text{m}$  panel shows the GEP-I all-sky survey  $5\sigma$  depth;  $\sim 50$  lensed galaxies will also be discovered in the 300 sq deg survey.

sources. Thus, to meet **GEP Science Objective 1a**, GEP will use two techniques to identify buried AGN and to measure their contribution to the total luminosity: decomposition of the multi-band spectrophotometric GEP-I data from the imaging surveys, and GEP-S spectroscopic surveys targeting the high-ionization mid-IR fine-structure lines.

The spectrophotometric distinction compares the PAH features in emission with the rising continuum spectrum generated by hot nuclear dust at 500–1000 K around AGN. The ratio of the PAH emission to the underlying continuum—the PAH Equivalent Width (EQW)—therefore forms an effective diagnostic of the presence of an AGN. AGN have a much warmer dust spectrum than starburst galaxies, with excess emission around 10  $\mu\text{m}$  (starbursts typically peak near at longer wavelengths, near 100  $\mu\text{m}$  in the rest frame). The EQW of the PAH features thus provides a ratio of starburst to AGN power, with starbursts typically having PAH EQW of the isolated 6.2  $\mu\text{m}$  feature of about 0.5–0.7  $\mu\text{m}$ . AGN have much lower PAH EQWs:  $\leq 0.1 \mu\text{m}$ . The PAH EQW is often used in concert with the atomic fine structure line ratios in a diagnostic diagram to identify the power sources in very dusty galaxies—for example, [Genzel et al. 1998; Armus et al. 2007].

As part of our study, the GEP Team has developed a new approach which uses all of the PAH features and continuum in a principal component analysis (PCA). We assess the ability of all 23 GEP-I photometric bands to separate these fundamental components. The goals are: 1) to identify star-formation- or AGN-dominated galaxies; and 2) to extract meaningful information from composite objects where both types of dust

heating make significant contributions to the SED. As Figure 6 (described in the sidebar) shows, the strawman technique applied to model galaxies works extremely well. At least in the framework of this model, the scatter in AGN fraction is about 10%, and this is without using additional legacy far-IR or submillimeter data. With the AGN luminosity in hand for each galaxy, GEP will provide the first dust-immune estimate of black hole accretion history in the last  $\frac{2}{3}$  of cosmic time.

### *Spectral signatures of black-hole accretion*

The rest-frame mid-IR has a number of spectral-line tracers of highly ionized gas, such as [S IV] 10.5, [Ne V] 14.3, 24.3, and [O IV] 25.9  $\mu\text{m}$ , with ionization potentials of 35–97 eV (Table 2).

When ratioed with bright lines with much lower ionization potential (e.g., [Ne II] 12.7  $\mu\text{m}$ ), it is possible to determine the relative amount of heating from young stars and AGN, since the latter provide a much broader input spectrum and, in particular, many more hard photons in the UV and X-ray that raise the ionization state of the gas. [Ne V] emission is seen in the spectra of individual Galactic planetary nebulae [Bernard-Salas et al. 2001; Pottasch et al. 2001], but not in the integrated nuclear (many kpc) spectrum of a galaxy unless an AGN is present. [O IV] can be excited by OB stars, and this line can be seen in starburst galaxies—for example, [Lutz et al. 1998; Smith et al. 2004; Devost et al. 2006], but AGN produce extremely large [O IV]/[Ne II] line flux ratios that are easily identified and used as a extinction-free diagnostic of AGN power (e.g., [Genzel et al. 1998; Armus et al. 2007; Lutz et al. 2003]). The spectral signatures are unambiguous, and while the samples will be smaller, the

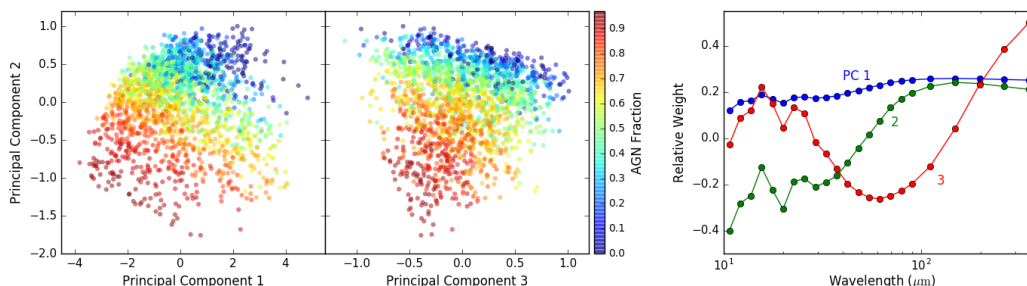


**Figure 6.** GEP-I's multiband observations will enable the relative contributions of galaxy IR luminosities from AGN and SF to be discriminated with 10% precision. *Left:* Outcome for analysis of the 3 sq deg survey at redshift  $z = 1.0 \pm 0.1$  when all GEP bands are detected, but results are similar for other survey depths and subsets of GEP bands provided adequate detection rates. *Right:* Three principle components. Together, they measure the AGN fraction and radiation field hardness (and redshift).

**Table 2.** Large range of ionization potentials accessed by GEP.

Species	Rest Wavelength ( $\mu\text{m}$ )	$z = 2$ Wavelength ( $\mu\text{m}$ )	Ionization Potential (eV)	Traces (SF denotes Star Formation)	Luminosity Relative to $L_{\text{FIR}}$ ( $\times 10^{-4}$ )
[S IV]	10.50	31.50	34.80	SF	...
PAH	11.25	33.75	N/A	SF	10
H <sub>2</sub> S(0)	12.00	36.00	N/A	H <sub>2</sub>	...
[Ne II]	12.80	38.40	21.60	SF	3
[NeV]	14.30	42.90	97.10	AGN	2
[Ne III]	15.60	46.80	41.00	SF/AGN	1
H <sub>2</sub> S(1)	17.00	51.00	N/A	H <sub>2</sub>	0.4
[S III]	18.70	56.10	23.30	SF	2
[Ne V]	24.30	72.90	97.10	AGN	2
[O IV]	25.90	77.70	54.90	AGN/SF	5
H <sub>2</sub> S(2)	28.00	84.00	N/A	H <sub>2</sub>	...
[S III]	33.50	100.50	23.30	SF	3
[Si II]	34.80	104.40	8.20	SF	4
[O III]	51.80	155.40	35.10	SF & AGN	20
[O I]	63.20	189.60	N/A	SF	10
[O III]	88.40	> 193.00	35.10	SF	8
[N II]	122.00	> 193.00	14.50	SF	2
[O I]	145.50	> 193.00	N/A	SF	3
[C II]	158.00	> 193.00	11.30	SF	20

**Measuring AGN Fractions and Radiation Hardness with GEP-I**

The PCA identifies the axes in a high-dimensional data space (here, the 23 GEP-I photometric bands) that minimize the variance in the data, making linear combinations of the GEP-I bands that often correspond to physical quantities. We applied a PCA to the simulated catalog described in §2.4.2. Noise was added to the synthetic observation in each band according to the sensitivity of each of the four GEP-I surveys. Among the objects that are detected at  $5\sigma$  in all bands or a subset of the bands, we use the PCA to assess which physical parameters can be recovered from galaxies that occupy a given 10%-wide redshift bin. Typically, the first principal component corresponds to the bolometric luminosity of objects. The second and third components are generally related to the dust temperature and the AGN fraction of the bolometric luminosity (Figure 6). This is true for most redshifts and survey depths, demonstrating that one can use the GEP bands to separate the AGN contribution from the star-formation contribution to the IR luminosity of galaxies. This can be done when all GEP bands are detected, when only a subset (as few as five) are detected that span the GEP wavelength coverage (e.g., when the PAH features and the dust peak are both detected), and when only the long-wavelength side of the GEP bands are detected (the peak dust emission,  $\lambda > \sim 40 \mu\text{m}$ ).

spectroscopy will provide a check against systematics in the photometric approach described above. GEP will survey 1.5 sq deg with GEP-S, targeting the [O IV] and [Ne II] transitions to depths reaching  $L^*$  at  $z < 2$ , measuring accretion rates in thousands of galaxies.

**2.3.4 Quantifying Feedback Mechanisms and Interstellar Conditions Spectroscopically**

With redshifts in hand from the bright lines in the deep GEP-S spectral survey obtained for **GEP Science Objective 1b**, spectra will be shifted and stacked to measure galaxies' aggregate properties with high SNRs. The stacked spectra will enable utilization of numerous spectral line diagnostics (Table 2). Importantly, the spectra will reveal high velocity ( $\pm 500$  km/s) wings of AGN lines, such as [NeV] and [OIV] that measure the AGN-powered mass outflow rate. With total line flux SNRs in excess of 50 in the stacked spectra, fractional fluxes in the wings (a proxy for mass fraction that is outflowing) can be measured with an RMS of 5% after deconvolution with the spectrometer  $R = 200$  (1500 km/s) response function. The spectral stacks will also reveal the lowest few (at  $z = 1$ ) H<sub>2</sub> rotational transitions that probe shocked gas associated with stellar or AGN feedback.

### Studying Feedback in Detail in Local Systems

GEP-S will be used to study feedback in detail by examining the impact of stellar energy sources on the gas conditions in nearby galaxies (**GEP Science Objective 1c**). GEP will provide a resolved (beamsize  $\ell = 150 \text{ pc} \left( \frac{D}{10 \text{ Mpc}} \right) \frac{\lambda}{24 \mu\text{m}}$ , where  $\sim 10^3$  galaxies have  $D < 10 \text{ Mpc}$ ) study of two key aspects of the cycling of matter and energy between stars, black holes and gas: 1) the mass and energetics of interstellar gas involved in star-formation, which is cooled primarily through the far-IR atomic fine-structure transitions; and 2) outflows and fountains driven by winds from massive stars, supernovae, and active nuclei, pushing material to the outskirts of galaxies and potentially regulating star-formation activity. This census of ISM phase as a function of local galactic environment will resolve whether ISM conditions are set by hydrostatics and the local stellar population [Wolfire et al. 2003; Ostriker et al. 2010] or by local feedback effects, e.g., [Walch et al. 2015].

Star-forming interstellar gas cools principally through the [C II] transition, and [C II], along with the  $122 \mu\text{m}$  [N II], transition provide a clean discrimination between neutral atomic and ionized material. The addition of the doubly ionized oxygen transitions ([O III]) at  $52$  and  $88 \mu\text{m}$ , and the doubly ionized nitrogen transition ([N III]) at  $57 \mu\text{m}$  provides: 1) a measure of the UV field hardness, thus constraining the stellar mass function; and 2) the density in the HII regions, thereby measuring the ISM pressure. However, the existing nearby galaxy measurements, from *ISO*, *Herschel*, and *SOFIA*, suffer from small sample sizes and relatively poor surface brightness sensitivity, which translates to a column density threshold below which material is simply not detected.

With its sensitive, long-slit spectrometers, GEP-S offers both orders of magnitude improvement in mapping speed and exquisite surface brightness sensitivity. GEP-S will use [C II] as a tracer of very low column density material, reaching 10–100 times below what can be done with a Jansky VLA deep HI 21 cm survey. This depth is important because it enables a census of material below the star-formation threshold of  $1\text{--}10 \text{ M}_\odot/\text{pc}^2$  [Martin and Kennicutt 2001; Schruba et al. 2011]. According to current modeling, this low-surface brightness is expected to lie in the outskirts of galaxies, propelled

by massive star and supernova-driven winds. Figure 7 shows an example simulation from the model described in [Walch et al. 2015]. In it, a bubble is forming in the star-forming atomic gas as much of it is pushed above and below the Galactic plane on a timescale of 70 million years.

Outstanding GEP-S surface brightness sensitivity will also be used to map the ionized gas density and photon flux (using the [N II] lines) and hardness (using the [N III] and [O III] lines), even in diffuse H II region material where [CII] is sub-thermally excited. Additionally, GEP-S will map molecular material with a powerful probe that is unique to the far-IR: HD, a chemical analog of  $\text{H}_2$ . Its rotational fundamental band at  $112 \mu\text{m}$  will provide a metallicity-independent molecular gas mass estimate to a depth of  $\sim 30 \text{ M}_\odot/\text{pc}^2$ . While HD has been detected in a few nearby protoplanetary

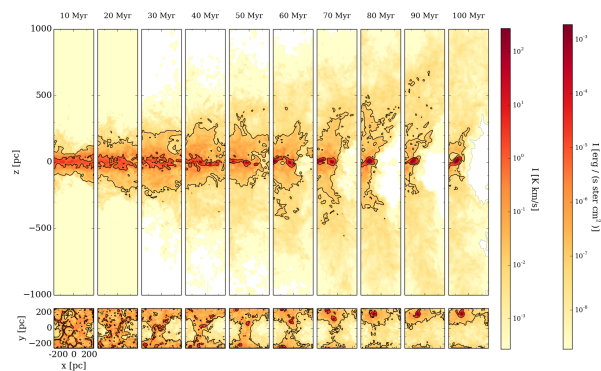


**Figure 7.** Long-slit GEP-S observations of nearby galaxies will detect extraplanar gas from interstellar bubble formation and blowout. As this simulation of gas erupting from a disk over 100 Myr in ten 10 Myr intervals (from left to right) shows, gas reaches kpc heights and emits in optically thin [CII]. GEP-S’s beamwidth  $\theta_{\text{beam}}$  is  $\sim 400 \text{ pc}$  at a galaxy distance of 5 Mpc (about the distance of M83,  $\sim 1.5\times$  the distance of M82) for  $[\text{CII}] = 158 \mu\text{m}$ ; thus, the width of each panel corresponds to approximately to the slit width. GEP-S can detect even the faintest emission in these simulated [CII] maps. This low-surface brightness material is impossible to detect with *SOFIA*, or even optimized balloon experiments, which would be limited to values on order  $10^{-6} \text{ erg/s/ster/cm}^2$  -- material restricted to the plane and not the blowout. Simulations from S. Walch (personal communication, see [Walch et al. 2015]).

disks with *Herschel*, with GEP-S it will be detectable in typical Galactic ISM sightlines.

### 2.3.5 Evolution of the Star-Forming Interstellar Medium Over Cosmic Time

To assess the evolving conditions in star-forming galaxies since redshift  $z = 2$  (**GEP Science Objective 1d**), a wide-field spectroscopic survey overlapping with the spectral fields of WFIRST and/or Euclid will be used. The 3-D position priors of thousands of galaxies per square degree provided by the near-IR will enable spectral stacks of the GEP mid- and far-IR spectra. The result will be high-SNR aggregate spectra binned in redshift and luminosity (survey details are in §2.5.1). These spectra will carry a host of the diagnostics summarized in Table 2, which in aggregate decode the properties of the gas in galaxies regardless of their dust content. The spectra will measure the mass of dense, photo-dissociated atomic gas (via [O I]), the mass of ionized gas (via [Ne II], [N II]), the stellar UV radiation field hardness (via [N III]/[N II], [O IV]/[O III]), the average accretion luminosity of AGN (via [Ne V]) and the density of gas around young stars (via the [O III] line pair.)

### 2.3.6 Heavy Element Production in the Hearts of Galaxies

**GEP’s Science Objective 2** is to measure the growth of metallicities of galaxies. The chemical complexity of the modern Universe, in particular the presence of planets and life, are only possible with the heavy elements, such as carbon, nitrogen, oxygen, and iron. These elements are only formed in stars, so the heavy element contents of the Universe at any given epoch is closely related to the integrated star-formation activity prior to that time. A complete history of the Universe’s heavy element production cannot rely solely on measurements of the intergalactic gas (typically probed with UV absorption spectroscopy, see [Tumlinson et al. 2017]), but must also chart the metallicity within galaxies, where the heavy elements are forged, then distributed to the rest of the Universe with unknown efficiencies.

The metallicity *within* galaxies, where stars, planets and eventually life arise, is not reliably measured with the presently used optical/UV techniques. These short-wavelength diagnostics suffer from two fundamental limitations: First, dust obscuration means that UV/optical spectroscopy does not penetrate the bulk of galaxies; they probes

only low-extinction regions, which represent only a fraction of the total star-formation activity (Figure 1). This may result in substantial underestimates: [Santini et al. 2010] infer a metallicity using far-IR dust measurements (*Herschel* photometry) that is more than 10 times higher than that inferred from optical nebular lines. Second, while they produce consistent *relative* metallicity measurements in local low-extinction systems, the optical diagnostics have large systematic uncertainties—for example [Fernández-Ontiveros et al. 2017; Kewley and Ellison 2008]. Additionally, because they are optical transitions, many of the diagnostics are temperature sensitive and electron temperatures in HII regions are hard to measure and spatially variable.

The far-IR atomic fine-structure lines accessible to GEP offer metallicity measurements that overcome these limitations because they can access both obscured and unobscured galaxy populations through the bulk of cosmic time. Two diagnostics will be employed. For the last half of the Universe, GEP will use the O to N ratio as a measure of stellar processing. While oxygen is a primary nucleosynthesis product, nitrogen is a secondary product—it results from both shell burning and core burning. The O/N ratio thus decreases with increased processing and provides a proxy for metallicity for values above 0.2 solar [Groves et al. 2004]. As [Nagao et al. 2009] have shown (Figure 8), the O/N ratio is measured cleanly in HII region gas with the suite of two [O III] transitions (52 and 88  $\mu\text{m}$ ) and one [N III] transition (57  $\mu\text{m}$ ). These two ions have a very similar ionization potential and the use of the two OIII transitions removes the dependence on electron density. These transitions are bright and will be detectable in  $3 \times 10^{11} L_{\odot}$  galaxies for  $z \leq 1.2$  with GEP-S. Thousands of galaxies will be detected in the 100-square-deg blind spectroscopic survey. This line ratio will also be clearly revealed in many of the stacked spectra generated from the WFIRST near-IR grism fields (§2.5.1 and §2.5.3).

For higher redshifts and lower metallicities, GEP will chart the relative metallicity evolution using the neon to sulphur ratio. This technique uses the fact that neon is inert, so it remains unadulterated in the gas phase with its abundance tracking metallicity, while sulphur is partially depleted onto grains as dust forms, so its abundance grows more

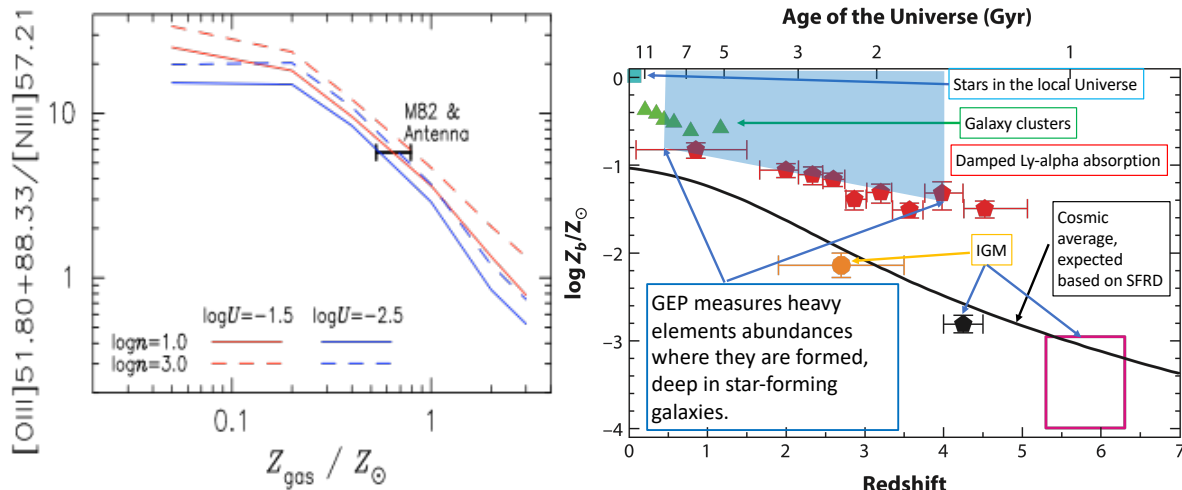


**Figure 8.** *Left:* Cosmic metal abundance measurements, reprinted from [Madau and Dickinson 2014] with annotations added. Heavy elements are forged in galaxies, and enrich the intergalactic material through feedback processes that are poorly understood. Comparing the metallicity within galaxies’ interstellar media to the absorption measurements reveals the timescale and degree to which the intergalactic is enriched with high-metallicity gas. Optical metallicity indicators carry large uncertainties, in large part due to de-weighting high-extinction regions. *Right:* GEP will access the IR [O III] and [N II] line triplet metallicity diagnostic in thousands of galaxies for the last two-thirds of cosmic time, anchoring the metallicity in the hearts of galaxies. Figure reprinted from [Nagao et al. 2009]. Prior to GEP, these lines could only be accessed by low-redshift galaxies, such as M82 and the Antennae (NGC 4038/9).

slowly than linear with metallicity. The empirical relation, calibrated carefully with *Spitzer* Infrared Spectrograph measurements of 47 local-Universe galaxies is [Fernández-Ontiveros et al. 2016]:

$$\text{Log}_{10} \left\{ \frac{([Ne III] 15.6 + [Ne II] 12.8)}{([S IV] 10.5 + [S III] 18.7)} \right\} = 0.037 + (0.53 \pm 0.32) \text{Log}_{10} \left( \frac{Z}{Z_{\odot}} \right).$$

With GEP-S, GEP will observe these transitions in 300 directly targeted galaxies (20 each in 15 redshift bins) between  $z = 1.2$  and 4. The highest-redshift bins will require approximately 4-hours integration per source.

The PAH spectra of galaxies can provide a complementary probe of metallicity. As PAHs are composed primarily of carbon and hydrogen, they likely originate in outflows from C-rich AGB stars. In this picture, a galaxy must have a substantial AGB population, requiring a few 100 million years of main sequence evolution, in order to host appreciable PAH emission. Thus, a correlation is expected between the age of the stellar population and the abundance of PAHs [Galliano et al. 2008]. Since timescales for AGB evolution are longer than that of Type II supernovae production, this may manifest itself as a systematic evolution in the ratio

of PAH luminosity per IR luminosity with cosmic time. GEP will determine this ratio for a large number of galaxies to test this paradigm and construct a quantitative picture of the lifecycle of PAHs. For example, when in the evolution of a galaxy the PAH emission becomes an appreciable part of the total IR emission.

## 2.4 Perceived Scientific Impact of the GEP: Additional GEP Science

### 2.4.1 Linking Star-Forming Galaxies to the Universe’s Dark Matter Skeleton

Large-scale structure measurements reveal the environments that galaxies occupy. Specifically, the strength of clustering exhibited by a population of galaxies on large scales is directly related to the masses of the dark matter halos that they inhabit. Previous IR surveys covered small volumes and could not probe the correlation of large-scale structure and star-formation over a comprehensive range of environments.

By encoding 3-D positions for millions of star-forming galaxies, GEP will provide high-SNR measurements of the clustering of star-forming galaxies in large enough volumes to overcome sample variance from  $0 < z < 2$ , down to luminosities

of  $L_* = 10^{12} L_\odot$  at  $z = 2$  (and lower  $L$  at lower redshift). This will reveal the masses of the dark matter halos occupied by galaxies as a function of luminosity, SFR, and redshift. The GEP surveys will provide star-formation rates that will be complementary to surveys of LSST, WFIRST, and Euclid that select primarily based on stellar mass.

While the photometric redshifts obtained by GEP-I will be insufficiently precise to measure 3-D correlation functions of galaxies, they can be used to measure projected correlation functions in several redshift windows with  $\Delta z \sim 0.2$ . Figure 9 shows expectations for the clustering of GEP-selected galaxies based on our mock catalogs. The top panel shows the expected projected correlation functions for samples selected by stellar mass and by SFR.

Figure 9 shows that, while clustering strength is a strong function of stellar mass, it depends less strongly on SFR. This is a clear, testable prediction of galaxy formation models: samples selected by SFR occupy a broad range of halo masses, so their clustering does not exhibit a strong dependence on the selection threshold. GEP will therefore be able to test if bursts of star formation happen over a wide range of halo mass as predicted by models, and test how environment affects bursts of star formation. This key prediction from models has previously not been measured accurately: GEP will make these measurements for the first time over a wide area.

#### 2.4.2 Background on PAHs, Chemistry and Physics of the Star-Forming ISM

PAH lines carry several percent of the bolometric luminosities of star-forming galaxies and are ubiquitous in star-forming galaxies. PAHs are molecules with tens or hundreds of atoms, arranged with carbon atoms in a graphene-like planar structure and hydrogen atoms on the peripheries at incomplete bonds. PAHs are stochastically heated by single UV photons, resulting in mid-IR line emission that provides a direct measure of the UV photon flux. In the rest frame, strong PAH emission lines occur at  $3.3 \mu\text{m}$  (C-H stretching mode),  $6.2$  and  $7.7 \mu\text{m}$  (C-C stretching modes),  $8.6 \mu\text{m}$  (C-H in-plane bending mode), and  $12$  and  $13.5 \mu\text{m}$  (C-H out-of-plane bending modes). There is a complementary silicate absorption feature at rest-frame  $10 \mu\text{m}$ . GEP-I's  $R = 8$  imaging bands are matched to the PAH line widths to enable redshift measurements from  $z = 0$  to  $z > 5$  (for very luminous and

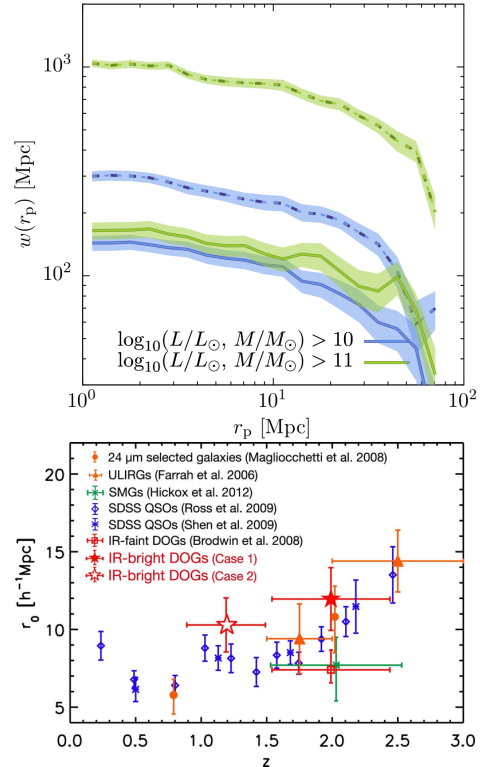


**Figure 9.** *Top:* Projected correlation functions from our mock catalog for galaxies selected by bolometric IR luminosity (solid lines) and stellar mass (dashed lines) in a  $1.0 < z < 1.2$  redshift slice. Bands indicate the expected uncertainties for the 30 square degree survey. Galaxy mass correlates strongly with halo mass, leading to a strong dependence of clustering strength with mass. Conversely, bolometric IR luminosity (which indicates star-formation rate) is weakly correlated with halo mass (even galaxies in low mass halos can have occasional strong starbursts), leading to a weak dependence of clustering strength on IR luminosity. GEP will test this predicted difference in clustering dependence on mass and star-formation rate. *Bottom:* A compilation of measured correlation lengths for dust-obscured (star-forming) galaxies and QSOs from [Toba et al. 2017] showing that such galaxies become more strongly clustered with increasing redshift. GEP's redshift reach will extend well beyond Spitzer's.

gravitationally lensed galaxies) as illustrated in Figure 4.

PAHs are expected to be present in star-forming galaxies wherever dense molecular ISM is present and a first generation of massive metal-producing stars has lived, similar to interstellar dust. Although

JWST lacks of the field of view and slew rate to observe large areas in depth, detailed JWST studies of rest-frame mid-IR spectra of star-forming galaxies will clarify PAH physics that will maximize the scientific return of GEP.

### High-Redshift Interstellar Chemistry with PAHs

GEP will provide a rich sample of PAH spectra across a range of redshift, SFR, IR luminosity, and metallicity. These spectra will be used to determine how the PAH emission in high redshift galaxies systematically evolves as a function of each. Relative changes in the PAH spectrum, such as trends in the various feature ratios, provide a window into changes in the structure of PAHs and their interstellar environments (see [Tielens 2008] for a review). For example, one of the most robust conclusions of detailed modeling of PAH emission physics is the dependence of the 6.2 to 11.2  $\mu\text{m}$  ratio on the PAH charge. In turn, this is a probe of the intensity of radiation able to ionize PAHs and the abundance of free electrons. Analysis of features of the PAH spectra (GEP-I and GEP-S) in conjunction with emission in various atomic lines (GEP-S), will enable construction of a detailed statistical picture of the chemistry and physical conditions in the ISM of high redshift galaxies.

### Star-Formation Conditions in the Milky Way and Nearby Galaxies

With the all-sky GEP-I survey, GEP will probe the ISM conditions over a large range of interstellar environments, from the Galactic Center, to the Milky Way's 4 kpc molecular ring and less molecular gas-rich outer Galaxy, to the disks and nuclei of nearby galaxies. Collectively the dust spectral shapes, PAH features relative the continuum, and far-IR atomic fine-structure lines are sensitive interstellar mass, dust temperature, UV radiation field, and density (Figure 10). While PAH emission features vary little on galaxy-wide scales, they do vary on small scales and source-to-source, such as in protoplanetary disks and post-asymptotic giant branch stars (e.g., [Peeters et al. 2002]). This is because they are sensitive to variations in the composition of the PAH molecular family, which are driven by chemical evolution, and ultimately by changing physical conditions. GEP-I's observations of the Milky Way will probe the chemical evolution and physical conditions in Galactic regions on an object-by-object basis.

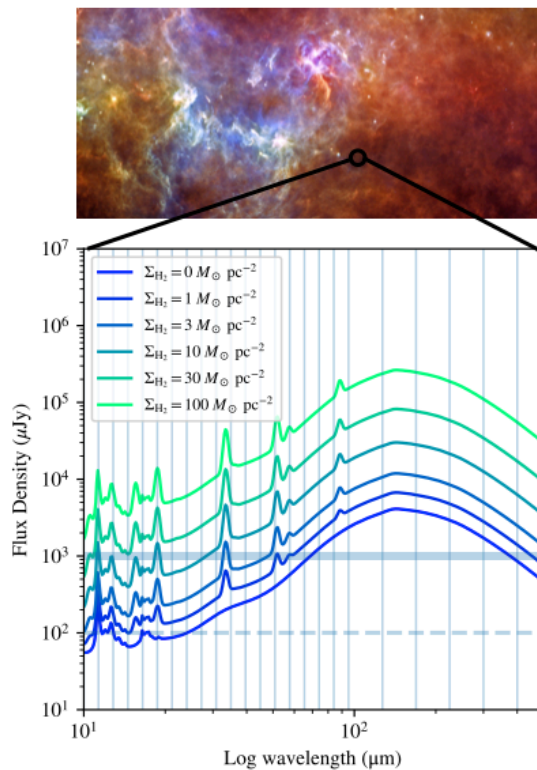


**Figure 10.** GEP-I will provide spatially resolved SED mapping across the star-forming ISM over  $10^{7.5}$  lines of sight in the Milky Way and nearby galaxies, providing a large data set to understand how local environment establishes ISM conditions. This figure shows how the dust emission from the Aquila molecular cloud (top) would be mapped into spatially resolved SEDs (bottom) over the GEP-I bands with flux density estimates in 3" apertures. The curves correspond to the expected signatures for varying levels of molecular gas in a stellar population with  $\Sigma_{\star} = 300 M_{\odot} \text{pc}^{-2}$ . Vertical lines indicate GEP-I band edges. The horizontal lines indicate the approximate  $5\sigma$  depths of the all-sky survey (solid) and 300 sq deg survey (dashed). Iconic star-forming regions in the Local Group are significantly brighter: Orion, 30 Dor, and NGC 604 would all peak above the top of the figure.

**Table 3.** GEP science objectives and surveys matrix (SF = star formation, BH = black hole).

Objective		GEP-I Surveys				GEP-S Surveys		GEP-S Pointed	GEP-S Mapping
		3 Sq Deg	30 Sq Deg	300 Sq Deg	All Sky	1.5 Sq Deg	100 Sq Deg		
1a	SF/BH Survey								
1b	BH Feedback								
1c	Local Feedback								
1d	ISM Conditions								
2	Heavy Elements								
			Principal Dataset						
			Auxiliary Dataset						

## 2.5 Science Yield: Observations and Measurements with Science Yield Estimates

### 2.5.1 Descriptions of Imaging and Spectroscopic Surveys

GEP is designed to be a dedicated survey mission. It will provide a legacy dataset with broad utility for studying the evolution of star-formation and black hole growth in galaxies, while maximizing the science within the Probe cost cap. The surveys enable multiple science objectives (Table 3).

GEP-I photometric survey program for **Science Objective 1a** is optimized to sample a comprehensive range of redshifts and galaxy luminosities using multiple depths and areas (Table 4). A combination of four depths and areas will sample low redshift and bright, rare galaxies, faint, high-redshift galaxies, and intermediate redshift and luminosity galaxies. Sufficient numbers of galaxies will be detected so that Poisson statistics

will not be limiters and sufficient volumes will be surveyed so that sample variance is not a limiter (Figure 11, left panel). For Science Objective 1a, the wide and deep surveys should be >100 and >10 square degrees, respectively. Figure 11 (right panel) shows the depths each survey is projected to reach as a function of wavelength for the GEP-I bands. All of the surveys except the all-sky survey will be centered on and divided between the north and south ecliptic poles to minimize the photon backgrounds from primarily zodiacal dust and secondarily Galactic dust [ISRA 2018]. This will provide overlap with Euclid surveys, which will provide near-IR counterparts and stellar masses of galaxies for combined studies, and ground-based observatories in both hemispheres.

Three types of spectroscopic measurements with GEP-S will complement GEP-I photometric surveys: 1) Individual observations of specific galaxies identified in the photometric surveys to provide precise redshifts and to validate the photometric techniques (**Science Objectives 1a**),

**Table 4.** GEP Galaxy Survey Yields.

Instrument	Area or Targets	Depth	Region	Number of Galaxies	Number of Redshifts	Science Objectives
GEP-I	3 sq deg	10 $\mu$ Jy	Ecliptic Poles	10 <sup>6</sup> above confusion noise	10 <sup>5</sup>	1a
GEP-I	30 sq deg	30 $\mu$ Jy	Ecliptic Poles	10 <sup>6</sup> above confusion noise	2 × 10 <sup>5</sup>	1a
GEP-I	300 sq deg	100 $\mu$ Jy	Ecliptic Poles	10 <sup>7</sup> above confusion noise	5 × 10 <sup>5</sup>	1a
GEP-I	All sky	1 mJy	N/A	10 <sup>8</sup> above confusion noise	10 <sup>6</sup>	1a
GEP-S	1.5 sq deg (GEP-DSS)	7 × 10 <sup>-20</sup> W m <sup>-2</sup> at 100 $\mu$ m	Ecliptic Poles	2 × 10 <sup>4</sup> galaxies between z = 1 and 2	2 × 10 <sup>4</sup>	1a, 1b, 2
GEP-S	100 sq deg (GEP-WSS)	3.5 × 10 <sup>-19</sup> W m <sup>-2</sup> at 100 $\mu$ m	Overlap with WFIRST / Euclid grism fields	Blind detections of ULIRG-class galaxies z = 1 - 2. Also use stacks via near-IR priors: 4 × 10 <sup>5</sup> galaxies.	Several × 10 <sup>4</sup>	1d
	Same, intensity mapping for P(k), multiple z bins		N/A	N/A	N/A	1a, 1b, 1d, 2
GEP-S	Galaxies from GEP-I surveys at z = 1.2 - 3	3 × 10 <sup>-20</sup> W m <sup>-2</sup>	Distributed across sky, up to 6 hrs / galaxy	300	N/A	2
GEP-S	Local galaxy mapping	1 × 10 <sup>-10</sup> W m <sup>-2</sup> ster <sup>-1</sup> at 122 $\mu$ m	8' × 8' regions in 400 galaxies, 15 sec integration / beam		N/A	1c

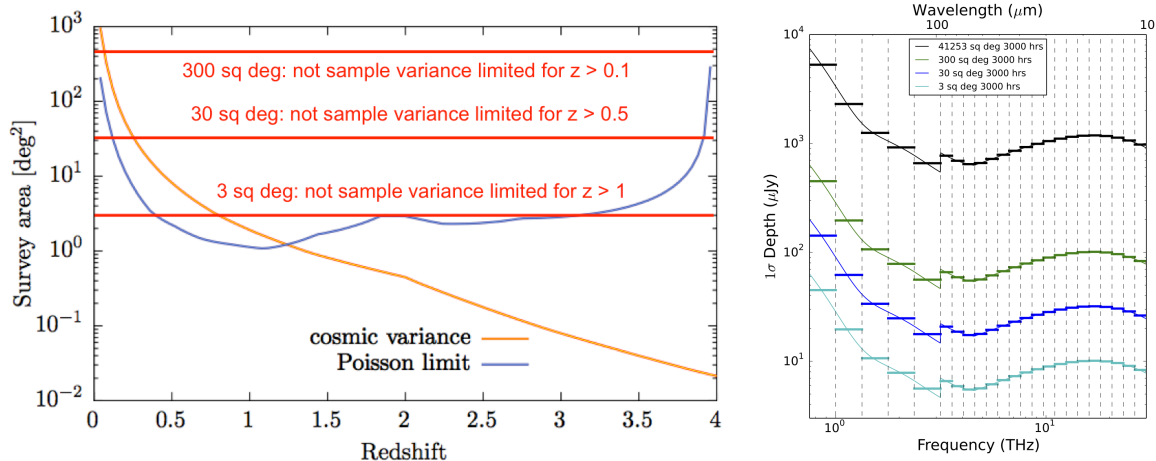


**Figure 11.** *Left:* GEP-I’s ‘wedding-cake’ survey will not be cosmic sample variance limited in the goal redshift ranges. It also will not be limited by Poisson statistics - the blue line shows the area needed such that Poisson errors allow a 10% accurate measurement of the slope of the luminosity function at the faint end. *Right:* With its 2.0 m, 4 K aperture, GEP-I’s surveys will reach unprecedented depths. GEPs band edges are shown as vertical dashed lines and the  $1\sigma$  survey depths are shown with thick horizontal lines in each band. *With its small field of view and long slew times, JWST will be unable to do surveys of GEPs magnitude.*

and to obtain high SNR measurements of the full suite of far-IR spectral features (**Science Objective 2**). 2) ‘Blind’ field-filling spectroscopic surveys obtained by rastering GEP-S on the sky (**Science Objectives 1a, 1b, and 1d**). 3) Spectral maps of nearby galaxies (**Science Objective 1c**). As summarized in Table 4, GEP-S will perform a deep spectroscopic survey over 1.5 square degrees and a wide spectroscopic survey over 100 square degrees. With its long-slit spectrometers with 40–70 spatial beams, GEP-S is more efficient in performing blind spectral surveys than SPICA, which is limited to a few beams in the slit.

The spectral survey datasets will be used in three ways. First, they will detect galaxies by the thousands and tens of thousands directly in the FIR fine-structure transitions (and the continuum, when binned). Second, the wide survey will be used to stack on the WFIRST and/or Euclid grism sources as described in §2.5.3 to provide high-SNR average galaxy spectra in bins. Finally, both surveys will be excellent datasets for line intensity mapping that will measure the total cosmic luminosity density in the various far-IR lines and ratios among line intensities (§2.5.4).

### 2.5.2 Expected Numbers of GEP-I Galaxies, Luminosity Functions, and Precision of Photometric Redshifts

In this subsection, GEP-I yields are summarized, and then the techniques – simulations generating images and mock catalogs – that were used to estimate the yields are described. First, GEP-I’s surveys will detect tens of millions of galaxies and measure photometric redshifts for millions of them (Figure 12). Second, GEP’s **Science Objective 1a** requires luminosity functions of galaxies over a range of redshifts. Integrated star-formation rates, as shown in Figure 1, are insufficient to describe galaxy evolution: the galaxy luminosity functions should be characterized as a function of redshift to observe the changes in galaxy formation and the build-up of stellar mass over cosmic time. This will relate star formation to the growth of cosmic structure via dark matter gravitation. Specifically, faint-end (below  $L^*$ ) mid- and far-IR luminosity function slopes have not been measured above  $z = 0.5$  and there is disagreement about the faint-end slopes even at  $z \sim 0$ . With GEP-I surveys, faint-end slopes below  $\text{Log}_{10}(L_{\text{IR}}/L_{\odot}) = 11$  for  $z = 0.5$ , below  $\text{Log}_{10}(L_{\text{IR}}/L_{\odot}) = 11.5$  at  $z = 1$ , and below  $\text{Log}_{10}(L_{\text{IR}}/L_{\odot}) = 12$  at  $z = 2$ , will be measured. Figure 13 shows current observational determinations of the IR bolometric luminosity function, and compares

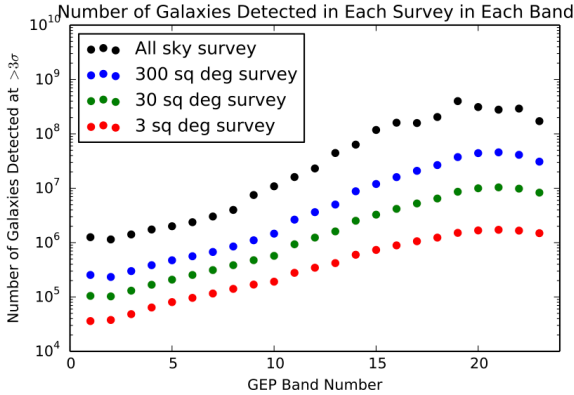


**Figure 12.** GEP will detect tens of millions of galaxies, measure photometric redshifts for millions of them, and measure their AGN fractions. The plot shows the number of galaxies that will be detected by GEP-I at greater than  $3\sigma$  significance in each band independently.

these to a sample luminosity function derived from our mock GEP catalogs. *GEP will represent an enormous step beyond the state of the art in detections of large numbers of star-forming galaxies, cosmological volumes probed, and resolution of the SEDs.*

Third, GEP-I requires photometric redshifts with precision  $\leq 10\%$  to  $z = 2$ , a requirement that is achieved with margin. For the cases of strong PAH features, the photometric redshift uncertainty is set by the width of the GEP-I bands relative to the widths of the PAH features.

Uncertainties in photometric redshifts were estimated by adding noise to the [Dale et al. 2014] model spectra according to each of the map depths given the photon backgrounds. The spectra were binned into the GEP-I bands and  $\chi^2$  were calculated by comparison to the spectral model and comparison to two other spectral models. Since the spectra of galaxies will not be known a priori, the comparison models were used to ascertain the uncertainty incurred by having a spectrum different from the model. Only the first ten GEP-I bands were used for the photometric redshift measurements because the steeply rising mid-IR dust spectra influences the redshifts and the dust temperatures will not be known a priori. The nominal model had strong PAH emission features and the comparison models had: 1) strong PAH emission features but cooler dust (hence a more slowly rising spectrum with wavelength); and 2) hot dust that substantially

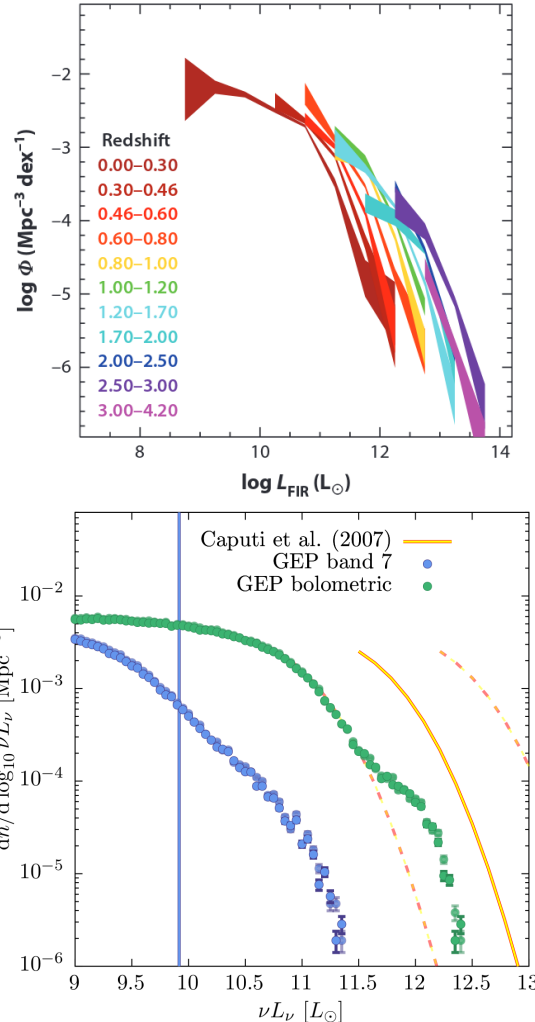


**Figure 13.** *Top:* Current observational determinations of the bolometric IR luminosity function from [Madau and Dickinson 2014]. *Bottom:* GEP luminosity function for  $1.0 < z < 1.2$  derived from the Galacticus mock catalogs assuming a  $\sigma_z = 0.1$  uncertainty on galaxy redshifts. Error bars are estimated assuming Poisson statistics scaled from the 4 sq deg area of our mocks to 30 sq deg. Blue points show the luminosity function in the GEP-I band 7 (21.2 to 24.0  $\mu\text{m}$ ), while green points show the bolometric IR luminosity function for reference and comparison to the top panel. (The bolometric luminosity function is not shown below  $10^9 L_\odot$  because it becomes incomplete due to the resolution of the simulation.) Blue line is  $3\sigma$  detection limit. Faint points indicate the luminosity function that would be obtained if spectroscopic redshifts were available; it is almost indistinguishable from that constructed using photometric redshifts.

overwhelmed the PAH features above 10  $\mu\text{m}$ . The results were as follows:

- Photometric redshifts are obtainable for  $10^{11}$   $L_{\odot}$  galaxies to  $z = 1$  in the 3 sq deg survey and to  $z = 0.5$  in the 30 sq deg survey, with  $\sigma_z \leq 0.1$ .
- Photometric redshifts are obtainable for  $10^{12}$   $L_{\odot}$  galaxies to  $z = 2$  in the 3 sq deg survey and to  $z = 1$  in the 30 sq deg survey with  $\sigma_z \leq \sim 0.1$ , and sometimes (depending on the spectrum) to  $z = 3$  in the 3 sq deg survey to  $1 \sigma_z \leq 0.15$ .
- Photometric redshifts are attainable for  $10^{13}$   $L_{\odot}$  galaxies to  $z = 4$  in the 3 sq deg survey and to  $z = 2$  in the 300 sq deg survey to  $\sigma_z \leq \sim 0.1$ .
- The photo- $z$  uncertainties are a function of redshift, galaxy luminosity, map depth, and strength of the PAH features relative to the continuum.
- The photo- $z$ s are only robust if the PAH features stand out above the dust continuum. Thus, in the case of very hot dust, which represents an extreme case, the photo- $z$ s have large uncertainties. However, even in the case of very hot dust, photo- $z$ s become detectable at  $z > 2$  for deep surveys and luminous galaxies because the dust continuum is not strong below rest-frame 10  $\mu\text{m}$ , which is redshifted well into the GEP-I bands.
- There is a bias of photometric redshift to lower values than the model by a few percent due to the rapidly rising dust spectrum in the mid-IR. This will be characterized and accounted for with simulations.

There is significant room for optimization in the photometric redshift measurements, however,  $1\sigma_z = 0.1$  was adopted to be conservative. The photometric redshift uncertainty estimations will be refined further for a Phase A study.

To quantify the science yield of the GEP-I survey program, a mock GEP-I survey was constructed using a combination of the Millennium N-body simulation [Springel et al. 2005], to provide the distribution of large-scale structure, and the Galacticus semi-analytic model [Benson 2012], to populate that simulation with galaxies based on physical models. For each dark matter halo in the simulation volume, the star-formation rate and black hole accretion rate of the galaxy was computed. Bolometric IR luminosities due to star-formation

were estimated as  $L_{\text{IR}} = 2.6 \times 10^{45}$  (SFR/ $M_{\odot}$  yr $^{-1}$ ) ergs/s [Calzetti 2013], and those due to AGN activity as  $\epsilon M_{\odot} c^2$  (with  $\epsilon$  being the radiative efficiency computed by Galacticus from the black hole spin and accretion rate). IR spectra with the corresponding AGN fraction were then assigned to galaxies using the models of [Dale et al. 2014] and normalized to give the computed total IR bolometric luminosity. The dust temperatures were drawn from a Gaussian distribution chosen to give the best match to measured IR number counts. These spectra were then used to compute broadband luminosities for model galaxies in each GEP-I band. Finally, a light cone from this synthetic catalog was extracted, corresponding to a 4 square degree area, from  $z = 0$  to 3, and determined observed fluxes in all GEP-I bands for each galaxy.

The galaxy number counts estimated in this way are lower limits because these (and other) galaxy evolution models generically underpredict the number of very high luminosity galaxies ( $\sim 10^{13}$   $L_{\odot}$ ; for example, [Benson et al. 2003]). Although we attempted to tune the Galacticus model number counts to match observations from *Spitzer* and *Herschel* by judiciously choosing from the [Dale et al. 2014] spectral library, at high flux densities (i.e.,  $> 1$  mJy at 160  $\mu\text{m}$ ) the model counts are almost an order of magnitude too low compared to observations. The agreement is much better at 24 and 70  $\mu\text{m}$ , coming close to matching observations. Some of the bright observed galaxies likely result from gravitational lensing (§2.3.2), but lensing is unlikely to account for the majority of the discrepancy. We adopt our model predictions for the detection rates with the understanding that they are likely conservative.

### 2.5.3 Stacking Analyses

Survey spectroscopy with GEP-S is a particular strength of the GEP long-slit spectrometer architecture (see Figure 14). Tens to hundreds of thousands of galaxies will be detected blindly in the GEP-S surveys (GEP-WSS and GEP-DSS), but these surveys will be especially powerful when combined with ancillary datasets. Specifically, stacking on grism spectrometer datasets from Euclid and WFIRST define the observations to accomplish **Science Objective 1d**. The slitless grism modes on Euclid and WFIRST will utilize the 1.2-1.8  $\mu\text{m}$  imaging cameras with the addition of dispersion at

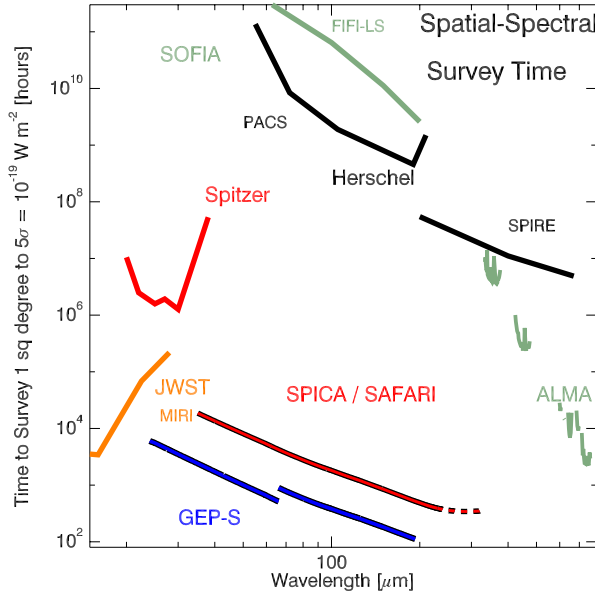


**Figure 14.** Spectral survey time to a given depth (lower is faster) in the far-IR. The spectrometer modules in GEP-S offer gains of 5-6 orders of magnitude relative to the current state of the art (*Herschel* and *SOFIA*). The GEP-S speed exceeds that of *SPICA* because of the larger detector format that enables true long-slit spectrometers.

moderate-resolution ( $R \sim$  few hundred) over large fields. Observation at multiple telescope boresight angles rotates the spectra with respect to the field and enables extraction of object-by-object spectra. The wavelength range corresponds to the  $H\alpha$  redshifts of approximately  $z = 1$  to 2.

Various groups have offered preliminary estimates of yields from the putative surveys; a particularly good recent reference is [Merson et al. 2018], which estimates  $H\alpha$  luminosity functions from the *Galacticus* model [Benson 2012]. These expected yields enable estimates of the density of detected galaxies for various GEP-S survey parameters (Table 5). As the table shows, the survey areas are large with tens of millions of  $H\alpha$  detections expected. GEP will use the near-IR 3-D positions as templates to stack both spatially and spectrally to provide high quality, aggregate far-IR spectra of

many bins in luminosity and redshift. Examples of stacked far-IR spectra already exist. [Wilson et al. 2017] used all available data in the *Herschel* SPIRE spectrometer archive – 197 galaxies covering rest wavelengths of 200 to 650  $\mu\text{m}$  (most with redshifts  $< 0.5$ ) – and the ALMA spectrum presented in [Spilker et al. 2014], generated with a stack of 22 distant millimeter-selected galaxies. Both studies showed that the basic approach is sound and that uncertainties integrate down as  $\sqrt{N}$ .

While the dust-obscured luminosity and line fluxes of the  $H\alpha$ -emitting galaxies are not known, an estimate of the GEP-S spectral stacking potential can be made by linking the  $H\alpha$ -derived star-formation to the expected mid- and far-IR line emission. First, the  $H\alpha$  fluxes must be corrected for extinction. [Merson et al. 2018] combine the *Galacticus* output with *Cloudy* models, suggesting that the typical extinction correction at  $H\alpha$  for these systems will be 1.9. Then the extinction-corrected  $H\alpha$  fluxes can be converted to star-formation rates, and thus IR luminosities, using the [Kennicutt Jr 1998] relations, tabulated in the 6th and 7th columns of Table 5.

The final column in the table lists estimates of the number of independent stacks that could be generated from the GEP-S data cube. These were obtained by comparing the far-IR spectral line depth ( $5\sigma$ ) obtained in the 3000-hour GEP-S wide spectral survey (GEP-WSS) covering a subset of the near-IR survey area (100 square degrees was adopted), with the line flux expected from the median near-IR selected galaxy. Detection of features with a line luminosity to total IR luminosity ratio of  $2 \times 10^{-4}$  was required, ensuring that the stack will be sufficiently sensitive to detect the key fine-structure transitions, including [Ne V]. This comparison yields the number of galaxies that would be required to measure an aggregate spectrum; it is typically in the few hundred. The 100 square degree dataset should thus yield on order 1000 independent spectral stacks, each a Rosetta stone for

**Table 5.** GEP-S Stacking of IR Galaxy Datasets.

Survey	Redshift of $H\alpha$	Area	Flux Depth	Density	Median SFR	$L_{\text{IR}}$	$N_{\text{Total}}$	# Stacks
		sq deg	erg/s/cm <sup>2</sup>	/sq deg	$M_{\odot}/\text{yr}$	$L_{\odot}$		
Euclid	0.9–1.8	15,000	$2.4 \times 10^{-16}$	4,000	33	$1.9 \times 10^{11}$	60 million	260
WFIRST	1–2	2,200	$1.0 \times 10^{-16}$	10,000	15	$6.8 \times 10^{10}$	22 million	950

understanding the aggregate activity in that galaxy population.

The stacks will be naturally organized hierarchically, with more galaxies in stacks for the lower luminosity, higher-redshift bins and fewer for the brighter galaxies. They will cover ranges such as 12 to 97  $\mu\text{m}$  (for  $z = 1$ ) to 8 to 64  $\mu\text{m}$  (for  $z = 2$ ). Throughout, the stacks will contain:

- The sequence of five neon fine-structure transitions ranging from [Ne II] to [Ne V] (ranging from 12.3 to 36  $\mu\text{m}$ ). This sequence probes the ionization state of the gas, and thereby provides constraints on the stellar mass function and (in the case of [Ne V]) provides the rate of SMBH accretion (§ 2.3.3).
- [Si II] and [O I], which probe neutral gas mass and density (§2.3.5).
- Far-IR [O III] and [N III] fine-structure transitions which can be used to probe metallicity per §2.3.6.
- The low-lying rotational H<sub>2</sub> transitions that probe cool/warm (few-hundred-Kelvin) molecular gas, including shocked material resulting from galaxy collisions and stellar winds.
- Absorption features of OH that reveal the column density of molecular gas around active star-forming regions.

#### 2.5.4 Line Intensity Mapping with GEP-S Surveys

A powerful emerging technique in long-wavelength astronomy is line intensity mapping (LIM). Introduced over 20 years ago, initially for studies of 21 cm radiation [Madau et al. 1997; Shaver et al. 1999], it was subsequently suggested for the far-IR fine-structure lines [Suginohara et al. 1999]. In LIM, the clustering of line-emitting galaxies is detected as fluctuations in a 3-D spatial-spectral dataset in which the line-of-sight dimension is encoded as wavelength. A principal feature of LIM is that it is sensitive to all sources of emission, not just the individually detected galaxies. It is thus vital if much of the luminosity function is below the detection threshold. Another key feature of LIM is the ability to measure cross-correlations among multiple datasets, for example comparing far-IR fine-structure transitions with one another and with HI 21 cm. Prospects for LIM in the far-IR/submillimeter has been examined in several studies [Gong et al.

2011; Uzgil et al. 2014; Silva et al. 2015; Cheng et al. 2016; Lidz and Taylor 2016; Serra et al. 2016]. Ground-based experiments are underway, making first measurements of CO [Cleary et al. 2016; Bower et al. 2015], and [CII] in the 1-mm atmospheric window [Crites et al. 2014; Lagache 2017], and a balloon experiment is now funded to target [CII] in the 240 to 420  $\mu\text{m}$  band (STARFIRE)—see [Hailey-Dunsheath et al. 2018].

GEP-S is extremely well suited to LIM because it offers excellent surface brightness sensitivity. Point-source sensitivity (which typically requires large apertures) is not required. Sensitivity estimates for a cryogenic far-IR mission have been presented in [Uzgil et al. 2014]. Scaling from these results indicates that GEP-S survey fields designed for the galaxy surveys should readily detect the clustering signal that encodes the total co-moving luminosity density ( $\rho_{\text{line}}$ ) in the bright lines (particularly [O III] 88  $\mu\text{m}$ ) at  $z = 1.5$  (the epoch considered in Uzgil + 14) with SNR of several hundred. For this measurement, the 100-square degree dataset will be the most powerful because it will have the lowest sample variance; we expect the bright lines will be sample variance limited with a clustering SNR of more than 50. The 1.5-square-degree dataset will be used to measure or set limits on the line emission at higher redshifts. The SNR in the power spectrum,  $P(k)$ , scales as  $P_{\delta\delta}(b\rho_{\text{line}}/D_L)^2$ , where  $P_{\delta\delta}$  is the underlying dark matter clustering power,  $b$  is the luminosity weighted bias, and  $D_L$  is the luminosity distance. Even with  $\rho_{\text{line}}$  fixed, this product drops off rapidly with look-back time; however, GEP-S should detect the clustering in the shorter-wavelength fine-structure (e.g., [Si II] 34, [O I] 63  $\mu\text{m}$ ) lines out to  $z = 4$  with SNR of several. Detectability at higher redshifts will depend on the luminosity density at that redshift, and will be a subject for detailed study in Phase A.

This experiment will be conducted with the datasets obtained as part of the other surveys, but it does demand high fidelity in the maps over large scales ( $\sim 1$  degree), where the clustering signal resides. This translates to requiring good detector stability (1/f knee of at most 100 mHz) so that sensitivity is preserved as the scan crosses the field.

#### 2.5.5 Estimation of Extragalactic Confusion Noise

Extragalactic source confusion arises when point spread functions of galaxies overlap. It happens at

far-IR wavelengths where diffraction-limited beams can be 10" or larger. It can be difficult or impossible to separate galaxy properties when they are 'confused', although there are well-developed methods to make use of prior information to deconvolve measurements. Confusion 'noise' is the signal that arises from galaxy separations on the order of the beam size. It forms a noise floor below which an observation cannot integrate; however, fruitful quantitative analysis can be done well into the confusion noise floor. In this subsection, estimates of the expected GEP-I confusion noise are presented. In the next subsection, a method to mitigate confusion is presented. In summary, GEP-I observations likely will reach the confusion noise level at approximately 70  $\mu\text{m}$  and longward in the deepest two surveys (3 and 30 sq deg). GEP-S spectral line observations will not be subject to confusion because lines from multiple redshifts will be distinguishable with  $R = 200$ .

We estimate the extragalactic confusion noise to be expected for GEP-I observations by: 1) considering confusion noise measurements from the previous observatories, and 2) deriving an empirical relationship for confusion noise as a function of telescope aperture diameter to interpolate to GEP-I's bands. The confusion flux density was estimated using *Spitzer* 70 and 160  $\mu\text{m}$  [MIPS 2011; Frayer et al. 2009] and *Herschel* 70, 100, and 250  $\mu\text{m}$  [Magnelli et al. 2013; Berta et al. 2011; Herschel Team 2014]. When the various confusion noise measurements are scaled by our empirically derived relationship between confusion and aperture diameter (confusion noise flux density  $\sim D^{-2}$ ; Figure 15), they are consistent. This validates the scaling relation for interpolation to the GEP 2.0 m aperture for estimation of confusion noise. It also shows that aperture diameters below 2.0 m will be increasingly susceptible to confusion.

We assess confusion noise for GEP-I by comparison to estimated map depths (Figure 11) for the four GEP-I surveys. The comparison yields the following results:

1. At 24  $\mu\text{m}$ , GEP-I will not be confusion limited: *Spitzer* was not with a 0.85 m, 4 K aperture even in deep observations.
2. The 70  $\mu\text{m}$ , 1 $\sigma$  RMS GEP-I map depths are 6  $\mu\text{Jy}$ , 20  $\mu\text{Jy}$ , 60  $\mu\text{Jy}$ , and 6 mJy for the 3, 30, 300 square degree, and all-sky surveys, respectively. Scaling the *Spitzer* 300  $\mu\text{Jy}$ ,

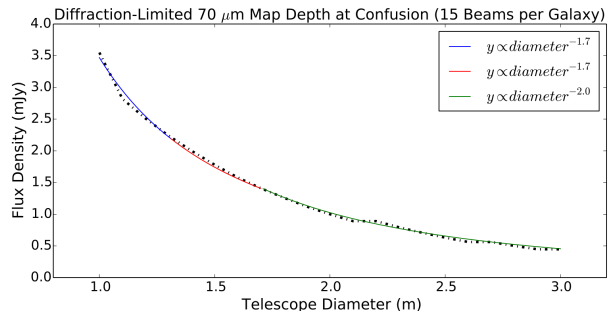


**Figure 15.** GEP's 2.0 m aperture is optimal: a smaller aperture would suffer much worse confusion noise and a larger aperture would not be feasible with a Probe-class budget. The plot shows the flux density at which a classical confusion of 15 beams per galaxy as a function of telescope aperture diameter for a wavelength of 70  $\mu\text{m}$ . The number counts are from [Béthermin et al. 2012]. The curves are piecewise fits, which can be represented approximately as confusion noise flux density proportional to  $D^{-2}$ , where  $D$  is the aperture diameter.

70  $\mu\text{m}$  confusion noise by the empirical  $D^{-2}$  relation yields 50  $\mu\text{Jy}$  RMS. Thus, the noise in the deepest two surveys will be dominated by confusion noise at 70  $\mu\text{m}$ , the observational noise will just reach the confusion noise in the 300 square degree survey, and the all-sky survey will not be affected by confusion noise.

3. At 100  $\mu\text{m}$ , scaling by the  $D^{-2}$  relation, *Herschel*'s observed confusion noise of 200  $\mu\text{Jy}$  RMS would be 600  $\mu\text{Jy}$  for GEP-I. Thus, the all-sky survey, with a 1 $\sigma$  map depth of 600  $\mu\text{Jy}$ , would just reach the confusion noise level.
4. All four surveys will likely reach the confusion noise level at wavelengths longer than 100  $\mu\text{m}$ . *However, observations must be made at these wavelengths to measure total luminosities of bright, low- $z$  galaxies and lensed high- $z$  galaxies, of which GEP-I will detect many (Figure 12).*

This analysis supports our conclusion that GEP-I will likely have significant confusion noise at 70  $\mu\text{m}$  and longer, but not at shorter wavelengths. GEP-I must integrate deeper than the 70  $\mu\text{m}$  confusion noise in the two deepest surveys for PAH redshifts of luminosity  $z \leq \sim 4$  galaxies with the wavebands at

50  $\mu\text{m}$  and below, which will not be limited by confusion noise. Additionally, monochromatic fluctuation ‘probability of deflection’ P(D) analyses—for example, [Glenn et al. 2010] – show that it is possible to constrain galaxy populations meaningfully with observations deeper than the confusion noise level. A polychromatic P(D) analysis with GEP-I observations covering the redshifted PAH features would be extremely powerful: it would yield precise galaxy number counts and redshifts statistically for the ensemble, and therefore luminosity functions, and tightly constrain galaxy evolution models.

Furthermore, using cross-identification with counterparts at shorter wavelengths, galaxy properties can be measured even when there is source confusion (§2.5.7). For example, [Labbé et al. 2015] showed that contamination by confusion can be reduced a factor of six with short-wavelength prior-based photometry. Additionally, because the detector count in wavebands longer than 100  $\mu\text{m}$  (GEP-I band 19) is small (§3.2 and §3.4), the cost of retaining them is clearly merited for measurements of far-IR luminosities, nearby galaxy science, and powerful P(D)-type fluctuation analyses.

### 2.5.7 Method to Mitigate Confusion: Bayesian Forced Photometry Using *XID+*

GEP-I imaging likely will be susceptible to confusion noise from around 70  $\mu\text{m}$  onward, corresponding to GEP-I bands 17 to 23. In this section we investigate the current state of the art for dealing with confusion and future developments that will improve accuracy further.

The Next Generation (X)Cross Identification (*XID+*) code was developed to estimate flux densities accurately from confusion-limited *Herschel* imaging [Hurley et al. 2016]. A key feature of *XID+* is that it exploits the prior information on the positions of galaxies obtained from high-resolution imaging at shorter wavelengths. With confused data the flux density estimates are inevitably correlated; thus, a second key feature of *XID+* is that it investigates the full posterior space of flux densities to derive rigorous uncertainties, taking into account confusion. The experience with the *Herschel* Extragalactic Legacy Project (HELP), [Hurley et al. 2016], shows that good priors are crucial to extract flux densities accurately. For *Herschel*, the most effective data for simple prior source positions were from *Spitzer*/IRAC images, which provided high spatial resolution and were well correlated with far-IR flux densities. Long-wavelength observations with GEP-I will benefit

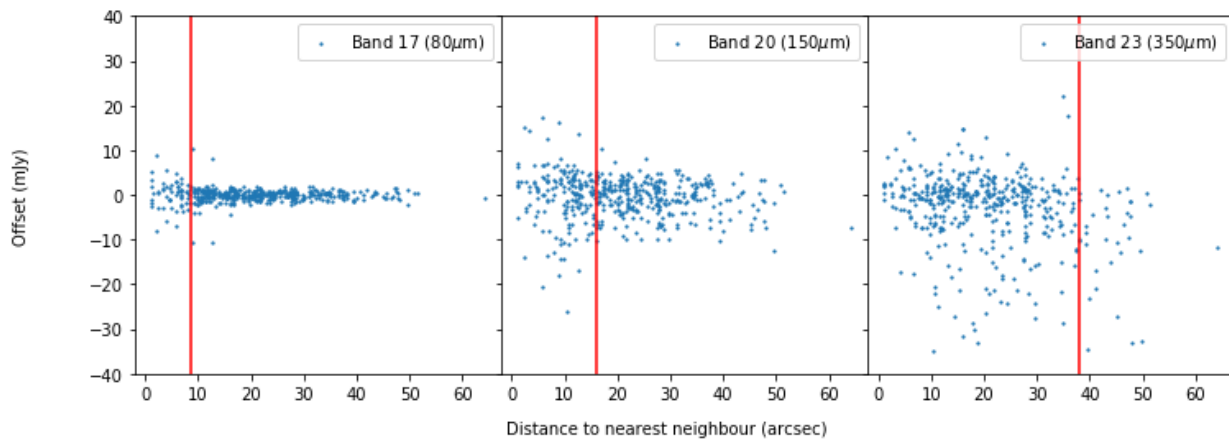


**Figure 16.** Difference between *XID+* fitted and true galaxy flux densities as a function of distance to the nearest galaxy neighbor for three GEP-I long-wavelength bands: 17, 20, and 23 (with FWHM beam sizes of 8.6, 16, and 38 arcseconds, respectively). For bands 17 and 20, the fractional error in the flux density is small down to the beam size and clustered around zero. Red vertical lines show the beam width as measured by the full width at half maximum. At the beam size and below the dispersion increases, although there is no bias. For band 23, GEP-I’s longest-wavelength band, the simulation data do not extend to great enough separations to see that the difference changes at the beam size. In this band, there is a negative bias for some galaxies—this will have to be addressed in the *XID+* algorithm or quantified for statistical corrections.

similarly from the short wavelengths, and we use these as priors in our modeling of confusion. The performance of XID+ also can be quantified by measuring the difference between fitted and true galaxy flux densities as a function of the distance to the nearest galaxy neighbor. Figure 16 shows that down to galaxy separations of the beam size—below the classical confusion ‘limit’—galaxy flux densities can be deblended with small fractional errors and little or no bias in most cases.

A recent extension of XID+ has been the inclusion of spectral energy distribution models to fit multiple bands simultaneously. This has the capacity to break degeneracies and significantly reduce errors. Applying this method to all 23 GEP-I bands is highly promising as a means to deblend the confused bands. Utilizing the XID+ flux densities from the standard wide-field single bands as priors, this method can be used for highly blended galaxies or galaxies of particular scientific interest. Work is underway to apply it to large samples.

### 3 INSTRUMENT PAYLOAD

The GEP payload includes the optical telescope assembly (OTA), GEP instrument comprised of one imager module (GEP-I) and four spectrometer modules (GEP-S), and a payload thermal subsystem [Glenn et al. 2018]. Figure 17 shows the basic optical configuration of GEP and layout of all major components in the payload assembly. This section

includes: descriptions of the optical telescope assembly (§3.1), the GEP imager (GEP-I, §3.2), the GEP spectrometer (GEP-S, §3.3), the kinetic inductance detectors (KIDs) that comprise all GEP focal planes (§3.4), their readout electronics (§3.5), and the payload thermal design (§3.6).

#### 3.1 Optical Telescope Assembly

To meet the science objectives, the fundamental optical design requirement is to collect light with the 2 m diameter primary mirror and to form an  $f/9$  focus at five interface planes. The unobscured three-mirror astigmat (TMA) is an oft-used configuration that is well suited to the first-order optical and mechanical requirements of this system. The powered mirrors are all conic shapes with parent surfaces that have mutual tilts and decentrations to reduce wavefront error (Figure 17).

The five instrument interface planes are nearly coplanar at the common focal surface of the TMA, with minor differences in final focus to minimize wavefront error in each channel. Based on the sizes of the Focal-Plane Array (FPA), spectrometer slits and enclosures, the optimized field of view is  $0.81^\circ \times 0.88^\circ$ . The centers of the spectrometer slits are in the plane of symmetry of the TMA so that they can be untilted with respect to the central ray to each spectrometer. Stray light suppression is achieved with a pupil stop and a field stop.

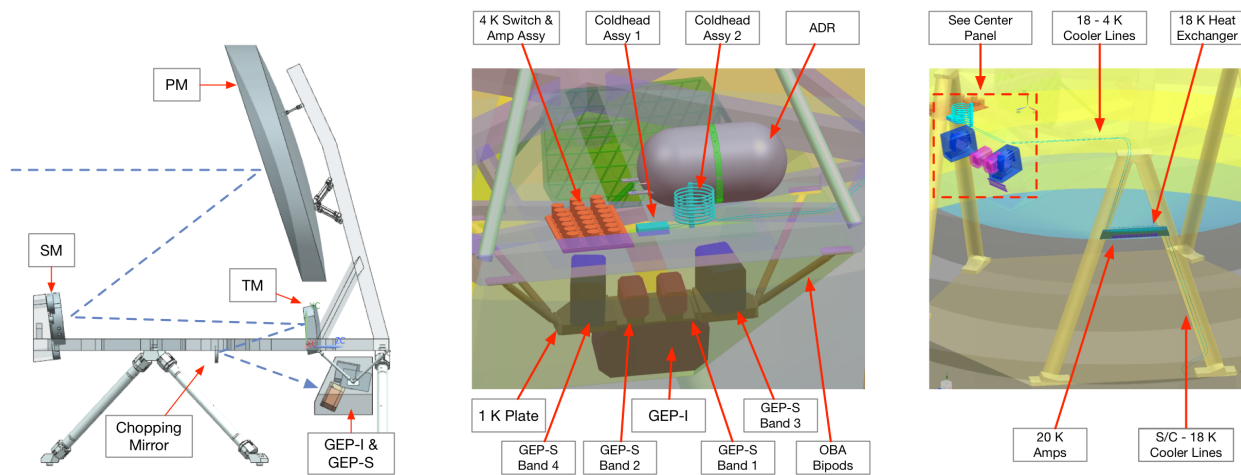


**Figure 17.** *Left:* GEP optical configuration side view shows its simple TMA design. A field stop is located between the secondary and tertiary mirrors and the fourth optic is a chopping mirror located at an image of the primary mirror, forming a pupil stop. The GEP-I and GEP-S modules are in the lower right. *Center:* Detail of GEP-I and the four GEP-S focal planes along with the ADR and 4 K cryogenic assembly. *Right:* Detail of the 18 K assembly located near the focal plane assembly.

To meet the extragalactic confusion requirement, the primary mirror will be required to be diffraction limited at  $24\ \mu\text{m}$ . This also serves to control cost because of the lower limit of KID pixel sizes for a given readout bandwidth (§3.4 and §3.5). However, the RMS wavefront error across the field of view in the optical design is diffraction limited at the minimum wavelength of  $10\ \mu\text{m}$ . The 100% encircled energy diameter is  $\leq 1.45''$ , much less than the  $3.43''$  detector pixel size.

The baseline for the GEP primary, secondary, and tertiary, and chopping mirrors is unactuated silicon carbide (SiC), as was flown on *Herschel* and *Gaia*. U.S. vendors are currently able to develop, manufacture, and test a sintered 2 m primary mirror from SiC. However, a technology that shows promise for GEP and other far-IR telescopes is SiC mirrors with distributed figure control actuators (§6).

### 3.2 GEP Imager (GEP-I)

The GEP-I concept is designed to obtain repeated measurements of each galaxy that is observed in each of the 23 wavebands by continuously scanning areas of sky. Each of the wavebands occupies the same amount of focal plane area, 0.002 square degrees, half of which is occupied by detectors and half of which is allotted for filter mounting. As shown in Figure 18, the shortest wavebands are in the center, where the optical performance is the best, and the longest wavebands are at the two edges. Metal-mesh bandpass filters are placed over each array. Bands 1–18 have spectral resolution  $R = 8$ , whereas bands 19–23 are  $R = 3.5$ .

GEP-I will have 25,735 KIDs (§3.4). GEP-I’s optical performance is diffraction limited at  $10\ \mu\text{m}$ . However, the primary mirror is specified to be diffraction limited at  $24\ \mu\text{m}$ , corresponding to  $\sim 3''$  beam size (FWHM). The primary reason for this is that the smallest KID pixel size we expect to be able to fabricate without exceeding the readout bandwidth is  $300\ \mu\text{m}$ , which corresponds to  $3.43''$ . Thus, bands 1–13 will not be Nyquist sampled while bands 14–23 will be. Should greater bandwidth become feasible through improvements in data acquisition and computing speed (a very likely development), the pixel sizes can be reduced, recovering Nyquist sampling at shorter wavelengths.

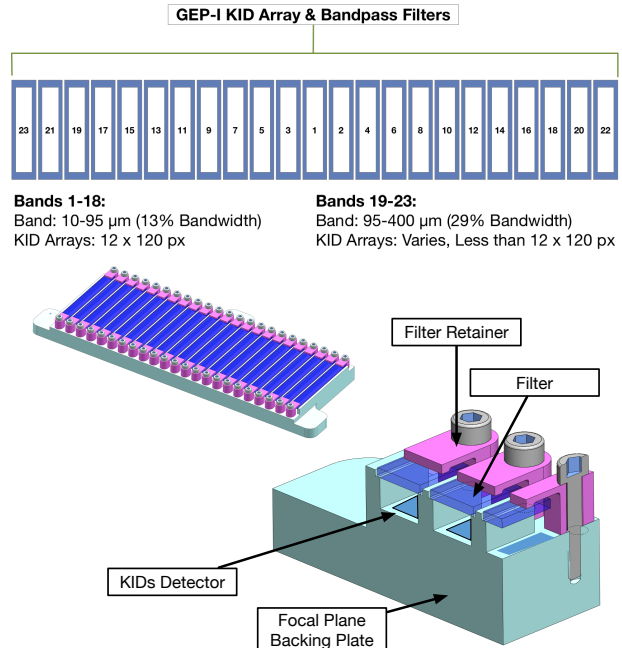


**Figure 18.** *Top:* Imager (GEP-I) focal plane layout concept. The 50% active area allows for bandpass filter mounts. Bands 1 ( $10.0\text{--}11.3\ \mu\text{m}$ ) through 15 ( $57.7\text{--}65.4\ \mu\text{m}$ ) have 1,440 KIDs (arrays of 12 horizontally in the top diagram by 120 vertically), with  $3.43''$  pixels ( $300\ \mu\text{m}$  square). The longer-wavelength bands have fewer, larger KIDs such that the focal plane area occupied by each photometric band is approximately the same. For example, Band 23 ( $300\text{--}400\ \mu\text{m}$ ) has 46 KIDs  $1,560\ \mu\text{m}$  square. *Bottom:* Cross-section of GEP-I shows the simple mounting structure for the KID arrays and the bandpass filters.

### 3.3 GEP Spectrometer (GEP-S)

GEP’s spectrometer was designed to meet the science requirements calling for observing mid- and far-IR atomic fine-structure lines from galaxies over a range of redshifts. Specifically, the  $24.3\ \mu\text{m}$  [Ne V] line starting at  $z = 0$  (for AGN identification) and the  $63.2\ \mu\text{m}$  [O I] line at  $z = 2$ . The entire bandwidth should be available to identify spectral lines for galaxies of unknown redshift. Sufficient spectral resolution is required to achieve good sensitivity (through dispersion of the astrophysical background photons). Spectral resolution  $R = 200$  meets these requirements.

GEP-S is comprised of 24,640 KID detectors (see §3.4) and is implemented with four spectrometers, identified as bands 1–4 (Table 6). The ray trace diagram and CAD model of band 4 is

**Table 6.** The four bands of GEP-S perform spectral mapping at  $R = 200$ .

	Bandpass ( $\mu\text{m}$ )	KID Pixels	Slit length ( $^\circ$ )
Band 1	24–42	7840	3.8
Band 2	40–70	7840	6.4
Band 3	66–116	4480	6.0
Band 4	110–193	4480	10.0

shown in Figure 19. Each band, or spectrometer module, is comprised of an enclosure, a slit, a collimator, a diffraction grating (operated in first order), a focusing mirror, and an array of KIDs. The long slit lengths enable spectral mapping. As with the imager, the shortest-wavelength bands 1 and 2 are placed nearest to the center of the field of view where the optical performance is the best.

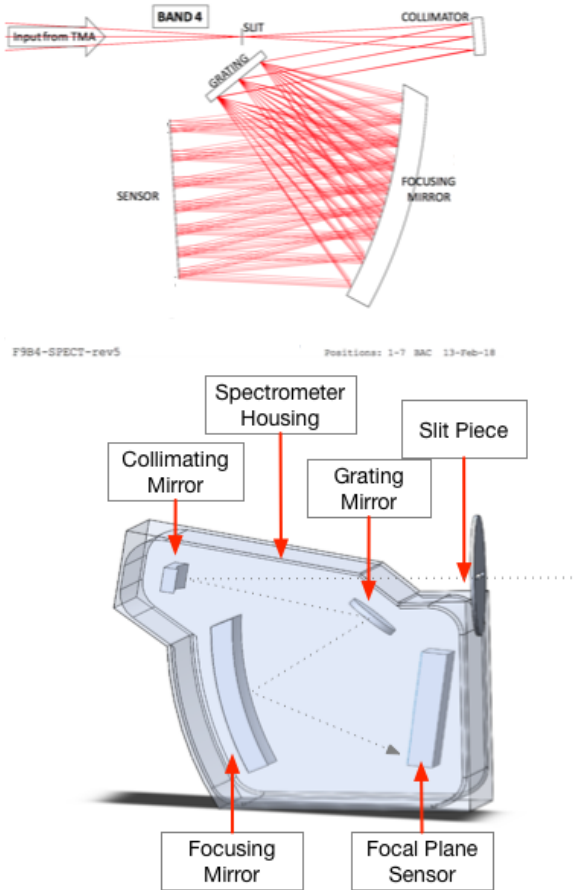


**Figure 19.** GEP-S’s band 4 was designed to observe from 110 to 193  $\mu\text{m}$ . Top: A ray-trace analysis verified optical performance. Bottom: Mechanical design. GEP-S’s placement within the payload assembly is shown in Figure 17.

### 3.4 Kinetic Inductance Detectors

New, deep mid- and far-IR observations require large arrays of sensitive detectors. Over the past two decades, the superconducting KID has emerged as a powerful array technology applicable to a very broad wavelength range that includes the 10-400  $\mu\text{m}$  band needed for GEP [Day et al. 2003; Zmuidzinas 2012; Mauskopf 2018; Farrah et al. 2017]. KIDs are baselined for GEP-I and GEP-S and will be a competitive technology for the Origins Space Telescope (OST) [Battersby et al. 2018], a 2030s Flagship mission concept that also requires large arrays of mid- and far-IR detectors. Figure 20 illustrates the landscape of far-IR detectors in terms of sensitivity (expressed as noise equivalent power, or NEP) and numbers of pixels in focal plane arrays.

Back-illuminated, lumped-element, microlens-coupled aluminum KIDs (Figure 21) operating at 100 mK will meet the requirements on GEP-I and GEP-S. Each KID pixel is a superconducting thin-film microresonator, consisting of an absorbing meander inductor and an interdigitated capacitor deposited on a silicon substrate. Light incident on a KID pixel is concentrated onto the inductor by the microlens. The geometry of the inductor controls the absorption characteristics as a function of wavelength and polarization. Absorption of photons changes the inductance, producing a small shift in the resonant frequency ( $\Delta f$ ). The interdigitated capacitors are unique for each pixel, allowing different resonant frequencies and therefore frequency-multiplexed readout. KIDs with sensitivity sufficient for GEP-I have been demonstrated [Baselmans et al. 2017] while modest improvement is needed for GEP-S.

Our report baselines KIDs for GEP-I and GEP-S because, at present, this technology offers the most straightforward path to meeting the science requirements; a 2023 GEP Pre-Phase A trade study would provide an opportunity to confirm the detector technology that is most mature and easiest to integrate with the spacecraft. Current alternatives include Si:As IBCs as used in JWST’s MIRI, and superconducting transition-edge sensor (TES) bolometers. Si:As IBCs are technologically mature and were considered in detail for GEP, but are unusable beyond 28  $\mu\text{m}$  and so KIDs would still be needed for longer wavelengths. However, the pixel pitch and operating temperature requirements for IBCs (7 K) and KIDs (100 mK) are very different,

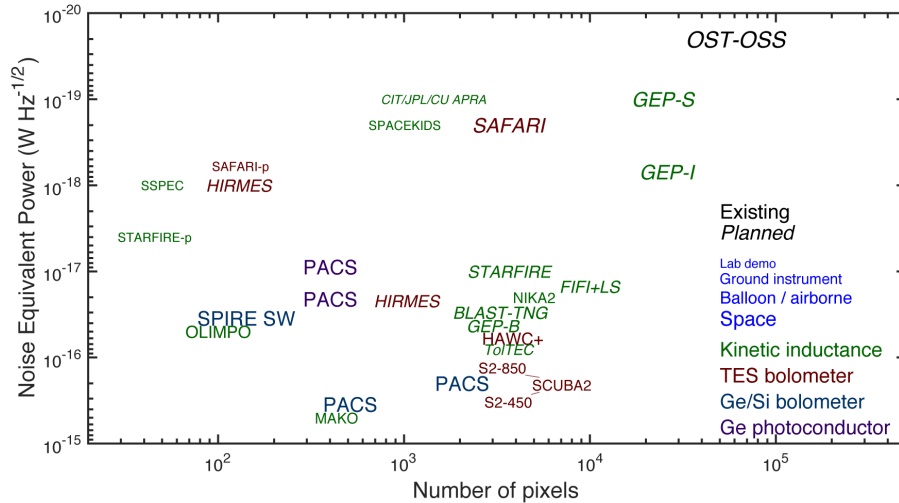


**Figure 20.** Far-IR detector technology has made considerable progress toward larger, more sensitive arrays over the past decade. BLAST-TNG: [Lourie et al. 2018]; CIT/JPL/CU APRA: [Hailey-Dunsheath 2018]; FIFI+LS: [Looney 2018]; GEP-I and GEP-S: this report; HIRMES: [Nikola et al. 2018]; MAKO: [Swenson et al. 2012; McKenney et al. 2012]; NIKA2: [Adam et al. 2018]; OLIMPO: [Paiella et al. 2018]; OST-OSS: [Bradford et al. 2018]; PACS: [Poglitsch et al. 2010]; SAFARI-p: [Hijmering et al. 2016]; SAFARI: [de Lange et al. 2018]; SCUBA2: [Holland et al. 2013]; SPACEKIDS: [Baselmans et al. 2017]; SPIRE: [Griffin et al. 2010]; SSPEC: [Wheeler et al. 2018]; STARFIRE-p: [Barlis et al. 2018; Hailey-Dunsheath et al. 2018]; STARFIRE: [Aguirre and Collaboration 2018]; and TolTEC: [Wilson et al. 2018].

and the diverging optical and cryogenic designs would effectively necessitate two instruments *each* for GEP-I and GEP-S and therefore drive GEP above the cost cap. Furthermore, Si:As IBC array fabrication is currently in hiatus and would need to be restarted for GEP, with clear implications for cost and risk. Meanwhile, TES bolometers can span the required wavelength range and could potentially achieve the required sensitivity, but have not

reached comparable multiplexing density and require complex hybridization with SQUID readouts, with attendant risks to performance and cost. Further technical details of KIDs and a plan to develop and demonstrate this technology to the level needed for GEP is described in §6.1.

All elements of the GEP KID focal planes are passive. The active components of the detector

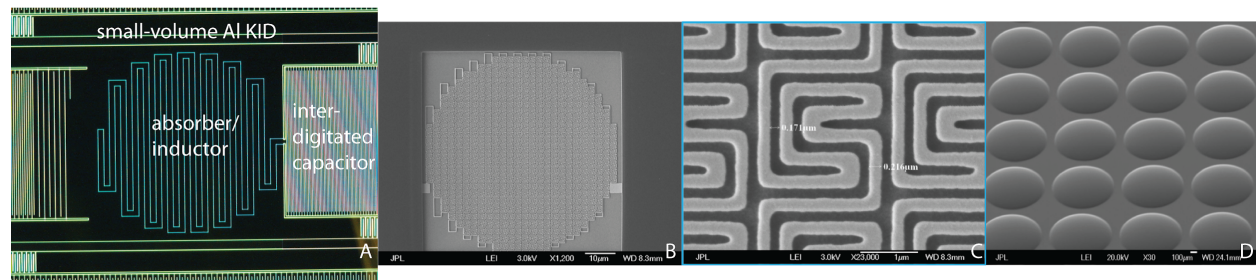


**Figure 21.** KID designs suitable for the GEP-I and GEP-S wavebands. (A) This  $\lambda > 100 \mu\text{m}$  design [Swenson et al. 2012; McKenney et al. 2012; Stacey et al. 2014] uses a meandered inductor that acts as an efficient single-polarization absorber. A microlens focuses the far-IR radiation onto the absorber. Dual-polarization designs have also been demonstrated. An interdigitated capacitor (partially shown) completes the resonant circuit and sets the radio-frequency (RF) readout frequency. (B) This modified absorber/inductor design provides high absorption efficiency at  $\lambda = 10 \mu\text{m}$ , and is shown in close-up in (C). (D) Illustrates prototype silicon microlenses produced at JPL/MDL [Lee et al. 2013]; adopting hexagonal close packing increases the optical fill factor to 91%. Over 5,000 such microlenses have been produced on a 100 mm diameter silicon wafer.

readout chain are low-noise amplifiers at 4 K and 18 K and warm readout electronics.

### 3.5 Detector Readout Electronics

The GEP-I and GEP-S modules will share the same set of readout electronics: they have separate (non-simultaneous) observing modes. Their use of the same electronics is diagrammed in Figure 22. Microwave switches on the readout lines will enable selection of GEP-S or GEP-I for readout. There are 24 parallel readout channels available from three RF readout boards with eight channels each. Of the 24 channels, 23 are utilized corresponding to the number of GEP-I wavebands and detector modules. The four GEP-S spectrometers will have their readouts distributed over these 23 modules. The eight-channel RF readout cards share a payload electronics chassis with a chopping mirror driver card and two clock, processor, memory, and power cards for dual-string redundancy. The total estimated power consumption for the readout electronics is 484 W CBE.

For all GEP focal planes, KIDs are organized into groups of ~1,500 detectors that are spread

across a 0.6-1.6 GHz band and read out using electronics as illustrated in Figure 22. The choice of a 1.1 GHz center frequency resulted from a trade study in which smaller pixels were favored by the optical design but larger pixels reduced the readout frequency and bandwidth, and thus power dissipation. The readout electronics generates an analog waveform using RF-DACs that is transmitted to the cold focal plane, exciting all 1,500 resonators. The 1 GHz bandwidth return signal from all 1,500 KIDs is digitized with RF-ADCs and digitally channelized with sufficient resolution to separate the individual KID frequencies. Resulting digitized data are low-pass filtered, recorded, and ultimately downlinked to Earth. This basic processing scheme, initially demonstrated in 2006 [Mazin et al. 2006], has now been implemented in various forms for ground-based and balloon-borne instruments [Yates et al. 2009; Duan et al. 2010; Duan 2015; McHugh et al. 2012; Swenson et al. 2012; Strader 2016; Bourrion et al. 2016; van Rantwijk et al. 2016; Gordon et al. 2016; Henderson et al. 2018]. GEP will process data on-board, including cosmic ray

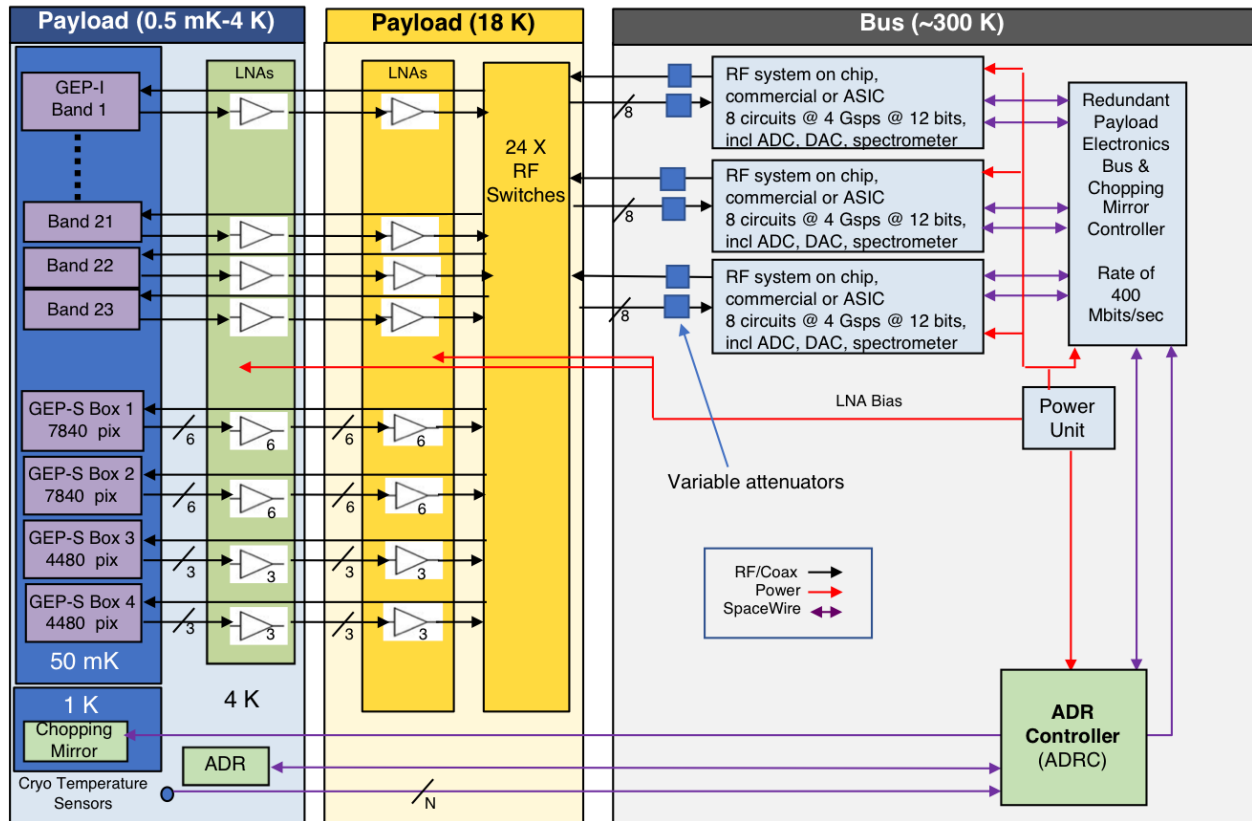


**Figure 22.** Readout system for the GEP KID arrays. All electronics are room temperature except the amplifiers at 4 K and 18 K (and the KIDs themselves at 0.1 K). The power consumption is conservatively estimated at 25 W per readout circuit. GEP-I uses 23 readout channels, GEP-S Box 1 & 2 use six readout channels each, and GEP-S Box 3 & 4 use three readout channels each.

removal, basis change from in-phase/quadrature to frequency-shift space, and merge IMU attitude data with each science data frame.

In §6.2, the remaining aspects of readout electronics technology development are described and a plan with milestones leading to TRL 6 by 2025 is defined. Industry trends indicate that a solution with commercial off-the-shelf (COTS) components may be available as FPGA development works to meet the needs of other customers of GHz microwave electronics. Should a COTS option not be available by 2023, a dedicated ASIC will be developed, which JPL has already done for GHz-bandwidth spectrometers. Our GEP study adopts a conservative power consumption of 24.4 W per 1 GHz readout channel, within reach of current commercial technology.

### 3.6 Payload Thermal

The thermal system for GEP employs multiple passive and active stages to meet the temperature intercept requirements of the instruments and optical assembly. Figure 23 from Moore et al. 2018 shows all active and passive components in a block

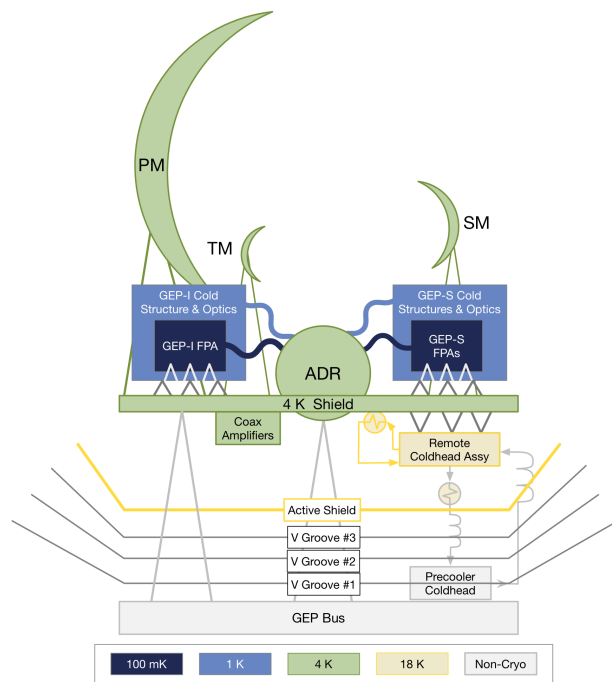


**Figure 23.** GEPs thermal accommodation uses active and passive cooling to maintain 100 mK required by the focal planes, 4 – 6 K for the optical assembly, and 18 K for the cryogenic amplifiers. Figure from [Moore et al. 2018]. Physical layout of major active components is shown in Figure 17.

diagram. The chopping mirror (see Figure 17) operates at 4 K. A continuous multi-stage adiabatic demagnetization refrigerator (ADR) provides cooling for the detectors at 100 mK, with a 1 K thermal intercept to reduce thermal noise and parasitic loads. As discussed in the §5.3, NASA GSFC has extensive experience producing flight ADRs and the proposed system utilizes high heritage subcomponents from previous missions.

A hybrid Joule-Thomson/Stirling cryocooler intercepts heat at 4 K, from the ADR, cryogenic amplifiers, and parasitic loads. The hybrid cooler has an 18 K intercept to cool a second stage of amplifiers for the detector signal and an active shield. As discussed in §5.3, multiple vendors, including NASA GSFC and Ball Aerospace, offer high TRL cryocoolers capable of meeting GEP heat-lift requirements. The sunshield assembly consists of three reflective shields with a total area of 33 m<sup>2</sup>, and a 9.77 m<sup>2</sup> active shield located above the sunshield under the focal plane boxes. The substrate of all four shields is an internally self-supporting 1 mm thick M55J laminate with an areal density of 29.5 kg/m<sup>2</sup>. The reflective coating on the three warmer, passively cooled sunshields consists of a thin (.005”) layer of aluminized Kapton adhered to the surface. The bottom surface of the actively cooled sunshield is also aluminized Kapton, however the top surface is a 1 mm thick high purity Aluminum thermal spreader layer. Fiberglass composite struts provide intershield supports at the perimeter to accept launch loads.

The sunshields are passively cooled. They intercept conducted loads from the bipods and harnesses and radiative loads from the Sun. With these non-deployable sunshields, the spacecraft can tilt  $\pm 20.6^\circ$ , maintaining all cryogenic components in the shadow cone and thus preserve thermal system operability. The cooler and ADR electronics dissipate heat at ‘room’ temperature ( $\sim 300$  K), along with all bus components, which is radiated by 10.5 m<sup>2</sup> of radiators mounted on the bus behind the solar panels.

## 4 DESIGN REFERENCE MISSION

The GEP flight system is designed as a Class B mission with significant science and engineering margins. It utilizes a combination of high-heritage designs and new components from trusted vendors, resulting in a low-risk mission below the Probe class cost cap. The GEP flight system is based on the Ball

Aerospace BCP2000 reference bus, of *Kepler* heritage, that is customized to meet the science and mission requirements of GEP. Following a one-month transit to an L2 halo orbit, a four-year survey program is divided into an imaging campaign and a spectroscopy campaign, where over 350 TB of observational data will be downlinked. Table 7 summarizes high-level GEP mission parameters while Table 8 outlines the system-level mass equipment list (MEL).

**Table 7.** GEP mission parameters.

Parameter	GEP's Design
Launch Date	January 1, 2029
Destination	Sun-Earth L2
Mission Duration	4 years
Bus Design Life	5 years
Mission Class	B, dual string (hot/cold redundancy)
Anticipated Bus Heritage	Ball BCP2000 (e.g., Kepler)
Dry Mass (CBE + Contingency)	1320 kg
Max Power (CBE + Contingency)	1990 W
Stabilization	Three axis (0.5 as/3 min), non-spinning
Primary Mirror Temperature	4 K design, 6 K allowable
Focal Plane Temperature	100 mK
Field of Regard	$\pm 20.6^\circ$
Total Mission Science Data	>350 TB

**Table 8.** GEP system-level mass equipment list (MEL).

	CBE Mass [kg]	CBE + Contingency [kg]
<b>Payload</b>	<b>376</b>	<b>488</b>
<b>Spacecraft Bus</b>	<b>669</b>	<b>831</b>
ACS	52	58
C&DH	27	29
Power	59	71
Propulsion	55	58
Mechanical	351	457
S/C-Side Adapter	12	16
Cabling	43	56
Telecom	27	31
Thermal	43	55
<b>Total Dry Mass</b>	<b>1045</b>	<b>1319</b>
Propellant Mass		234
L/V-Side Adapter		36
<b>Predicted Wet Mass at Launch</b>	<b>1315</b>	<b>1589</b>
<b>Allowable Wet Mass at Launch</b>		<b>3023</b>

#### 4.1 Mission Design & Phases

The GEP mission is divided into four phases: launch & transit, science checkout, GEP-I science, and GEP-S science. There are no critical events following launch. GEP will conduct its science mission from L2. L2 was selected owing to its available field of regard and favorable thermal environment compared to Earth orbit. Moreover, because GEP has no consumables, there is potential for an extended mission.

The GEP mission is notionally scheduled to launch onboard a Falcon 9 on January 1, 2029 and transit to an Earth-Sun L2 halo orbit. The 30 day transit to L2 will require three trajectory correct maneuvers (TCMs) for a total of 150 m/s required  $\Delta V$ . During transit, GEP will remain warm as a part of the decontamination period described in §5.2.

Following all required TCMs and the decontamination period, GEP will cool down its payload. Once the payload is at its operating temperature, a science checkout phase will evaluate the function of all aspects of the payload. Beginning with science checkout, orbit maintenance will be required for the remainder of the mission, requiring 10 m/s  $\Delta V$  over 16 maneuvers that can be scheduled flexibly.

Following science checkout, the two-year GEP-I science phase will begin. GEP will continuously observe while rotating or rastering about the Sun-Probe axis. GEP-I's survey areas will be defined in advance of launch. For two years, no further modification to this pre-defined survey schedule will be required to meet the science objectives. Moreover, during the GEP-I science phase, GEP-S will not be used. GEP-I will observe at all times, including during downlink, unless otherwise restricted by desaturation events or other health and safety operations. As GEP-I survey data are downlinked, the science team will discover targets (galaxies) for the pointed observations during the GEP-S science phase.

The GEP-S science phase will begin by switching the microwave switches to point to GEP-S. This is the only time they are used following science checkout. During the GEP-S science phase, the plan for observing pre-defined fields and targets defined during the GEP-I science phase is executed. There will be no opportunities for guest-observer programs in Phase E, which limits operations complexity and minimizes science team budget.

## 4.2 Survey Operations

The orthogonal positioning of GEP’s passive sunshield enables GEP’s robust deep scan strategy. With a maximum Sun-Earth-Probe angle of  $15^\circ$ , the field of regard is  $\pm 21.6^\circ$  about its boresight. During the surveys defined in Table 4, GEP rolls about Sun-Probe axis, thereby allowing it to observe the north and south ecliptic pole fields at all times throughout the mission. Owing to the static high gain antenna’s pointing requirement tolerance, surveys will also be conducted during downlink when the boresight rolls about the Earth-Probe axis. Given the location of the halo orbit, the Earth, and the Sun, there is  $6^\circ$  of margin in pointing off the Earth-Probe line (Figure 24).

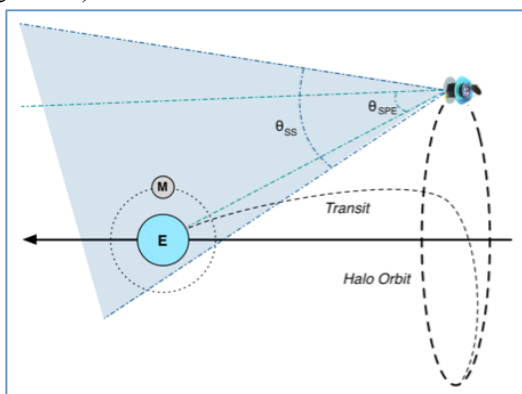


**Figure 24.** The GEP mission design enables GEP to observe with near 100% observational efficiency. The maximum Sun-Probe-Earth angle is  $15^\circ$ . GEP’s sunshields afford a  $42^\circ$  field of regard, illustrated as allowable Sun angle in shaded blue, resulting in a  $6^\circ$  pointing margin about the Probe-Earth line and  $21^\circ$  about the Probe-Sun line. Figure is not to scale.

GEP-S science observations include surveys and targeted observations, only some of which will be at the ecliptic poles. GEP-S fields and targets that are at lower equatorial latitudes will be scheduled in advance so that GEP field-of-regard restrictions can be respected. With this restriction comes the benefit of reduced planning complexity and the resulting potential for Phase E cost growth.

The GEP-I and GEP-S instrument modules observe one at a time and use the same readout electronics. They share a scan survey observing mode, where mapping is performed as the spacecraft slews at approximately  $60''/s$ . The scan survey mode is used for all the GEP-I surveys, for GEP-S’s 1.5 and 100 square degree surveys, and for mapping of nearby galaxies. GEP-S also has a pointed

observation mode in which a chopping mirror, with a total throw of  $\pm 0.2^\circ$ , modulates the signal for  $1/f$  noise mitigation and for background subtraction.

Notably, GEP’s survey operations are resilient to pointing control failure. Reaction Wheel Assemblies (RWA) failure, as recently experienced on *Kepler* and *Dawn*, has the ability to limit observations and reduce mission duration. The first strategy employed by GEP to reduce the impact of RWA failure is by incorporating four reaction wheels, with one being redundant, to meet Class B requirements and to improve survivability.

GEP also is also resilient to pointing faults with safe slewing operations that naturally respect thermal constraints, with sufficient thermal margin to limit noise at maximum nominal off-pointing. In the event of a missed desaturation, RWA total momentum storage is approximately twice the desaturation threshold. The GEP survey strategy requires the spacecraft to slew radially about the Sun-Probe axis or within a  $15^\circ$  offset. With this configuration, solar pressure offers little torque to rotate the spacecraft beyond its maximum off-pointing angle, increasing any associated times-to-criticality.

**Table 9.** GEP has been designed to perform beyond a field of regard set by  $\pm 15$  deg pointing off the Sun-Probe axis. This table shows GEP’s resilience to thermal loads beyond the requirement, at  $\pm 20$  deg.

	Spacecraft Tilt		
	-20 degrees	0 degrees	20 degrees
Total unmarginined load at 4 K (parasitic + instrument)	27.3 mW	26.5 mW	27.8 mW
Total unmarginined load at 18K (parasitic + instrument)	156.8 mW	98.8 mW	128.4 mW
Telescope temperature range (including 4 K structure)	4.5 to 5.3 K	4.5 to 5.3 K	4.5 to 5.6 K
Active shield average temperature	20 K	19 K	19.5 K
Sunshield 3 average temperature	42 K	40 K	47 K
Sunshield 2 average temperature	94.5 K	88 K	92 K
Sunshield 1 average temperature	229 K	223 K	229 K
Bus radiator panel average temperature	271 K	265 K	271.5 K

### 4.3 Propulsion

A simple monopropellant hydrazine blowdown system using heritage components was selected. A single 22 N, Aerojet MR-106L main thruster provides thrust for halo orbit insertion while four 4 N, Aerojet MR-111C thrusters are used to desaturate GEPs reaction wheels once per day. A total of 234 kg of Hydrazine is held to support the total  $\Delta V$  budget of GEP is 160 m/s and daily desaturations.

### 4.4 Attitude Control Subsystem (ACS)

GEP’s ACS subsystem is sized to meet the pointing stability requirement of GEP-S’s pointed-observing mode, requiring 0.5" ( $1\sigma$ ) stability for 300 s and 0.5" pointing knowledge. The pointing knowledge is provided by three low-cost, high-accuracy star trackers (either Sodem Hydra or Ball CT2020), with a fourth carried for redundancy [Ball Aerospace 2018]. Star tracker telemetry is used by the bus for spacecraft pointing and to update a Northrop Grumman SIRU, generating high refresh-rate pointing knowledge piped to payload electronics for recording in observational metadata. Three Adcole 2-axis Sun sensors are flown to provide redundant pointing knowledge during safe mode. Three-axis stabilization for the bus and payload is provided by four high-heritage Honeywell 25 RWA. The RWA momentum capacity is 25 N m s, while the requirement is 10 N m s.

### 4.5 Command & Data Handling

Two high-heritage RAD750 flight computers are flown in a dual-string configuration. Four storage cards are used to provide 760 GB of available storage, three times the daily generated data. This allows data to be sent on the same day of observation, retransmitted on the following day if data are missed, and confirmed for retransmission or deletion on the second day after observation.

GEP produces three types of data products on-board: In-phase/Quadrature IQ0, IQ1, and delta frequency ( $\Delta f$ ), with their processing defined by the flow in Figure 25. All data processing for these products is performed by payload electronics. For GEP-I, IQ0 data represents KID raw data after Fast Fourier Transform (FFT) with pointing and timing information inserted into the metadata. GEP-S IQ0 data products have an additional processing step to demodulate the action of the chopping mirror. The IQ1 data product has a processing step to remove cosmic ray events. Further on-board processing

changes the basis of the data from IQ to frequency-space, allowing a reduction in data volume by a factor of two.

The GEP study assumes no on-board compression. However future study may verify the usability of lossless compression resulting in reduced DSN costs, relaxed telecommunications requirements, and/or improved margins.

### 4.6 Telecommunications

Over its mission, GEP downlinks over 350 TB of data by utilizing the DSN’s evolving Ka-band capability. GEP uses Ka-band downlink for science data and S-band for command and telemetry. A 0.65 m static HGA is baselined to reduce cost and vibration. It enables 132 Mbps science data downlink with 7.9 dB to the DSNs 34 m beam waveguide (BWG) ground stations. GEP carries two Ka-band TWTAs for redundancy should one fail. Furthermore, if DSN enables dual-polarization Ka-band downlink, GEP can downlink at 300 Mbps, reducing operations costs without any additional hardware. For persistent access, commanding, and telemetry, two low-gain S-band antennas offer  $4\pi$  steradian coverage.

### 4.7 Mission Operations

The GEP science operations impose a limited set of commanding requirements, allowing for simple operations. In addition to verifying spacecraft functionality, health, and beginning payload thermal operations, early observations of reference targets will be recorded in IQ0 and IQ1 data types. Ground processing of these reference target data will be used to optimize calibration, cosmic ray removal, and drift removal processing on-board such that  $\Delta f$  data will be transmitted during science operations (see

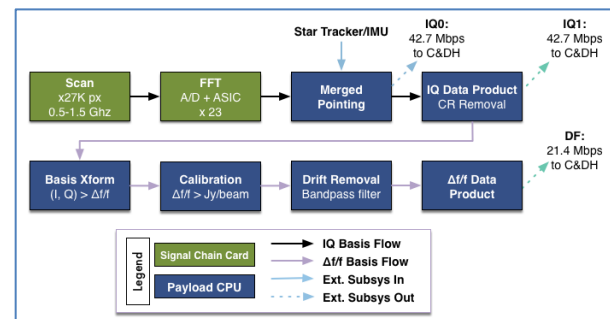


**Figure 25.** The onboard processing of GEP-I data is straightforward. The limited processing adds pointing information and reduces the stored data volume by performing a basis transformation.

Figure 25). During science operations, background sequences defining surveying, data downlink, and spacecraft health and safety maintenance can be uploaded weekly or less frequently. As survey-mode observations continue, one five-hour DSN pass per day is required to downlink 0.24 TB, the average daily data volume.

GEP Phase E science operations were designed with significant margin to the requirements in the STM. The survey depth and field requirements outlined in the STM require a 12,000 hour survey. However, the spacecraft has been designed and costed, along with required DSN time, to support a 17,500 hour survey - resulting in a 46% margin on observational efficiency. Additionally, GEP maintains data storage margin to permit for missed DSN passes in the event of poor weather at the ground station.

For this study, the GEP Team has assumed that mission operations are conducted from NASA JPL. However, pre-proposal study will select either NASA JPL or University of Colorado (CU) Boulder’s Laboratory for Atmospheric and Space Physics (LASP), which operated the *Kepler* spacecraft.

## 5 COST, RISK, AND HERITAGE ASSESSMENT

### 5.1 Cost Assessment

This study has generated two cost estimates for the GEP mission. The GEP Team and JPL Team X (JPL’s concurrent design facility) have estimated GEP’s lifecycle cost to be \$910M and \$951M FY18, respectively, as detailed in Table 10. Both estimates assume 30% development reserve on Phases A–D and 15% on operational reserves in Phase E, excluding WBS 7.03, as is standard practice. The Team X evaluation costed all aspects of the mission. The GEP Team cost was compiled based on estimates from Ball Aerospace and Team X. The costs presented in this report are ROM estimates; they are not point estimates or cost commitments. It is possible that each estimate could range from as much as 20% percent higher to 10% lower. The costs presented are based on Pre-Phase A design information, which is subject to change.

Two different approaches were used to cost the flight system. The JPL Team X flight system estimated WBS 6 to be \$232M, assuming an in-house build, resulting in a more conservative

estimate. The Ball Aerospace combined estimate of WBS 6 and 10 is \$200M and was derived from cost regression as a function of bus mass based on data from historical Class B missions using the BCP2000 bus. The Ball estimate includes an estimate of JPL institutional overhead.

GEP-I, GEP-S, associated payload electronics, optical assembly, and all active cooler components are costed as a part of the GEP payload. GEP-I and GEP-S were costed as a single instrument using NICM Version 8 as a passive RF instrument owing to the nature of their readout electronics and their identical operating temperatures. The NICM subsystem cost, reported by Team X, is \$59M. In order to account for the design and integration of multiple focal planes, the GEP team estimated a cost of \$84M for all the modules. This estimate was made by assuming that GEP would have a similar

**Table 10.** Both JPL Team X and the GEP Team estimated the cost of GEP. Both estimates are under the Probe cost cap, with substantial reserves available to mitigate cost growth. Note that the GEP Team estimate for WBS 6 Flight System includes WBS 10 ATLO.

Work Breakdown Structure (WBS) Elements	GEP Estimate	Team X Estimate
<b>Development Cost (Phase A-D)</b>	<b>\$661M</b>	<b>\$702M</b>
1.0, 2.0, & 3.0 Management, Systems Engineering, and Mission Assurance	\$54M	\$54M
4.0 Science	\$16M	\$16M
5.0 Payload System	\$195M	\$168M
5.01, 5.02 Payload Mgmt, SE	\$6M	\$6M
5.1 GEP-I	\$91M	\$64M
5.2 GEP-S		
5.3 Active Cooling	\$71M	\$71M
5.4 OTA	\$27M	\$27M
6.0 Flight System	\$200M	\$232M
7.0 Mission Op Preparation	\$17M	\$17M
9.0 Ground Data Systems	\$22M	\$22M
10.0 ATLO	*Included in WBS 6	\$26M
12.0 Mission and Navigation Design	\$5M	\$5M
Development Reserves (30%)	\$152M	\$162M
<b>Operations Cost (Phase E)</b>	<b>\$99M</b>	<b>\$99M</b>
1.0 Management	\$4M	\$4M
4.0 Science	\$44M	\$44M
7.0 Mission Operations	\$30M	\$30M
9.0 Ground Data Systems	\$9M	\$9M
Operations Reserves (15%)	\$12M	\$12M
<b>Launch Vehicle (LV)</b>	<b>\$150M</b>	<b>\$150M</b>
<b>Total Cost (including LV)</b>	<b>\$910M</b>	<b>\$951M</b>

ratio of non-sensor/sensor costs as *Spitzer* MIPS cost actuals, while fixing the sensor costs to the NICM 8 output. In both cases, the cost of focal plane integration is carried within this WBS line, while payload integration is carried in WBS 10 ATLO.

The cost of active cooling includes the ADR and cryocooler and is carried in WBS 5.3. The ADR cost for this study is an estimate from NASA Goddard Space Flight Center (GSFC). It assumes the provision of both a flight model and an engineering model. GSFC has produced ADRs for multiple spaceflight missions. The 4 K cryocooler cost for this study is based on the NICM VIII CER Cryocooler model, assuming a commercial build. GEP benefits from recent and ongoing investment by commercial suppliers of 4 K coolers as described in §5.3.

The optical assembly was costed using the Stahl model for a 24  $\mu\text{m}$ -diffraction limited, 4 K, 2.0 m primary mirror, resulting in \$27M.

Operations costs were estimated by Team X and adopted by the GEP Team. Additional study was performed to estimate the cost of operations at CU Boulder LASP. LASP cost estimates were generated for WBSs 7.0, 7.03, 9.0A, and 9.0B, and were found to be similar to the cost of conducting operations from NASA JPL. Thus, conducting operations from LASP remains an opportunity for future study.

The science effort, described by WBS 4, was generated by the GEP team and based on experience developing the software pipeline for *Herschel* SPIRE, delivery and archiving of SPIRE GTO data products, and GTO data analysis. This cost was passed through Team X and was accepted as a part of their estimate.

All other WBS elements were costed using the JPL Institutional Cost Model assuming a Class B mission with spacecraft built by a subcontractor. Team X estimates are generally model based, and were generated after a series of instrument and mission-level studies. Their accuracy is commensurate with the level of understanding typical to Pre-Phase-A concept development. They do not constitute an implementation or cost commitment on the part of JPL or Caltech.

### 5.1.1 Cost Trades and Descopes

GEP is able to perform transformative science under the Probe cost cap due to advances in detectors and RF electronics, its usage of a single detector

technology and FPA temperature, integration of GEP-I and GEP-S payload electronics, and advances in SiC mirror and technology.

Several trades remain for future study that can provide additional opportunity to reduce cost. First, investigation into the compressibility of KID's data stream output could reduce telecom requirements. Following this compressibility study, cost optimization trades evaluating operations location, downlink frequency, data rate, and telecom electronics remain for future study. Additionally, the propulsion system can be further simplified by evaluating upper stage performance to perform HOI, removing the need for GEP's main engine. Finally, expanding options for commercially available cryocooler in the following years may provide additional opportunities to reduce GEP cost.

## 5.2 Risk Assessment

The GEP mission architecture was based on a strategy of defining appropriate contingencies and margins and utilization of design strategies that mitigate potential mission risks. In this section, the risks to the GEP mission having the highest impact and likelihood are discussed. Future work will further quantify the impact and likelihood of these risks.

### 5.2.1 Development Risks

#### Focal Plane KID Arrays

GEP is expected to be the first space observatory using KID technology. Therefore, the GEP team will prepare multiple strategies to mitigate the development risk owing to their fabrication, integration, and test.

The first strategy is to begin detector development early in the project lifecycle and to reach TRL 6 quickly. The KID technology development plan in §6.1 anticipates achieving TRL 5 with all required new technologies by 2023, two years before the TRL 6 technology cutoff in 2025, at the end of Phase B.

The second strategy is used to reduce the risk of delayed down-selection of FPGA or ASIC readout technologies. A GEP Team key decision point in 2022, prior to project start, will be to evaluate the flight readiness of FPGA signal chain electronics, described in §6.2. If the FPGA option cannot be flight qualified in advance of a GEP proposal, its logic can be designed as an ASIC. By placing this

decision early in the GEP lifecycle, development cost and schedule risk are reduced.

The third strategy is to leverage the physically independent but very similar design of the focal planes. Because none of the GEP-S module boxes are coupled together and GEP-S and GEP-I are only physically connected at the microwave switch, each focal plane can be fabricated in parallel and unit tested extensively prior to integration, thereby mitigating potential schedule risk. We expect that focal planes will be built and unit tested at JPL, with final integration at the spacecraft vendor.

### *Primary Mirror*

A possible cost risk mitigation strategy is to maintain an option to select an adaptive SiC primary mirror should the technology become sufficiently mature by the project start. If this technology, described in §6.3, becomes available, it has the potential to reduce payload and systems I&T duration and cost by reducing iterations of OTA testing.

### *Payload Thermal*

Following selection, GEP will begin developing a payload thermal design that meet Class B requirements. Design requirements will define down-selection criteria for available cryocooler options, as laid out in §5.3.

Hardware development and test of detector payload and active payload thermal components will be done independently. Final integration and test will occur at the spacecraft vendor.

### *Cosmic Rays*

The GEP team will implement approaches in mission development and operations to mitigate the impact from cosmic rays. The KID readout electronics will be designed to mitigate the likelihood and impact of single-event upsets (SEUs) that would reduce instrument availability. Radiation testing will be a part of technology development and will quantify the impact of SEUs and the mitigation strategies. The microwave switches will also be tested to evaluate their susceptibility to radiation, although they are expected to be robust.

The strategy to minimize KID cosmic ray susceptibility is two-fold. First, the impacts of cosmic ray strikes to detector arrays will be limited to a small number of detectors by deposition of titanium on the semiconductor substrate. This has been shown to localize cosmic-ray-induced phonons

to nearest-neighbor detectors [Monfardini et al. 2016].

The second strategy is to reduce the impact of cosmic ray events, which will have unique and repeatable (exponential) time signatures, by performing on-board cosmic ray event removal. The removal algorithm will be similar to those successfully used by *Herschel* and *Planck*. During early GEP observations, observations will be performed and recorded as IQ0 data products. These data will be evaluated to optimize filtering methods that can be uploaded to the GEP spacecraft to create cosmic-ray-removed IQ1 and DF data products from IQ0 data.

### *5.2.2 Mission Risks*

#### *Payload Electronics Component Failure*

Although the flight validation process will assure the reliability of payload electronics components, the potential impact of their failure necessitates response to mitigate identifiable failure modes.

By design, GEP-I and GEP-S are resilient to failure. The payload electronics processor, memory, clock, and power cards are dual-string redundant in a hot/cold configuration. The highest-impact risk would be the failure of a signal chain card, where eight readout channels would be lost. To mitigate this impact, consecutively bands will not be read out on the same signal chain card. For example, GEP-I bands 16 and 17, covering 65-74 and 74-84  $\mu\text{m}$ , respectively, will not be read out by the same card. Thus a large range of spectral data would not be lost with the failure of a single card. As of this study, no other payload electronics failure will jeopardize GEP's ability to meet its science measurement requirements.

The second-highest impact risk is single readout circuit failure. In such an event, a single GEP-I band and portion of a GEP-S band is lost, limiting its impact to a narrow range of spectrum.

The third-highest impact risk is microwave switch failure. GEP reduces the likelihood of this risk by minimizing the use of the microwave switches to only once in the mission following checkout. The impact itself is constrained to only one GEP-I band and portion of a GEP-S band, therefore limiting the science impact to a narrow range in spectrum.

If the chopping mirror fails, GEP-I (which does not use it) will operate normally, as will the GEP-S

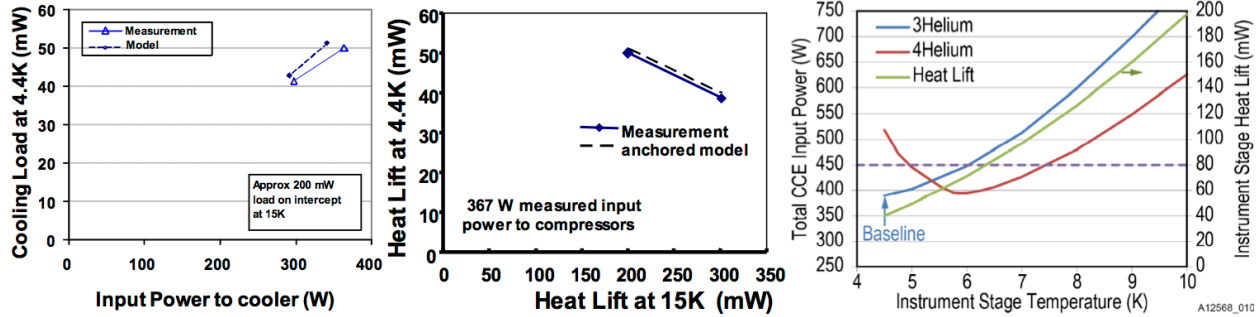


**Figure 26.** *Left, Center:* NGAS results for a 2-stage JT system showing 100% margin on GEP thermal loads, for both modeled and measured performance [Raab et al. 2013]. *Right:* Predicted Ball cooler performance for a point design supporting a mission with similar thermal requirements to GEP, demonstrating 100% margin at 4.5 K relative to GEP requirements.

spectral mapping mode. The GEP-S pointed spectral mode will suffer from  $1/f$  noise and have reduced sensitivity. Therefore, most of the mission objectives—all but the first part of Objective 2—will still be possible.

### Contamination

In this study, GEP has acknowledged the risk of contamination that can impact telescope performance. The GEP mission does not use a telescope barrel or cover to limit dust and particle contamination during the final stages of ATLO. Given the size of dust, the GEP waveband, and requirements that can be levied upon the launch vehicle fairing, there is a small likelihood of dust contamination impacting optical quality or throughput to impact observations. In order to limit deposition of outgassed volatiles upon optics after launch, GEP will remain warm until outgassing is completed, similar to [Planck Team 2013].

## 5.3 Heritage Assessment

### Cryocoolers and ADR

GEP has two active cooling technologies: a hybrid cryocooler for cooling to 18 K and 4 K, and an ADR for cooling to 1 K and 100 mK. All technology development has been completed for both the hybrid cooler and the ADR. The only remaining work to be done is in engineering implementation specific to GEP requirements.

The GEP ADR requires no new additional technology development to meet required performance. GSFC has a well-established program for ADR development [Shirron et al. 2000; Shirron and Pirro 2005], with most individual components at TRL 9. A continuous ADR design with five salt pills and four cooling stages has been proposed by

Shirron that utilizes these high TRL components to provide significant margin to GEP requirements at both 1 K and 100 mK.

There are multiple approaches to implementing the hybrid cooler, with one option from Ball and another from Northrop Grumman Aerospace Systems (NGAS). An approach proposed by Ball Aerospace as a point design for a mission with similar requirements utilizes the existing TIRS-2 mechanical Stirling cryocooler with an optimized regenerator for lower-temperature operation. This optimization is a well understood and common modification in cryocoolers and does not qualify as technology development. The JT cooling system uses the same compressor as the TIRS-2 Stirling Cryocooler with valving to circulate the  $^3\text{He}$  working fluid.

Additionally, the Ball cooler uses warm bypass valves for precooling the system. This eliminates the need for cold valves, which proved to be a development challenge in the construction of the MIRI cooler. Ball generated a point design for another mission with similar requirements to GEP and 100% margin above GEP loads (Figure 26). Ball showed good results for a similar cooler during Advanced Cryocooler Technology Development Program (ACTDP) development [Glaister et al. 2005]. Ball is also assessing multistage JT coolers to increase the compression ratio and improve efficiency.

NGAS implemented the ACTDP to support JWST, which resulted in the development of the 6 K flight cooler for the MIRI instrument. This cooler uses an acoustic pulse-tube Stirling cooler as the precooler and a  $^4\text{He}$  JT cooler for 6 K heat lift. Using the existing MIRI JT compressor with  $^3\text{He}$  as the

system working fluid could give improved performance at 4.5 K. Scaling from existing performance data indicates that it could meet the thermal requirements of GEP with >100% margin. This would only drive minor engineering work, such as optimizing the  $^3\text{He}$  performance of heat exchangers. Additionally, NGAS has been developing a multistage compressor for the JT cooling loop that would allow very high compression ratios suitable for high-efficiency operation with  $^4\text{He}$  at 4.5 K [Raab et al. 2013]. With high compression ratios,  $^4\text{He}$  is more efficient than  $^3\text{He}$  at this temperature. This design is expected to be fully developed well before GEP mission implementation. NGAS has already collected data and models showing performance with  $\sim 100\%$  margin above GEP requirements (Figure 26).

### Bus Development

GEP does not baseline any specific spacecraft bus design, but was evaluated using the Ball Configurable Platform (BCP) spacecraft that has successfully supported 12 missions on orbit, with five more in development. The GEP spacecraft design draws directly from this extensive history by using the same flight-qualified components and designs. The legacy BCP modular spacecraft design provides flexibility in I&T flow and enhances schedule assurance via parallel manufacturing and integration of the spacecraft.

### Optical assembly

GEP is baselining non-actuated SiC optics, with a braze-joined primary mirror. This process was used for the *Herschel* primary mirror and is currently used by several domestic contractors.

### Operations

The GEP operations are expected to be performed either at NASA JPL or CU LASP, with both having extensive experience in operating and maintaining space observatories.

## 6 TECHNOLOGY MATURATION PLAN

With a launch in 2029, all technologies required for the GEP mission must be at or above TRL 6 in 2025. As detailed in this section, The GEP Team plans to achieve TRL 6 technologies in advance of 2025.

### 6.1 Kinetic Inductance Detectors

GEP will leverage existing KIDs technology development and planned future work to mature

KIDs technology in advance of a GEP proposal. Of the existing demonstrations shown in Figure 20, the European SPACEKIDs results [Baselmans et al. 2017] are the closest to meeting the GEP requirements, which are listed in Table 11. By comparing the capability gap between GEP KID focal plane requirements and SPACEKIDs performance, specific advances required to achieve TRL 6 by 2025 can be identified:

- **Wavelength range:** To support GEPs wavebands, absorber-coupled detectors are required (Figure 21), which represents an improvement over the antenna-coupled  $\lambda = 350\ \mu\text{m}$  SPACEKIDs design. Additionally, a modified absorber design is needed at shorter wavelengths ( $\lambda = 10\ \mu\text{m}$ ).
- **Sensitivity:** GEP-S requires at least a  $3\times$  improvement in NEP over SPACEKIDs. This can be achieved through reducing the detector active volume (thereby increasing the quasiparticle density, and hence responsivity) below the  $\sim 100\ \mu\text{m}^3$  used by SPACEKIDs [Hailey-Dunsheath 2018].
- **Multiplexing:** The minimum detector-multiplexing factor for GEP is 1,500 pixels per GHz of readout bandwidth. This  $6\times$  increase in multiplex factor relative to SPACEKIDs is based on a  $6\times$  reduction in readout frequency, from 6 GHz to 1 GHz (band center). Multiplex factors of 6,500 per GHz have been demonstrated at 200 MHz readout frequency [Swenson et al. 2012]. Further improvements are likely using post-fabrication resonator trimming methods [Liu et al. 2017; Shu et al. 2018].
- **Pitch:** The baseline pixel pitch of GEP-I is  $300\ \mu\text{m}$  from wavelengths of 10 to  $60\ \mu\text{m}$  to provide 3.43 arcsecond resolution. For GEP-S, the pixel pitch is  $300 \times 600\ \mu\text{m}$  to meet the spectral resolution requirement. Both are smaller than the  $1,600\ \mu\text{m}$  SPACEKIDs pitch, which was driven by their optics/antenna design. The GEP requirements can be met with area-efficient resonator designs and deep-UV lithography [JPL/MDL 2018]. Smaller pixels generally have higher readout frequency, which presents an engineering design trade space of pitch versus readout frequency.

**Table 11.** Detector requirements for GEP versus results achieved for SPACEKIDs [Baselmans et al. 2017].

	Tile Size (pixels)	$\lambda$ ( $\mu\text{m}$ )	NEP ( $\text{W Hz}^{-1/2}$ )	MUX (pix/GHz)	Pitch ( $\mu\text{m}$ )	$\tau_{\text{det}}$ (ms)	Min. Yield	Dynamic Range	Crosstalk (dB)	1/f knee (Hz)	Cosmic Ray Deadtime
<b>SPACEKIDs</b>	961	350	$3 \times 10^{-19}$	240	1600	1.5	83%	$10^5$	-30	0.2	< 5%
<b>GEP-I</b>	1,440	10–400	$7 \times 10^{-19}$	1,500	300	< 4	80%	5,000	-17	< 1	< 2%
<b>GEP-S</b>	980	24–193	$1 \times 10^{-19}$	1,500	300 × 600	< 4	80%	1,000	-17	< 1	< 2%

Notes: Minimum tile sizes for GEP-I/GEP-S shown; actual arrays could be multiples thereof. Tiles with  $12 \times 120 = 1,440$  pixel format are envisioned for GEP-I bands 1–18. GEP-S bands 1 & 2 assume arrays with  $112 \times 70$  format, which could consist of tiles with  $28 \times 35 = 980$  pixels. The dynamic range is specified for a 1 Jy calibration source, e.g., an asteroid [Müller et al. 2014; Baselmans et al. 2017]. Techniques to mitigate electrical and optical crosstalk, and cosmic ray susceptibility, have been demonstrated [Noroozian et al. 2012; Baselmans et al. 2017; Yates et al. 2017].

*Planned Activities, Schedule and Milestones, and Estimated Cost*

Recent, ongoing, and future key technology demonstrations that lead to GEP’s (and OST’s) requirements are listed in Table 12 and overviewed in Figure 27. All of the table rows below SPACEKIDs are, or are expected to be, NASA funded. Cumulatively, the table presents a pathway from state-of-the-art (SPACEKIDs and STARFIRE-p) wavebands, detector counts, and sensitivities through to GEP and OST requirements.

A newly selected 3-year CIT/JPL/CU NASA APRA program will demonstrate kilopixel-scale KID arrays meeting our KIDs requirements [Hailey-Dunsheath et al. 2018]. A small KID array has already flown on the Italian OLIMPO balloon payload [Paiella et al. 2018] and the BLAST-TNG 3.3 kilopixel KID focal plane is scheduled for an Antarctic balloon flight in December 2018 [Lourie et al. 2018]. Kilopixel-scale, far-infrared aluminum KID arrays can also be fully demonstrated using the newly-selected STARFIRE NASA balloon payload [Aguirre and Collaboration 2018] and/or through the proposed KID upgrade for the FIFI-LS SOFIA instrument [Looney 2018].

A planned GEP balloon precursor (GEP-B) would enable absorber-coupled GEP-prototype mid- and far-infrared KID arrays to be demonstrated. A three-year, \$8M, 6 FTE/year focused technology development program (GEP-TD) would be needed following the 2020 Decadal survey (assuming a NASA Astrophysics Probe class is endorsed), leading to demonstration of GEP prototype arrays at the TRL-5 level by mid-CY23. A subsequent technology maturation program (GEP-TM) that included space qualification activities would reach TRL-6 by 2025.

**Table 12.** Major detector technology demonstrations leading to GEP and beyond.

Project	Date	Type	Detector Count (pixels)	NEP ( $\text{W Hz}^{-1/2}$ )	Wavelength ( $\mu\text{m}$ )
SPACEKIDs	2014–17	Lab	1,000	$3 \times 10^{-19}$	350
STARFIRE-p	2017–18	Lab	45	$4 \times 10^{-18}$	350
APRA	2019–22	Lab	1,000	$1 \times 10^{-19}$	10–350
FIFI+LS	2018–22	SOFIA	9,856	$< 1.5 \times 10^{-17}$	51–206
STARFIRE	2019–23	Balloon	3,600	$< 1 \times 10^{-17}$	240–420
GEP-TD	2020–23	Pre-phase A	1,440	$1 \times 10^{-19}$	10–400
GEP-B	2020–24	Balloon	3,000	$< 5 \times 10^{-17}$	10–400
GEP-TM	2023–25	Phase A	1,440	$1 \times 10^{-19}$	10–400
GEP-I	2025+	Probe	25,735	$1 \times 10^{-19}$	10–400
GEP-S	2025+	Probe	24,640	$1 \times 10^{-19}$	24–193
OST-OSS	2030+	Flagship	60,000	$2 \times 10^{-20}$	25–589

Notes: The SPACEKIDs [Baselmans et al. 2017] and STARFIRE-p [Baris et al. 2018] programs are already completed. The APRA [Hailey-Dunsheath 2018] and STARFIRE [Aguirre and Collaboration 2018] programs were selected for funding by NASA, and FIFI+LS [Looney 2018] has been proposed.

**6.2 Detector Readout Electronics**

Because GEP will have a potential option to use either FPGA or ASIC technology for its detector readout electronics, we plan to utilize cost-effective FPGA options over the course of the development outlined in §5.1 and to downselect from the two technologies in 2022. This will provide sufficient time to mature and flight validate, if needed, the selected technology in advance of 2025.

To date, all KID instrument readout systems use field-programmable gate arrays (FPGAs) [Trimberger 2015] for the digital channelization. This channelization is conceptually equivalent to an FFT, and sometimes implemented as such [Yates et al. 2009; van Rantwijk et al. 2016]. Table 12 lists the characteristics of selected Xilinx FPGAs spanning several generations of CMOS technology, from the

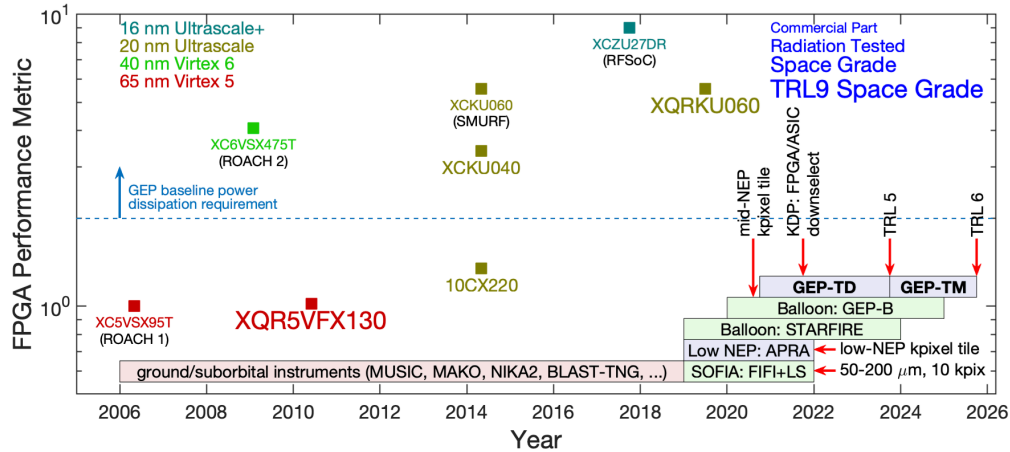


**Figure 27.** GEP has developed a robust plan to mature KIDs and payload electronics technologies in advance of a Probe-class proposal through laboratory (shaded in red), SOFIA and balloon-borne experiments (green), and system-level demonstrations (blue) starting in 2019. Their key parameters are listed in Table 12. In the top of the figure, feasibility of GEP readout electronics is illustrated using the evolution of Xilinx FPGA capability over time. Specific devices are plotted as points labeled by the part number, with data sheets listed in the references. The horizontal axis gives the introduction date, and the vertical axis is a composite performance metric that combines the number of logic gates and DSP cells, memory, and IO capability. The dashed blue line indicates the approximate minimum capability required for meeting the GEP baseline power dissipation of 25 W per 1 GHz readout channel. Color is used to indicate the CMOS technology node while font size indicates suitability for use in the space radiation environment. The XQRKU060, which Xilinx plans to release as a space-grade part in 2020, is a strong candidate for GEP. All work by the GEP Team will feed forward to TRL 6 validation of all hardware required for GEP’s payload by 2025.

65 nm Virtex-5 family to the latest 16 nm FinFET Ultrascale+ family [Xilinx 2015a]. First-generation KID readouts [Duan et al. 2010; Duan 2015; McHugh et al. 2012; Swenson et al. 2012] typically used Virtex-5 [ROACH-1 2008] hardware to process a 500 MHz bandwidth using about 50 W, across which up to 4,000 KIDs could be multiplexed [Swenson et al. 2012]. Similarly, the CORE mission study [De Bernardis et al. 2018] concluded that a 1 GHz bandwidth could be read with 50 W using existing space-grade, TRL-9 Virtex-5 FPGAs [Elftmann 2018].

Newer-generation FPGAs could allow 10× lower power as illustrated in Table 13 [Xilinx 2015b]. Given the very strong interest in the use of

advanced FPGAs in space [Wirthlin 2013; Swift 2017; SEE 2018; SEFUW 2018; Le Mauff 2018; Wang et al. 2018], one can expect additional options than the Virtex-5 to be available by the time GEP would enter Phase A. Thus, the laboratory figure of 50 W per 1 GHz channel is conservative.

Radiation test results on late-generation FPGAs obtained at Sandia, JPL, and elsewhere [Lee et al. 2015; Lee 2017; Elftmann 2018; Allen and Vartanian 2018] have been positive. As a result, Xilinx has formally announced that the 20 nm KU060 FPGA (used in the SMURF readout electronics developed at SLAC) [Henderson et al. 2018] will be available as a space-rated product by late 2020 [Elftmann 2018]. This bodes well for even

**Table 13.** Field programmable gate arrays for detector readout. Data sheets are listed in references.

Device	Node (nm)	Logic Cells	DSP Slices	Block RAM	PLL	Transceivers	I/O Pins	Notes
XC5VSX95T	65	94 k	640	8.8 Mb	6	16 (3.75 Gb/s)	640	ROACH-1
XQR5VFX130	65	131 k	320	10.7 Mb	6	18 (4.25 Gb/s)	836	TRL 9
10CX220	20	220 k	192	12.5 Mb	10	16 (12.5 Gb/s)	284	Radiation tested
XC6VSX475T	40	476 k	2,016	38.3 Mb	18	36 (6.60 Gb/s)	840	ROACH-2
XCKU040	20	530 k	1,920	21.1 Mb	10	16 (12.5 Gb/s)	468	Radiation tested
XQRKU060	20	726 k	2,760	38 Mb	12 × 2	32 (12.5 Gb/s)	516	Space-qualified 12/2020
XCZU27DR	16	930 k	4,272	38 Mb	8 × 2	16 (16.3 Gb/s)	299	RFSoc; FinFET

more advanced options such as the new 16 nm FinFET Xilinx RF-system on chip (RFSoc) which integrates eight ADCs, eight DACs, and considerable FPGA logic into a single chip (Table 12); the entire GEP readout could potentially be reduced to 1 or 2 such chips. A board with this chip has been released [Abaco 2018]; initial power dissipation estimates are well below our conservative assumption of 25 W per 1 GHz channel. Alternatively, mixed-signal application-specific integrated circuits (ASICs) that integrate ADCs and signal processing have been developed at JPL for similar applications [Hsiao et al. 2015].

#### *Planned Activities, Schedule and Milestones, and Estimated Cost*

Concurrent with the GEP-TD focused detector technology effort described in §6.1, a parallel 3-year, 3-FTE, \$3M effort to define and develop a readout electronics solution for GEP will start in 2020. This effort would explore hardware and algorithm options using commercially available components and tools, evaluate the options for flight hardware taking into account FPGA radiation test results and industry announcements.

In 2022, the GEP team will downselect from the available FPGA technologies or begin development on an ASIC based on the FPGA logic used in technology work discussed in this section. A low-power ASIC implementation of the chosen algorithm/logic could be undertaken if the FPGA solution is not projected to reach the required TRL before the technology cut-off date.

### **6.3 Telescope Optics**

GEP is baselining a 2 m non-actuated, SiC primary mirror (PM) and does not require any new technology development. *Herschel's* 3.5 m diameter SiC primary mirror, the largest developed for a space telescope, was developed by Astrium Aerospace in collaboration with Boostec Industries. SiC was chosen due to its high specific stiffness, low thermal diffusivity, and suitability for cryogenic temperatures. Facility limitations restrict the size of monolithic parts to approximately 1.7 m × 1.2 m. The *Herschel* primary mirror was manufactured by joining together 12 individual wedge-like segments using a non-reactive, high-temperature brazing process. The process developed produces thin joints, with material properties matching that of the parent SiC material. Once brazed, subsequent polishing steps can occur on traditional large aperture

polishing machines with final surface roughness values in the 1–5 nm RMS regime. The *Herschel* primary mirror was extremely lightweight, with a total mass of 210 kg (22 kg/m<sup>2</sup>) while achieving high stiffness (50 Hz first mode) [Sein et al. 2003].

The process developed by Astrium/Boostec has been repeated for other space missions including GAIA (1.45 m × 0.5 m) [Bougoïn and Lavenac 2011] and AEOLUS/ALADIN (1.5 m dia.) [Logut et al. 2005]. Several other manufacturers developed their own SiC processes. Notably, AOA Xinetics has developed a slip-cast process to produce lightweight (< 10 kg/m<sup>2</sup>) mirrors. Larger mirrors like the 2.0 m GEP primary can be produced through brazing techniques (reactive or non-reactive) or through a slip-bonding process. Monolithic parts have been demonstrated in the 1.5 m diameter range, which will be used for GEPs secondary and tertiary mirrors.

Although GEP baselines a non-actuated mirror, GEP development and integration costs may be reduced by using an active primary mirror with distributed figure control actuators. In a technique developed AOA Xinetics in partnership with JPL, piezoelectric actuators are embedded into the backside of a lightweight SiC mirror substrate [Hickey et al. 2010]. These actuators provide in-situ wavefront correction capabilities and can be used to correct thermally induced figure distortions, gravity sag, and long-term material creep. As a result, cost and complexity may be reduced because manufacturing tolerances can be relaxed as a result of the embedded figure control. More savings can be realized during telescope I&T as on-orbit performance specifications are achieved under a variety of test conditions (i.e., room/cryogenic temperatures, zero/1 g). A significant amount of work has been performed in this area for room temperature, visible-wavelength applications.

#### *Planned Activities, Schedule and Milestones, and Estimated Cost*

No new technology development is required for passive SiC optics. Activities are underway at JPL to extend the capabilities of active SiC mirrors to cryogenic, far-infrared applications with a full-scale demonstration expected to be complete in the 2021 timeframe [Steeves et al. 2018]. A 1.2 m deformable primary mirror is planned for the GEP-B balloon to demonstrate this technology.

## 7 MANAGEMENT PLAN

For the purpose of developing a GEP mission concept of sufficient maturity for costing, the GEP study made the following assumptions. The study evaluated GEP as being led by PI Prof. Jason Glenn (CU Boulder). He will be responsible for the success of the investigation and its execution within the project’s cost and schedule. NASA JPL will manage and oversee all aspects of technical work, including coordination with a spacecraft vendor should the flight system be subcontracted. Either NASA JPL or CU Boulder LASP will manage spaceflight operations.

Prior to Phase A, the technology development plan will prepare key technologies for GEP and build the collaborative structure, with participation by JPL, CU, a subcontractor, and scientists at various institutions. As detailed in the previous section, technology development work is expected to meet TRL 6 prior to 2023, over two years before Phase B.

Figure 28 outlines the high-level project schedule for GEP, with critical milestones and phase durations similar to other Class B NASA missions. At the latest, the beginning of Phase C will see the development of focal planes, payload electronics, optics, and cryogenics at different locations. JPL will be responsible for development of focal-plane and payload electronics while subcontracting telescope and cryocooler development. JPL or a spacecraft vendor will be responsible for integrating the bus and payload. An instrument scientist (JPL) and a deputy instrument scientist (CU) will be appointed to oversee instrument unit build/test and payload I&T.

Either NASA JPL or CU LASP will manage mission operations. Science will be coordinated between JPL and CU, along with domestic and

international collaborating scientists and their institutions.

## 8 CONCLUSIONS

The 2010 Decadal Survey called upon the astronomical community to “Use telescopes as time machines to map the full history of galaxy formation and assembly, from the birth of the first stars through the turbulent epoch of rapid growth, to the galaxies we see today.” Because much of this transformation and cycling of gas into collapsed structures has occurred in deeply embedded regions of galaxies, long-wavelength measurements are essential.

GEP is a mid-IR and far-IR observatory optimized for sensitivity to star formation to answer this call. GEP will trace the history of star formation in galaxies from high redshifts, by utilizing the power of gravitational lensing, through the epoch of rapid growth with deep and wide surveys, to the local universe with spectral line mapping of nearby galaxies and the Milky Way. GEP will achieve this under the Probe \$1B cost cap with a mission optimized for dedicated surveys that simplify instrument design and operations, and thereby minimize cost. The surveys will produce a powerful legacy data set for use in conjunction with complementary facilities of the next two decades, including: WFIRST, Euclid, eROSITA, ALMA, and ultimately OST and LUVOIR.

As a Class B mission, GEP takes advantage of high-heritage technologies for the majority of its subsystems, such as the bus, ACS, and cryogenics. GEPs science and Probe-class cost are enabled by new detector technology—KIDs—that came on the scene less than two decades ago and has already been implemented in numerous astronomical observatories. GEPs technology development will bring the detector and readout technology to TRL 6 and demonstrate system-level performance of

CY	2023				2024				2025				2026				2027				2028				2029				2030				2031				2032				2033				2034			
Fiscal Quarter	2	3	4	1	2	3	4	1	2	3	4	1	2	3	4	1	2	3	4	1	2	3	4	1	2	3	4	1	2	3	4	1	2	3	4	1	2	3	4	1	2	3	4	1				
Project Phase					A				B				C/D				E				F																											
Key Milestones									PDR				CDR				ARR				KDP E																KDP F											

**Figure 28.** The GEP project schedule is in-class with other Class B NASA missions. With a five-year design life, GEP will have the option for an extended science mission following the baselined four years of operations.

optics, detectors, and readout on a pathfinder balloon, GEP-B. This GEP concept study has shown the powerful science that can be accomplished on a Probe budget, enabling NASA Astrophysics to have multiple major missions per decade for a broad science portfolio that will engage a large part of the astronomical community.

## **APPENDIX A - ACRONYMS**

ACS	Attitude Control Subsystem
ACTDP	Advanced Cryocooler Technology Development Program
ADR	Adiabatic Demagnetization Refrigerator
AGN	Active Galactic Nuclei
ALMA	Atacama Large Millimeter Array
ASIC	Application-Specific Integrated Circuit
BCP	Ball Configurable Platform
BWG	Beam Waveguide
C&DH	Command and Data Handling
CBE	Current Best Estimate
COTS	Commercial, Off-The-Shelf
CU	University of Colorado Boulder
DF	Delta Frequency: KID resonator frequency shift, also written $\Delta f$
EQW	Equivalent Width
ESA	European Space Agency
FFT	Fast Fourier Transform
FPA	Focal Plane Array
FPGA	Field-Programmable Gate Array
GEP	Galaxy Evolution Probe
GEP-DSS	Galaxy Evolution Probe – Deep Spectral Survey
GEP-I	Galaxy Evolution Probe – Imager
GEP-S	Galaxy Evolution Probe – Spectrometer
GEP-WSS	Galaxy Evolution Probe – Wide Spectral Survey
HELP	Herschel Extragalactic Legacy Project
HGA	High-Gain Antenna
I&T	Integration and Test
IQ	Intensity-Quadrature
IR	Infrared
IRAS	Infrared Astronomical Satellite
ISM	Interstellar Medium
ISO	Infrared Space Observatory
JAXA	Japanese Aerospace Exploration Agency
JWST	James West Space Telescope
KID	Kinetic Inductance Detector
LASP	Laboratory for Atmospheric and Space Physics
LIM	Line Intensity Mapping
LSST	Large Synoptic Survey Telescope
LUVUIR	Large Ultraviolet Optical Infrared Surveyor
LV	Launch Vehicle
MO&DS	Mission Operations & Data Systems
NEP	Noise Equivalent Power
NGAS	Northrop Grumman Aerospace Systems
OST	Origins Space Telescope
OTA	Optical Telescope Assembly
PAH	Polycyclic Aromatic Hydrocarbon

PCA	Principal Component Analysis
PM	Primary Mirror
RF	Radio-Frequency
RFSoc	RF-System on Chip
ROM	Rough Order of Magnitude
RWA	Reaction Wheel Assembly
SCUBA	Submillimeter Common User Bolometer Array
SED	Spectral Energy Distribution
SEU	Single Event Upsets
SFR	Star Formation Rate
SiC	Silicon Carbide
SKA	Square Kilometer Array
SMBH	Supermassive Black Hole
SNR	Signal-to-Noise Ratio
SPICA	Space Infrared telescope for Cosmology and Astrophysics
SPT	South Pole Telescope
STM	Science Traceability Matrix
TCM	Trajectory Correction Maneuver
TES	Transition-Edge Sensor
TMA	Three-Mirror Astigmat
UV	Ultraviolet
WFIRST	Wide Field Infrared Survey Telescope
XID+	Cross IDentification Code

## APPENDIX B - REFERENCES

- Abaco, Systems. 2018. "The VP430: direct RF processing system." <https://www.abaco.com/products/vp430-rfsoc-board>.
- Adam, Remi, Amar Adane, PAR Ade, Philippe André, Aina Andrianasolo, Herve Aussel, Alexandre Beelen, Alain Benoit, Aurelien Bideaud, and Nicolas Billot. 2018. "The NIKA2 large-field-of-view millimetre continuum camera for the 30 m IRAM telescope." *Astronomy & Astrophysics* 609:A115.
- Aguirre, James, and STARFIRE Collaboration. 2018. "STARFIRE: The Spectroscopic Terahertz Airborne Receiver for Far-InfraRed Exploration." American Astronomical Society Meeting Abstracts.
- Allen, Gregory A., and S. Vartanian. 2018. "NEPP FPGA Update FY18 V2." NASA Electronic Parts and Packaging (NEPP) Program 2018 Electronics Technology Workshop, Building 3 Auditorium, at the NASA Goddard Space Flight Center in Greenbelt, MD.
- Armus, Lee, V Charmandaris, J Bernard-Salas, HWW Spoon, JA Marshall, SJU Higdon, V Desai, HI Teplitz, L Hao, and D Devost. 2007. "Observations of ultraluminous infrared galaxies with the infrared spectrograph on the Spitzer Space Telescope. II. The IRAS bright galaxy sample." *The Astrophysical Journal* 656 (1):148.
- Ball Aerospace. 2018. "CT-2020." [https://www.ball.com/aerospace/Aerospace/media/Aerospace/Downloads/D3408\\_CT2020\\_0118.pdf?ext=.pdf](https://www.ball.com/aerospace/Aerospace/media/Aerospace/Downloads/D3408_CT2020_0118.pdf?ext=.pdf).
- Barlis, Alyssa, Steven Hailey-Dunsheath, James E Aguirre, Charles M Bradford, Joseph G Redford, Tashalee S Billings, Henry G LeDuc, Christopher M McKenney, and Matthew I Hollister. 2018. "Development of aluminum LEKIDs for balloon-borne far-infrared spectroscopy (Conference Presentation)." Millimeter, Submillimeter, and Far-Infrared Detectors and Instrumentation for Astronomy IX.
- Baselmans, JJA, J Bueno, Stephen JC Yates, O Yurduseven, N Llombart, K Karatsu, AM Baryshev, L Ferrari, A Endo, and DJ Thoen. 2017. "A kilo-pixel imaging system for future space based far-infrared observatories using microwave kinetic inductance detectors." *Astronomy & Astrophysics* 601:A89.
- Battersby, Cara, Lee Armus, Edwin Bergin, Tiffany Kataria, Margaret Meixner, Alexandra Pope, Kevin B. Stevenson, Asantha Cooray, David Leisawitz, Douglas Scott, James Bauer, C. Matt Bradford, Kimberly Ennico, Jonathan J. Fortney, Lisa Kaltenecker, Gary J. Melnick, Stefanie N. Milam, Desika Narayanan, Deborah Padgett, Klaus Pontoppidan, Thomas Roellig, Karin Sandstrom, Kate Y. L. Su, Joaquin Vieira, Edward Wright, Jonas Zmuidzinas, Johannes Staguhn, Kartik Sheth, Dominic Benford, Eric E. Mamajek, Susan G. Neff, Sean Carey, Denis Burgarella, Elvire De Beck, Maryvonne Gerin, Frank P. Helmich, S. Harvey Moseley, Itsuki Sakon, and Martina C. Wiedner. 2018. "The Origins Space Telescope." *Nature Astronomy* 2 (8):596-599. doi: 10.1038/s41550-018-0540-y.
- Benson, AJ, RG Bower, CS Frenk, Cedric G Lacey, CM Baugh, and Shaun Cole. 2003. "What shapes the luminosity function of galaxies?" *The Astrophysical Journal* 599 (1):38.
- Benson, Andrew J. 2012. "G ALACTICUS: A semi-analytic model of galaxy formation." *New Astronomy* 17 (2):175-197. doi: 10.1016/j.newast.2011.07.004.
- Bernard-Salas, J., S. R. Pottasch, D. A. Beintema, and P. R. Wesselius. 2001. "The ISO-SWS spectrum of planetary nebula NGC 7027." *Astronomy & Astrophysics* 367 (3):949-958.
- Berta, S, B Magnelli, R Nordon, D Lutz, S Wuyts, B Altieri, P Andreani, H Aussel, H Castaneda, and J Cepa. 2011. "Building the cosmic infrared background brick by brick with Herschel/PEP." *Astronomy & Astrophysics* 532:A49.
- B  thermin, Matthieu, Emanuele Daddi, Georgios Magdis, Mark T Sargent, Yashar Hezaveh, David Elbaz, Damien Le Borgne, James Mullaney, Maurilio Pannella, and V  ronique Buat. 2012. "A

- unified empirical model for infrared galaxy counts based on the observed physical evolution of distant galaxies." *The Astrophysical Journal Letters* 757 (2):L23.
- Bougoin, Michel, and Jérôme Lavenac. 2011. "From Herschel to Gaia: 3-meter class SiC space optics." *Optical Manufacturing and Testing IX*.
- Bourrion, O., A. Benoit, J. L. Bouly, J. Bouvier, G. Bosson, M. Calvo, A. Catalano, J. Goupy, C. Li, J. F. Macías-Pérez, A. Monfardini, D. Tourres, N. Ponchant, and C. Vescovi. 2016. "NIKEL\_AMC: readout electronics for the NIKA2 experiment." *Journal of Instrumentation, Volume 11, Issue 11, pp. P11001 (2016)*. 11:P11001. doi: 10.1088/1748-0221/11/11/P11001.
- Bower, Geoffrey, Garrett Keating, Dan Marrone, David DeBoer, Tzu-Ching Chang, Ming-Tang Chen, Homin Jiang, Patrick Koch, Derek Kubo, and Chao-Te Li. 2015. "Intensity Mapping of Molecular Gas at High Redshift." *IAU General Assembly 22*.
- Bower, R. G., A. J. Benson, R. Malbon, J. C. Helly, C. S. Frenk, C. M. Baugh, S. Cole, and C. G. Lacey. 2006. "Breaking the hierarchy of galaxy formation." *Monthly Notices of the Royal Astronomical Society (MNRAS)* 370 (2):645-655. doi: 10.1111/j.1365-2966.2006.10519.x.
- Bradford, Charles M, Bruce Cameron, Bradley D Moore, Lee Armus, and Alexandra Pope. 2018. "The Origins Survey Spectrometer (OSS): a far-IR discovery machine for the Origins Space Telescope (Conference Presentation)." *Space Telescopes and Instrumentation 2018: Optical, Infrared, and Millimeter Wave*.
- Calzetti, Daniela. 2013. "Star Formation Rate Indicators." In *Secular Evolution of Galaxies*, edited by Jesús Falcón-Barroso and Johan H. Knapen, 419. Cambridge, UK: Cambridge University Press.
- Casey, Caitlin M, Desika Narayanan, and Asantha Cooray. 2014. "Dusty star-forming galaxies at high redshift." *Physics Reports* 541 (2):45-161.
- Chapman, Scott C, AW Blain, RJ Ivison, and Ian R Smail. 2003. "A median redshift of 2.4 for galaxies bright at submillimetre wavelengths." *Nature* 422 (6933):695.
- Cheng, Yun-Ting, Tzu-Ching Chang, James Bock, C. Matt Bradford, and Asantha Cooray. 2016. "Spectral Line De-confusion in an Intensity Mapping Survey." *The Astrophysical Journal* 832 (2):165.
- Cleary, Kieran, Marie-Anne Bigot-Sazy, Dongwoo Chung, Sarah E. Church, Clive Dickinson, Hans Eriksen, Todd Gaier, Paul Goldsmith, Joshua O. Gundersen, Stuart Harper, Andrew I. Harris, James Lamb, Tony Li, Ryan Munroe, Timothy J. Pearson, Anthony C. S. Readhead, Risa H. Wechsler, Ingunn Kathrine Wehus, and David Woody. 2016. "The CO Mapping Array Pathfinder (COMAP)." 227th Meeting of the American Astronomical Society with High Energy Astrophysics Division (HEAD) and Historical Astronomy Division (HAD), Kissimmee, FL, 01/2016.
- Crites, A. T., J. J. Bock, C. M. Bradford, T. C. Chang, A. R. Cooray, L. Duband, Y. Gong, S. Hailey-Dunsheath, J. Hunacek, P. M. Koch, C. T. Li, R. C. O'Brient, T. Prouve, E. Shirokoff, M. B. Silva, Z. Staniszewski, B. Uzgil, and M. Zemcov. 2014. "The TIME-Pilot intensity mapping experiment." *SPIE Astronomical Telescopes + Instrumentation*, Montréal, Quebec, Canada.
- Croton, Darren J., Volker Springel, Simon D. M. White, G. De Lucia, C. S. Frenk, L. Gao, A. Jenkins, G. Kauffmann, J. F. Navarro, and N. Yoshida. 2006. "The many lives of active galactic nuclei: cooling flows, black holes and the luminosities and colours of galaxies." *Monthly Notices of the Royal Astronomical Society (MNRAS)* 365 (1):11-28. doi: 10.1111/j.1365-2966.2005.09675.x.
- Dale, Daniel A. , George Helou, Georgios E. Magdis, Lee Armus, Tanio Díaz-Santos, and Yong Shi. 2014. "A Two-parameter Model for the Infrared/Submillimeter/Radio Spectral Energy Distributions of Galaxies and Active Galactic Nuclei." *The Astrophysical Journal* 784 (1):83.
- Day, Peter K, Henry G LeDuc, Benjamin A Mazin, Anastasios Vayonakis, and Jonas Zmuidzinas. 2003. "A broadband superconducting detector suitable for use in large arrays." *Nature* 425 (6960):817.
- De Bernardis, P, PAR Ade, JJA Baselmans, ES Battistelli, A Benoit, M Bersanelli, A Bideaud, M Calvo, FJ Casas, and MG Castellano. 2018. "Exploring cosmic origins with CORE: The instrument." *Journal of Cosmology and Astroparticle Physics* 2018 (04):015.

- de Lange, Gerhard, Peter Roelfsema, Martin Giard, Francisco Najarro, Kees Wafelbakker, Willem Jellema, Brian Jackson, Marc Audard, Matt Griffin, and Franz Kerschbaum. 2018. "The SAFARI grating spectrometer for the SPICA space observatory (Conference Presentation)." Millimeter, Submillimeter, and Far-Infrared Detectors and Instrumentation for Astronomy IX.
- Dekel, Avishai, and Yuval Birnboim. 2006. "Galaxy bimodality due to cold flows and shock heating." *Monthly Notices of the Royal Astronomical Society* 368 (1):2-20.
- Devost, D., B. R. Brandl, and L. Armus. 2006. "[Ne III], [Ne II] and [S III] in NGC 253." In *The Spitzer Space Telescope: New Views of the Cosmos*, edited by L. Armus and W. T. Reach, 213.
- Di Matteo, Tiziana, Jörg Colberg, Volker Springel, Lars Hernquist, and Debora Sijacki. 2008. "Direct Cosmological Simulations of the Growth of Black Holes and Galaxies." *The Astrophysical Journal* 676 (1):33-53. doi: 10.1086/524921.
- Driver, Simon P, Stephen K Andrews, Elisabete da Cunha, Luke J Davies, Claudia Lagos, Aaron SG Robotham, Kevin Vinsen, Angus H Wright, Mehmet Alpaslan, and Joss Bland-Hawthorn. 2017. "GAMA/G10-COSMOS/3D-HST: the  $0 < z < 5$  cosmic star formation history, stellar-mass, and dust-mass densities." *Monthly Notices of the Royal Astronomical Society* 475 (3):2891-2935.
- Duan, Ran. 2015. "Instrumentation for Kinetic-Inductance-Detector-Based Submillimeter Radio Astronomy." California Institute of Technology.
- Duan, Ran, Sean McHugh, Bruno Serfass, Benjamin A Mazin, Andrew Merrill, Sunil R Golwala, Thomas P Downes, Nicole G Czakon, Peter K Day, and Jiansong Gao. 2010. "An open-source readout for MKIDs." Millimeter, Submillimeter, and Far-Infrared Detectors and Instrumentation for Astronomy V.
- Elftmann, Daniel. 2018. "Xilinx On-Orbit Reconfigurable Kintex UltraScale FPGA Technology for Space." SEFUW: Space FPGA Users Workshop, 4th Edition, European Space Research and Technology Centre (ESTEC), April 9-11, 2018.
- Farrah, Duncan, Kimberly Ennico Smith, David Ardila, Charles M Bradford, Michael Dipirro, Carl Ferkinhoff, Jason Glenn, Paul Goldsmith, David Leisawitz, and Thomas Nikola. 2017. "Far-Infrared Instrumentation and Technology Development for the Next Decade." *arXiv preprint arXiv:1709.02389*.
- Fernández-Ontiveros, JA, L Armus, Maarten Baes, J Bernard-Salas, AD Bolatto, J Braine, L Ciesla, Ilse De Looze, E Egami, and J Fischer. 2017. "SPICA and the Chemical Evolution of Galaxies: The Rise of Metals and Dust." *Publications of the Astronomical Society of Australia* 34.
- Fernández-Ontiveros, Juan Antonio, Luigi Spinoglio, Miguel Pereira-Santaella, Matthew A Malkan, Paola Andreani, and Kalliopi M Dasyra. 2016. "Far-infrared line spectra of active galaxies from the Herschel/PACS spectrometer: the complete database." *The Astrophysical Journal Supplement Series* 226 (2):19.
- Frayer, David T, DB Sanders, JA Surace, H Aussel, M Salvato, E Le Floch, MT Huynh, NZ Scoville, A Afonso-Luis, and B Bhattacharya. 2009. "Spitzer 70 and 160  $\mu\text{m}$  Observations of the COSMOS Field." *The Astronomical Journal* 138 (5):1261.
- Galliano, Frédéric, Eli Dwek, and Pierre Chaniai. 2008. "Stellar Evolutionary Effects on the Abundances of Polycyclic Aromatic Hydrocarbons and Supernova-Condensed Dust in Galaxies." *The Astrophysical Journal* 672 (1):214-243. doi: 10.1086/523621.
- Genzel, R, D Lutz, E Sturm, E Egami, D Kunze, AFM Moorwood, D Rigopoulou, HWW Spoon, A Sternberg, and LE Tacconi-Garman. 1998. "What powers ultraluminous IRAS galaxies?" *The Astrophysical Journal* 498 (2):579.
- Glaister, D. S., W. Gully, R. G. Ross, R. Stack, and E. Marquardt. 2005. "Ball Aerospace 4–10 K Space Cryocoolers." Cryocoolers 13, Boston, MA, 2005//.
- Glenn, J, A Conley, M Béthermin, B Altieri, A Amblard, V Arumugam, H Aussel, T Babbedge, A Blain, and J Bock. 2010. "HerMES: deep galaxy number counts from a P (D) fluctuation analysis of SPIRE Science Demonstration Phase observations." *Monthly Notices of the Royal Astronomical Society* 409 (1):109-121.

- Glenn, Jason, Charles M Bradford, Rashied Amini, Katey Alatalo, Lee Armus, Andrew Benson, Duncan Farrah, Adalyn Fyhrie, Sarah Lipsky, and Bradley Moore. 2018. "The Galaxy Evolution Probe: a concept for a mid and far-infrared space observatory." *Space Telescopes and Instrumentation 2018: Optical, Infrared, and Millimeter Wave*.
- Gong, Yan, Asantha Cooray, Marta B. Silva, Mario G. Santos, and Phillip Lubin. 2011. "Probing Reionization with Intensity Mapping of Molecular and Fine-structure Lines." *The Astrophysical Journal Letters* 728 (2):L46.
- Gordon, Samuel, Brad Dober, Adrian Sinclair, Samuel Rowe, Sean Bryan, Philip Maukopf, Jason Ausermann, Mark Devlin, Simon Dicker, and Jiansong Gao. 2016. "An open source, FPGA-based LeKID readout for BLAST-TNG: pre-flight results." *Journal of Astronomical Instrumentation* 5 (04):1641003.
- Griffin, Matthew Joseph, A Abergel, As Abreu, Peter AR Ade, P André, J-L Augueres, T Babbedge, Y Bae, T Baillie, and J-P Baluteau. 2010. "The Herschel-SPIRE instrument and its in-flight performance." *Astronomy & Astrophysics* 518:L3.
- Groves, Brent A, Michael A Dopita, and Ralph S Sutherland. 2004. "Dusty, Radiation Pressure-Dominated Photoionization. II. Multiwavelength Emission Line Diagnostics for Narrow-Line Regions." *The Astrophysical Journal Supplement Series* 153 (1):75.
- Hailey-Dunsheath, S, ACM Barlis, JE Aguirre, CM Bradford, JG Redford, TS Billings, HG LeDuc, CM McKenney, and MI Hollister. 2018. "Development of Aluminum LEKIDs for Balloon-Borne Far-IR Spectroscopy." *Journal of Low Temperature Physics*:1-8.
- Hailey-Dunsheath, S. et al. 2018. Sensitive mid- and far-IR kinetic inductance detector arrays for space astronomy, Proposal to NASA APRA program (selected).
- Henderson, Shawn W, Zeeshan Ahmed, Jason Ausermann, Daniel Becker, Douglas A Bennett, David Brown, Saptarshi Chaudhuri, Hsiao-Mei Sherry Cho, John M D'Ewart, and Bradley Dober. 2018. "Highly-multiplexed microwave squid readout using the slac microresonator radio frequency (smurf) electronics for future cmb and sub-millimeter surveys." *Millimeter, Submillimeter, and Far-Infrared Detectors and Instrumentation for Astronomy IX*.
- Herschel Team. 2014. 4.3 Source Confusion.
- Hezaveh, Yashar D, and Gilbert P Holder. 2011. "Effects of strong gravitational lensing on millimeter-wave galaxy number counts." *The Astrophysical Journal* 734 (1):52.
- Hickey, Gregory, Troy Barbee, Mark Ealey, and David Redding. 2010. "Actuated hybrid mirrors for space telescopes." *Space Telescopes and Instrumentation 2010: Optical, Infrared, and Millimeter Wave*.
- Hijmering, RA, R den Hartog, M Ridder, AJ van der Linden, J van der Kuur, JR Gao, and B Jackson. 2016. "Readout of a 176 pixel FDM system for SAFARI TES arrays." *Millimeter, Submillimeter, and Far-Infrared Detectors and Instrumentation for Astronomy VIII*.
- Holland, WS, D Bintley, EL Chapin, Antonio Chrysostomou, GR Davis, JT Dempsey, WD Duncan, M Fich, P Friberg, and M Halpern. 2013. "SCUBA-2: the 10 000 pixel bolometer camera on the James Clerk Maxwell Telescope." *Monthly Notices of the Royal Astronomical Society* 430 (4):2513-2533.
- Hsiao, Frank, Adrian Tang, Y. Kim, Brian Drouin, Goutam Chattopadhyay, and MC Frank Chang. 2015. "A 2.2 GS/s 188mW spectrometer processor in 65nm CMOS for supporting low-power THz planetary instruments." 2015 IEEE Custom Integrated Circuits Conference (CICC), San Jose, CA, Sep 28-30, 2015.
- Hurley, PD, S Oliver, M Betancourt, C Clarke, WI Cowley, S Duivenvoorden, D Farrah, M Griffin, C Lacey, and E Le Floch. 2016. "HELP: XID+, the probabilistic de-blender for Herschel SPIRE maps." *Monthly Notices of the Royal Astronomical Society* 464 (1):885-896.
- ISRA. 2018. "Infrared Science Archive (ISRA) External Data." [https://irsa.ipac.caltech.edu/data/Planck/release\\_1/external-data/external\\_maps.html](https://irsa.ipac.caltech.edu/data/Planck/release_1/external-data/external_maps.html).

- JPL/MDL, Jet Propulsion Laboratory/Microdevices Laboratory. 2018. "Deep-UV lithography capabilities at JPLs Microdevices Laboratory: Canon FPA3000 EX6." <https://microdevices.jpl.nasa.gov/infrastructure/equipment/>.
- Kennicutt Jr, Robert C. 1998. "The global Schmidt law in star-forming galaxies." *The Astrophysical Journal* 498 (2):541.
- Kewley, Lisa J., and Sara L. Ellison. 2008. "Metallicity calibrations and the mass-metallicity relation for star-forming galaxies." *The Astrophysical Journal* 681 (2):1183-1204. doi: 10.1086/587500.
- Labbé, Ivo, Pascal A Oesch, Garth D Illingworth, Pieter G Van Dokkum, Rychard J Bouwens, Marijn Franx, CM Carollo, Michele Trenti, B Holden, and Renske Smit. 2015. "Ultradeep IRAC Imaging Over the HUDF and GOODS-South: Survey Design and Imaging Data Release." *The Astrophysical Journal Supplement Series* 221 (2):23.
- Lagache, Guilaine. 2017. "Exploring the dusty star-formation in the early Universe using intensity mapping." *Proceedings of the International Astronomical Union* 12 (S333):228-233. doi: 10.1017/S1743921318000558.
- Le Mauff, J. 2018. "From eFPGA cores to RHBD System-On-Chip FPGA." SEFUW: Space FPGA Users Workshop (SEFUW), 4th Edition, held at ESA/ESTEC, Noordwijk, NL, 9-11 April 2018.
- Lee, C., G. Chattopadhyay, I. Medhi, J. J. Gill, C. D. Jung-Kubiak, and N. Llombart. 2013. Silicon Micromachined Microlens Array for THz Antennas. NASA Tech Briefs, 20130014109:9–10.
- Lee, D. S., G. R. Allen, G. Swift, M. Cannon, M. Wirthlin, J. S. George, R. Koga, and K. Huey. 2015. "Single-Event Characterization of the 20 nm Xilinx Kintex UltraScale Field-Programmable Gate Array under Heavy Ion Irradiation." 2015 IEEE Radiation Effects Data Workshop (REDW), 13-17 July 2015.
- Lee, David S. 2017. "Commercial Field-Programmable Gate Arrays for Space Processing Applications." Spaceborne Computing Conference, Albuquerque, NM, May 30 - June 2, 2017.
- Lidz, Adam, and Jessie Taylor. 2016. "On Removing Interloper Contamination from Intensity Mapping Power Spectrum Measurements." *The Astrophysical Journal* 825 (2):143.
- Liu, X., Weijie Guo, Y. Wang, M. Dai, L. F. Wei, B. Dober, C. M. McKenney, G. C. Hilton, Johannes Hubmayr, J. E. Austermann, J. N. Ullom, Jiachen Gao, and Michael Vissers. 2017. "Superconducting micro-resonator arrays with ideal frequency spacing." *Applied Physics Letters* 111:252601. doi: 10.1063/1.5016190.
- Logut, D., J. Breyse, Y. Toulemont, and M. Bougoin. 2005. "Light weight monolithic silicon carbide telescope for space application." *Optical Systems Design 2005*, October 14, 2015.
- Looney, L. et al. 2018. FIFI+LS: The FIFI-LS upgrade maximizing science, Proposal to NASA SOFIA Next Generation Instrumentation study (under review).
- Lourie, Nathan P., Peter A. R. Ade, Francisco E. Angile, Peter C. Ashton, Jason E. Austermann, Mark J. Devlin, Bradley Dober, Nicholas Galitzki, Jiansong Gao, Sam Gordon, Christopher E. Groppi, Jeffrey Klein, Gene C. Hilton, Johannes Hubmayr, Dale Li, Ian Lowe, Hamdi Mani, Philip Mauskopf, Christopher M. McKenney, Federico Nati, Giles Novak, Enzo Pascale, Giampaolo Pisano, Adrian Sinclair, Juan D. Soler, Carole Tucker, Joel N. Ullom, Michael Vissers, and Paul A. Williams. 2018. "Preflight characterization of the BLAST-TNG receiver and detector arrays." *SPIE Astronomical Telescopes + Instrumentation*, Austin, TX.
- Lutz, D., D. Kunze, H. W. W. Spoon, and M. D. Thornley. 1998. "Faint [O IV] emission from starburst galaxies." *arXiv preprint astro-ph/9803314* 333:L75-L78.
- Lutz, D., E. Sturm, R. Genzel, H. W. W. Spoon, A. F. M. Moorwood, H. Netzer, and A. Sternberg. 2003. "ISO spectroscopy of star formation and active nuclei in the luminous infrared galaxy NGC 6240." *Astronomy & Astrophysics* 409 (3):867-878. doi: 10.1051/0004-6361:20031165.
- Madau, Piero, and Mark Dickinson. 2014. "Cosmic Star-Formation History." *Annual Review of Astronomy and Astrophysics* 52 (1):415-486. doi: 10.1146/annurev-astro-081811-125615.
- Madau, Piero, Avery Meiksin, and Martin J. Rees. 1997. "21 Centimeter Tomography of the Intergalactic Medium at High Redshift." *The Astrophysical Journal* 475:429-444.

- Magnelli, B., Paola Popesso, Stefano Berta, F. Pozzi, D. Elbaz, Dominic Lutz, M. Dickinson, Bruno Altieri, P. Andreani, Herve Aussel, M. Bethermin, A. Bongiovanni, Jordi Cepa, Vassilis Charmandaris, R. R. Chary, A. Cimatti, E. Daddi, N. M. Förster Schreiber, R. Genzel, and Ivan Valtchanov. 2013. "The deepest Herschel -PACS far-infrared survey: Number counts and infrared luminosity functions from combined PEP/GOODS-H observations." *Astronomy & Astrophysics* 553. doi: 10.1051/0004-6361/201321371.
- Magorrian, John, Scott Tremaine, Douglas Richstone, Ralf Bender, Gary Bower, Alan Dressler, SM Faber, Karl Gebhardt, Richard Green, and Carl Grillmair. 1998. "The demography of massive dark objects in galaxy centers." *The Astronomical Journal* 115 (6):2285.
- Marconi, Alessandro, and Leslie K Hunt. 2003. "The relation between black hole mass, bulge mass, and near-infrared luminosity." *The Astrophysical Journal Letters* 589 (1):L21.
- Martin, Crystal L., and Robert C. Kennicutt, Jr. 2001. "Star Formation Thresholds in Galactic Disks." *The Astrophysical Journal* 555 (1):301-321. doi: 10.1086/321452.
- Mauskopf, P. D. 2018. "Transition Edge Sensors and Kinetic Inductance Detectors in Astronomical Instruments." *Publications of the Astronomical Society of the Pacific* 130 (990:082001). doi: 10.1088/1538-3873/aabaf0.
- Mazin, Benjamin A., Peter K. Day, Kent D. Irwin, Carl D. Reintsema, and Jonas Zmuidzinas. 2006. "Digital readouts for large microwave low-temperature detector arrays." *Nuclear Instruments and Methods in Physics Research Section A: Accelerators, Spectrometers, Detectors and Associated Equipment* 559 (2):799-801. doi: <https://doi.org/10.1016/j.nima.2005.12.208>.
- McConnell, Nicholas J, and Chung-Pei Ma. 2013. "Revisiting the scaling relations of black hole masses and host galaxy properties." *The Astrophysical Journal* 764 (2):184.
- McHugh, Sean, Benjamin A. Mazin, Bruno Serfass, Seth Meeker, Kieran O'Brien, Ran Duan, Rick Raffanti, and Dan Werthimer. 2012. "A readout for large arrays of microwave kinetic inductance detectors." *Review of Scientific Instruments* 83 (4):044702. doi: 10.1063/1.3700812.
- McKenney, Christopher M., Henry G. Leduc, Loren J. Swenson, Peter K. Day, Byeong H. Eom, and Jonas Zmuidzinas. 2012. "Design considerations for a background limited 350 micron pixel array using lumped element superconducting microresonators." SPIE Astronomical Telescopes + Instrumentation, Amsterdam, Netherlands, 24 September 2012.
- Merson, Alexander, Yun Wang, Andrew Benson, Andreas Faisst, Daniel Masters, Alina Kiessling, and Jason Rhodes. 2018. "Predicting H $\alpha$  emission-line galaxy counts for future galaxy redshift surveys." *Monthly Notices of the Royal Astronomical Society* 474 (1):177-196. doi: 10.1093/mnras/stx2649.
- MIPS. 2011. MIPS Instrument Handbook. In *MIPS Heritage Archive Documentation*, edited by MIPS Instrument and MIPS Instrument Support Teams.
- Mocanu, L. M., T. M. Crawford, J. D. Vieira, K. A. Aird, M. Aravena, J. E. Austermann, B. A. Benson, M. Béthermin, L. E. Bleem, M. Bothwell, J. E. Carlstrom, C. L. Chang, S. Chapman, H. M. Cho, A. T. Crites, T. de Haan, M. A. Dobbs, W. B. Everett, E. M. George, N. W. Halverson, N. Harrington, Y. Hezaveh, G. P. Holder, W. L. Holzapfel, S. Hoover, J. D. Hrubes, R. Keisler, L. Knox, A. T. Lee, E. M. Leitch, M. Lueker, D. Luong-Van, D. P. Marrone, J. J. McMahon, J. Mehl, S. S. Meyer, J. J. Mohr, T. E. Montroy, T. Natoli, S. Padin, T. Plagge, C. Pryke, A. Rest, C. L. Reichardt, J. E. Ruhl, J. T. Sayre, K. K. Schaffer, E. Shirokoff, H. G. Spieler, J. S. Spilker, B. Stalder, Z. Staniszewski, A. A. Stark, K. T. Story, E. R. Switzer, K. Vanderlinde, and R. Williamson. 2013. "Extragalactic Millimeter-wave Point-source Catalog, Number Counts and Statistics from 771 deg<sup>2</sup> of the SPT-SZ Survey." *The Astrophysical Journal* 779 (1):61.
- Monfardini, Alessandro, Jochem Baselmans, Alain Benoit, Aurelien Bideaud, Olivier Bourrion, Andrea Catalano, Martino Calvo, Antonio D'Addabbo, Simon Doyle, and Johannes Goupy. 2016. "Lumped element kinetic inductance detectors for space applications." Millimeter, Submillimeter, and Far-Infrared Detectors and Instrumentation for Astronomy VIII.

- Moore, Bradley, Jason Glenn, C. Matt Bradford, and Rashied Amini. 2018. "Thermal architecture of the galaxy evolution probe mission concept." SPIE Astronomical Telescopes + Instrumentation, Austin, TX.
- Müller, Thomas, Zoltán Balog, Markus Nielbock, Tanya Lim, David Teyssier, Michael Olberg, Ulrich Klaas, Hendrik Linz, Bruno Altieri, Chris Pearson, George Bendo, and Esa Vilenius. 2014. "Herschel celestial calibration sources." *Experimental Astronomy* 37 (2):253-330. doi: 10.1007/s10686-013-9357-y.
- Nagao, T., R. Maiolino, and H. Matsuhara. 2009. "Next Generation Study of the Cosmic Metallicity Evolution with SPICA." SPICA joint European/Japanese Workshop.
- Negrello, Mattia, S Amber, A Amvrosiadis, Z-Y Cai, A Lapi, J Gonzalez-Nuevo, G De Zotti, C Furlanetto, SJ Maddox, and M Allen. 2017. "The Herschel-ATLAS: a sample of 500  $\mu\text{m}$ -selected lensed galaxies over 600 deg<sup>2</sup>." *Monthly Notices of the Royal Astronomical Society* 465 (3):3558-3580.
- Nikola, Thomas, Edwin Bergin, Gordon L. Bjoraker, James G. Douthit, George E. Gull, Charles Henderson, Wen-Ting Hsieh, Alexander S. Kuttyrev, Gary Melnick, Stefanie N. Milam, Samuel H. Moseley, David A. Neufeld, Klaus Pontoppidan, Stephen A. Rinehart, Aki Roberge, Gordon J. Stacey, Johannes G. Staguhn, Dan M. Watson, and Edward J. Wollack. 2018. "HIRMES: the third generation instrument for SOFIA (Conference Presentation)." SPIE Astronomical Telescopes + Instrumentation, Austin, TX.
- Noroozian, Omid, Peter K. Day, Byeong Ho Eom, Henry G. Leduc, and Jonas Zmuidzinas. 2012. "Crosstalk Reduction for Superconducting Microwave Resonator Arrays." *IEEE Transactions on Microwave Theory and Techniques* 60 (5):1235-1243. doi: 10.1109/TMTT.2012.2187538.
- Ostriker, Eve C, Christopher F McKee, and Adam K Leroy. 2010. "Regulation of star formation rates in multiphase galactic disks: a thermal/dynamical equilibrium model." *The Astrophysical Journal* 721 (2):975.
- Paiella, A., A. Coppolecchia, L. Lamagna, P. A. R. Ade, E. S. Battistelli, M. G. Castellano, I. Colantoni, F. Columbro, G. D'Alessandro, P. de Bernardis, S. Gordon, S. Masi, P. Mauskopf, G. Pettinari, F. Piacentini, G. Pisano, G. Presta, and C. Tucker. 2018. Kinetic Inductance Detectors for the OLIMPO experiment: design and pre-flight characterization. *arXiv e-prints*. Accessed October 01, 2018.
- Peeters, E., A. G. G. M. Tielens, C. van Kerckhoven, S. Hony, L. J. Allamandola, D. M. Hudgins, and C. W. Bauschlicher. 2002. "ISO Spectroscopy of PAH Features." Hot Star Workshop III: The Earliest Stages of Massive Star Birth. ASP Conference Proceedings., San Francisco, CA, 10/2002.
- Planck Team. 2013. Planck Explanatory Supplement First Release v1.04.
- Poglitsch, A., C. Waelkens, N. Geis, H. Feuchtgruber, B. Vandenbussche, L. Rodriguez, O. Krause, E. Renotte, C. van Hoof, P. Saraceno, J. Cepa, F. Kerschbaum, P. Agnès, B. Ali, B. Altieri, P. Andreani, J. L. Augeres, Z. Balog, L. Barl, O. H. Bauer, N. Belbachir, M. Benedettini, N. Billot, O. Boulade, H. Bischof, J. Blommaert, E. Callut, C. Cara, R. Cerulli, D. Cesarsky, A. Contursi, Y. Creten, W. De Meester, V. Doublier, E. Doumayrou, L. Duband, K. Exter, R. Genzel, J. M. Gillis, U. Grözinger, T. Henning, J. Herreros, R. Huygen, M. Inguscio, G. Jakob, C. Jamar, C. Jean, J. de Jong, R. Katterloher, C. Kiss, U. Klaas, D. Lemke, D. Lutz, S. Madden, B. Marquet, J. Martignac, A. Mazy, P. Merken, F. Montfort, L. Morbidelli, T. Müller, M. Nielbock, K. Okumura, R. Orfei, R. Ottensamer, S. Pezzuto, P. Popesso, J. Putzeys, S. Regibo, V. Reveret, P. Royer, M. Sauvage, J. Schreiber, J. Stegmaier, D. Schmitt, J. Schubert, E. Sturm, M. Thiel, G. Tofani, R. Vavrek, M. Wetzstein, E. Wieprecht, and E. Wiezorrek. 2010. "The Photodetector Array Camera and Spectrometer (PACS) on the Herschel Space Observatory\*." *Astronomy & Astrophysics* 518 (Herschel: the first science highlights):12. doi: <https://doi.org/10.1051/0004-6361/201014535>.
- Pottasch, SR, DA Beintema, J Bernard Salas, and WA Feibelman. 2001. "Abundances of planetary nebulae NGC 7662 and NGC 6741." *Astronomy & Astrophysics* 380 (2):684-694.

- Raab, J., D. Durand, T. V. Nguyen, and E. Tward. 2013. "Active Cooling of 4K Telescopes and sub 4K Instruments." Space Cryogenics Workshop, 2013, The 25th Space Cryogenics Workshop, Alyeska Resort, Girdwood, Alaska, June 23-25, 2013.
- Riechers, Dominik A, Alexandra Pope, Emanuele Daddi, Lee Armus, Christopher L Carilli, Fabian Walter, Jacqueline Hodge, Ranga-Ram Chary, Glenn E Morrison, and Mark Dickinson. 2014. "Polycyclic Aromatic Hydrocarbon and Mid-Infrared Continuum Emission in a  $z > 4$  Submillimeter Galaxy." *The Astrophysical Journal* 786 (1):31.
- ROACH-1, (Reconfigurable Open Architecture Computing Hardware). 2008. "Standalone FPGA processing board." Collaboration for Astronomy Signal Processing and Electronics Research (CASPER). <https://casper.ssl.berkeley.edu/wiki/ROACH>.
- Santini, P., R. Maiolino, B. Magnelli, L. Silva, A. Grazian, B. Altieri, P. Andreani, H. Aussel, S. Berta, A. Bongiovanni, D. Brisbin, F. Calura, A. Cava, J. Cepa, A. Cimatti, E. Daddi, H. Dannerbauer, H. Dominguez-Sanchez, D. Elbaz, A. Fontana, N. Förster Schreiber, R. Genzel, G. L. Granato, C. Gruppioni, D. Lutz, G. Magdis, M. Magliocchetti, F. Matteucci, R. Nordon, I. Pérez Garcia, A. Poglitsch, P. Popesso, F. Pozzi, L. Riguccini, G. Rodighiero, A. Saintonge, M. Sanchez-Portal, L. Shao, E. Sturm, L. Tacconi, and I. Valtchanov. 2010. "The dust content of high- $z$  submillimeter galaxies revealed by Herschel \*\*\*." *Astronomy & Astrophysics* 518 (July-August 2010, Herschel: the first science highlights):6. doi: 10.1051/0004-6361/201014748.
- Schruba, Andreas, Adam K. Leroy, Fabian Walter, Frank Bigiel, Elias Brinks, W. J. G. de Blok, Gaelle Dumas, Carsten Kramer, Erik Rosolowsky, Karin Sandstrom, Karl Schuster, Antonio Usero, Axel Weiss, and Helmut Wiesemeyer. 2011. "A Molecular Star Formation Law in the Atomic-gas-dominated Regime in Nearby Galaxies." *The Astronomical Journal* 142 (2):25. doi: 10.1088/0004-6256/142/2/37.
- SEE, Single Event Effects. 2018. 27th Annual Single Event Effects (SEE) Symposium coupled with the Military and Aerospace Programmable Logic Devices (MAPLD) Workshop, San Diego, CA, 21-24 May 2018.
- SEFUW, Space FPGA Users Workshop, 4th Edition. 2018. "SEFUW: Space FPGA Users Workshop, 4th Edition." accessed 9-11 April 2018. <https://indico.esa.int/event/232/>.
- Sein, Emmanuel, Yves Toulemon, Frederic Safa, Michel Duran, Pierre Deny, Daniel de Chambure, Thomas Passvogel, and Goeran L. Pilbratt. 2003. "A  $\Phi$  3.5m diameter Sic telescope for Herschel mission." *Astronomical Telescopes and Instrumentation*, Waikoloa, Hawaii.
- Serra, Paolo, Olivier Doré, and Guilaine Lagache. 2016. "Dissecting the High- $z$  Interstellar Medium through Intensity Mapping Cross-correlations." *The Astrophysical Journal* 833 (2):153.
- Shaver, P. A., R. A. Windhorst, Piero Madau, and A. G. de Bruyn. 1999. "Can the reionization epoch be detected as a global signature in the cosmic background?" *Astronomy and Astrophysics* 345:380-390.
- Shirron, P. J., E. R. Canavan, M. J. DiPirro, J. G. Tuttle, and C. J. Yeager. 2000. "A Multi-Stage Continuous-Duty Adiabatic Demagnetization Refrigerator." In *Advances in Cryogenic Engineering*, edited by Quan-Sheng Shu, 1629-1638. Boston, MA: Springer US.
- Shirron, Peter J., and Michael J. Di Pirro. 2005. Passive gas-gap heat switch for adiabatic demagnetization refrigerator. The United States Of America As Represented By The Administrator Of The National Aeronautics And Space Administration.
- Shu, S., M. Calvo, J. Goupy, S. Leclercq, A. Catalano, A. Bideaud, A. Monfardini, and E. F. C. Driessen. 2018. "Increased multiplexing of superconducting microresonator arrays by post-characterization adaptation of the on-chip capacitors." *Applied Physics Letters* 113 (8):082603. doi: 10.1063/1.5040968.
- Sijacki, Debora, Volker Springel, Tiziana Di Matteo, and Lars Hernquist. 2007. "A unified model for AGN feedback in cosmological simulations of structure formation." *Monthly Notices of the Royal Astronomical Society (MNRAS)* 380 (3):877-900. doi: 10.1111/j.1365-2966.2007.12153.x.

- Silk, Joseph. 2013. "Unleashing positive feedback: linking the rates of star formation, supermassive black hole accretion, and outflows in distant galaxies." *The Astrophysical Journal* 772 (2):112. doi: 10.1088/0004-637X/772/2/112.
- Silk, Joseph, and Martin J. Rees. 1998. "Quasars and galaxy formation." *Astronomy & Astrophysics* 331:L1-L4.
- Silva, Marta, Mario G. Santos, Asantha Cooray, and Yan Gong. 2015. "Prospects for Detecting C II Emission during the Epoch of Reionization." *The Astrophysical Journal* 806 (2):209.
- Smith, John David T, DA Dale, L Armus, BT Draine, DJ Hollenbach, H Roussel, G Helou, RC Kennicutt Jr, A Li, and GJ Bendo. 2004. "Mid-infrared IRS spectroscopy of NGC 7331: A first look at the Spitzer Infrared Nearby Galaxies Survey (SINGS) legacy." *The Astrophysical Journal Supplement Series* 154 (1):199-203. doi: 10.1086/423133.
- Spilker, JS, DP Marrone, JE Aguirre, M Aravena, MLN Ashby, M Béthermin, CM Bradford, MS Bothwell, M Brodwin, and JE Carlstrom. 2014. "The rest-frame submillimeter spectrum of high-redshift, dusty, star-forming galaxies." *The Astrophysical Journal* 785 (2):149.
- Springel, Volker, Simon D. M. White, Adrian Jenkins, Carlos S. Frenk, Naoki Yoshida, Liang Gao, Julio Navarro, Robert Thacker, Darren Croton, John Helly, John A. Peacock, Shaun Cole, Peter Thomas, Hugh Couchman, August Evrard, Jörg Colberg, and Frazer Pearce. 2005. "Simulations of the formation, evolution and clustering of galaxies and quasars." *Nature* 435:629-636. doi: 10.1038/nature03597.
- Stacey, Gordon J., Stephen Parshley, Thomas Nikola, German Cortes-Medellin, Justin Schoenwald, Ganesh Rajagopalan, Michael D. Niemack, Tim Jenness, Patricio Gallardo, Brian Koopman, Charles D. Dowell, Peter K. Day, Matthew I. Hollister, Attila Kovacs, Henry G. LeDuc, Christopher M. McKenney, Ryan M. Monroe, Hiroshige Yoshida, Jonas Zmuidzinas, Loren J. Swenson, Simon J. Radford, Hien Trong Nguyen, Anthony K. Mroczkowski, Jason Glenn, Jordan Wheeler, Philip Maloney, Spencer Brugger, Joseph D. Adams, Frank Bertoldi, Reinhold Schaaf, Mark Halpern, Douglas Scott, Galen Marsden, Jack Sayers, Scott Chapman, and Joaquin D. Vieira. 2014. "SWCam: the short wavelength camera for the CCAT Observatory." SPIE Astronomical Telescopes + Instrumentation, Montréal, Quebec, Canada.
- Steeves, John, David Redding, James K. Wallace, Charles Lawrence, Todd Gaier, Randall Bartman, Raef Mikhail, Jeff Cavaco, and John Vayda. 2018. "Active mirrors for future space telescopes." SPIE Astronomical Telescopes + Instrumentation, Austin, TX.
- Strader, Matthew James. 2016. "Digital readout for microwave kinetic inductance detectors and applications in high time resolution astronomy." Doctor of Philosophy in Physics, University of California, Santa Barbara.
- Suginohara, Maki, Tatsushi Suginohara, and David N. Spergel. 1999. "Detecting  $z > 10$  Objects through Carbon, Nitrogen, and Oxygen Emission Lines." *The Astrophysical Journal* 512 (2):547.
- Swenson, Loren J., Peter K. Day, Charles D. Dowell, Byeong H. Eom, Matthew I. Hollister, Robert Jarnot, Attila Kovács, Henry G. Leduc, Christopher M. McKenney, Ryan Monroe, Tony Mroczkowski, Hien T. Nguyen, and Jonas Zmuidzinas. 2012. "MAKO: a pathfinder instrument for on-sky demonstration of low-cost 350 micron imaging arrays." SPIE Astronomical Telescopes + Instrumentation, Amsterdam, Netherlands.
- Swift, G. 2017. "Invited talk I: The foundations of robustness in reconfigurability in a radiation environment: Understanding single-event effects test results on SRAM-based FPGAs." 2017 NASA/ESA Conference on Adaptive Hardware and Systems (AHS), Pasadena, CA, 24-27 July 2017.
- Teplitz, HI, V Desai, L Armus, R Chary, JA Marshall, JW Colbert, DT Frayer, A Pope, A Blain, and HWW Spoon. 2007. "Measuring PAH Emission in Ultradeep Spitzer\* IRS\*\* Spectroscopy of High-Redshift IR-Luminous Galaxies." *The Astrophysical Journal* 659 (2):941.
- Tielens, A. G. G. M. 2008. "Interstellar Polycyclic Aromatic Hydrocarbon Molecules." *Annual Review of Astronomy and Astrophysics* 46 (1):289-337. doi: 10.1146/annurev.astro.46.060407.145211.

- Toba, Yoshiki, Tohru Nagao, Masaru Kajisawa, Taira Oogi, Masayuki Akiyama, Hiroyuki Ikeda, Jean Coupon, Michael A Strauss, Wei-Hao Wang, and Masayuki Tanaka. 2017. "Clustering of infrared-bright dust-obscured galaxies revealed by the Hyper Suprime-Cam and WISE." *The Astrophysical Journal* 835 (1):36.
- Trimberger, S. M. 2015. "Three Ages of FPGAs: A Retrospective on the First Thirty Years of FPGA Technology." *Proceedings of the IEEE* 103 (3):318-331. doi: 10.1109/JPROC.2015.2392104.
- Tumlinson, Jason, Molly S Peeples, and Jessica K Werk. 2017. "The circumgalactic medium." *Annual Review of Astronomy and Astrophysics* 55:389-432.
- Uzgil, B. D., J. E. Aguirre, C. M. Bradford, and A. Lidz. 2014. "Measuring Galaxy Clustering and the Evolution of [C II] Mean Intensity with Far-IR Line Intensity Mapping during  $0.5 < z < 1.5$ ." *The Astrophysical Journal* 793 (2):116.
- van Rantwijk, J., M. Grim, D. van Loon, S. Yates, A. Baryshev, and J. Baselmans. 2016. "Multiplexed Readout for 1000-Pixel Arrays of Microwave Kinetic Inductance Detectors." *IEEE Transactions on Microwave Theory and Techniques* 64 (6):1876-1883. doi: 10.1109/TMTT.2016.2544303.
- Wagner, A. Y., G. V. Bicknell, M. Umemura, R. S. Sutherland, and J. Silk. 2016. "Galaxy-scale AGN feedback – theory." *Astronomische Nachrichten* 337 (1-2):167-174. doi: 10.1002/asna.201512287.
- Walch, S., P. Girichidis, T. Naab, A. Gatto, S. C. O. Glover, R. Wünsch, R. S. Klessen, P. C. Clark, T. Peters, D. Derigs, and C. Baczynski. 2015. "The SILCC (SIMulating the LifeCYcle of molecular Clouds) project – I. Chemical evolution of the supernova-driven ISM." *Monthly Notices of the Royal Astronomical Society* 454 (1):238-268. doi: 10.1093/mnras/stv1975.
- Wang, I., D. Keymeulen, D. Tran, E. Liggett, M. Klimesh, D. Dolman, D. Nunes, P. Sullivan, M. Bernas, and M. Pham. 2018. "LiveCheckHSI: A hardware/software co-verification tool for hyperspectral imaging systems with embedded system-on-chip instrument avionics." 2018 IEEE Aerospace Conference, Big Sky, MT, 3-10 March 2018.
- Wheeler, Jordan D., Steve Hailey-Dunsheath, Erik Shirokoff, Peter S. Barry, Charles M. Bradford, Scott Chapman, George Che, Simon Doyle, Jason Glenn, Sam Gordon, Matthew Hollister, Atilla Kovacs, Henry G. Leduc, Philip Maukopf, Ryan McGeehan, Christopher McKenney, Theodore Reck, Joeseeph Redford, Colin Ross, Corwin Shiu, Carole Tucker, Jordan Turner, and Jonas Zmuidzinas. 2018. "SuperSpec: the on-chip spectrometer: characterization of a full 300 channel filterbank (Conference Presentation)." SPIE Astronomical Telescopes + Instrumentation, Austin, TX, 10 July 2018.
- Wilson, Derek, Asantha Cooray, Hooshang Nayyeri, Matteo Bonato, Charles M Bradford, David L Clements, Gianfranco De Zotti, Tanio Díaz-Santos, Duncan Farrah, and Georgios Magdis. 2017. "Stacked Average Far-infrared Spectrum of Dusty Star-forming Galaxies from the Herschel/SPIRE Fourier Transform Spectrometer." *The Astrophysical Journal* 848 (1):30.
- Wilson, Grant W., Peter Ade, Itziar Aretxaga, Jason E. Austermann, Joseph Bardin, Peter Barry, James Beall, Marc Berthoud, Alan Braeley, Sean A. Bryan, Alexandra Burkott, John Bussan, Edgar Castillo, Miguel Chavez, Natalie DeNigris, Simon Doyle, Miranda Eiben, Daniel Ferrusca, Laura Fissel, Jiansong Gao, Walter Gear, Victor Gómez, Sam Gordon, Chris Groppi, Robert Gutermuth, Mark Heyer, Stephen Kuczarski, Mohsen Hosseini, Stella Offner, Alexandra Pope, F. Peter Schloerb, Kamal Souccar, Yuping Tang, Gary Wallace, Min S. Yun, Phillip Maukopf, Rhys Kelso, Jacob Knapp, Emily Lunde, Hamdi Mani, Justin Mathewson, Evan Scannapieco, Matt Underhill, Johannes Hubmayr, Michael Vissers, David H. Hughes, Ivan Rodriguez Montoya, David Sanchez, Miguel Velazquez, Salvador Ventura, Enzo Pascale, Sam Rowe, Carole Tucker, Giles Novak, Jeff McMahon, and Sara Simon. 2018. "The TolTEC project: a millimeter wavelength imaging polarimeter (Conference Presentation)." SPIE Astronomical Telescopes + Instrumentation, Austin, TX, 10 July 2018.
- Wirthlin, M. J. 2013. "FPGAs operating in a radiation environment: lessons learned from FPGAs in space." *Journal of Instrumentation* 8 (02):C02020.

- Wolfire, Mark G, Christopher F McKee, David Hollenbach, and AGGM Tielens. 2003. "Neutral atomic phases of the interstellar medium in the galaxy." *The Astrophysical Journal* 587 (1):278-311.
- Xilinx. 2015a. Vertex-5 Family Overview, DS100 (v5.1).
- Xilinx. 2015b. Virtex-6 Family Overview, DS150 (v2.5).
- Yates, S. J. C., A. M. Baryshev, J. J. A. Baselmans, B. Klein, and R. Güsten. 2009. "Fast Fourier transform spectrometer readout for large arrays of microwave kinetic inductance detectors." *Applied Physics Letters* 95 (4):042504. doi: 10.1063/1.3159818.
- Yates, Stephen J. C., Andrey M. Baryshev, Ozan Yurduseven, Juan Bueno, Kristina K. Davis, Lorenza Ferrari, Willem Jellema, Nuria Llombart, Vignesh Murugesan, David J. Thoen, and Jochem J. A. Baselmans. 2017. "Surface Wave Control for Large Arrays of Microwave Kinetic Inductance Detectors." *IEEE Transactions on Terahertz Science and Technology* 7 (6):789-799. doi: 10.1109/TTHZ.2017.2755500.
- Zmuidzinas, Jonas. 2012. "Superconducting Microresonators: Physics and Applications." *Annual Review* 3 (Condensed Matter Physics):169-214.

**COST TABLE**

**2020 Astrophysical Decadal Survey - Probe Mission Preparatory Study  
Master Equipment List Based Parametric Total Lifecycle Cost Estimate**

**Mission Name / Acronym:** Galaxy Evolution Probe/GEP  
**Cost Estimator:** JPL Team X  
**Date of Cost Estimate:** December 10, 2018  
**Cost Estimate Based On:** Final Master Equipment List

<b><u>PROJECT PHASE</u></b>		<b><u>COST [FY18 \$M]</u></b>
<b>Phase A</b>		(See Note 1)
<b>Phases B-D</b>	Mgmt, SE, MA	\$54
	Science	\$16
	Telescope	\$27
	Instrument 1 (Detectors)	\$64
	Instrument 2 (Payload Thermal)	\$71
	Instrument 3 (Wraps)	\$6
	Spacecraft, including ATLO	\$258
	MOS/GDS	\$44
	Launch Vehicle and Services	\$150
	Reserves	\$162
<b>Total Cost Phases A-D</b>		<b>\$852</b>
<b>Phase E-F</b>	Operations	\$87
	Reserves	\$12
	<b>Total Cost Phases E-F</b>	
<b>TOTAL LIFECYCLE COST</b>		<b>\$951</b>

**Notes:**

1. Team X estimates costs for Phase A-D. A break out of Phase A cost is not available. In this table, Phase A costs are included in Phase B-D.
2. This parametric cost estimate is based on the Probe's Master Equipment List derived from the Final Engineering Concept Definition Package that accurately reflects the mission described in the Probe's Final Report. This estimate is to be used only for non-binding rough order of magnitude planning purposes.
3. Team X estimates are generally model-based, and were generated after a series of instrument and mission level studies. Their accuracy is commensurate with the level of understanding typical to Pre-Phase-A concept development. They do not constitute an implementation or cost commitment on the part of JPL or Caltech.